Planck early results

Planck early results. XV. Spectral energy distributions and radio continuum spectra of northern extragalactic radio sources[★,★★]

Planck Collaboration: J. Aatrokoski[1], P. A. R. Ade[82], N. Aghanim[53], H. D. Aller[4], M. F. Aller[4], E. Angelakis[75], M. Arnaud[69], M. Ashdown[66,7], J. Aumont[53], C. Baccigalupi[80], A. Balbi[33], A. J. Banday[87,11,74], R. B. Barreiro[60], J. G. Bartlett[6,64], E. Battaner[89], K. Benabed[54], A. Benoît[52], A. Berdyugin[86], J.-P. Bernard[87,11], M. Bersanelli[30,47], R. Bhatia[8], A. Bonaldi[43], L. Bonavera[80,9], J. R. Bond[10], J. Borrill[73,83], F. R. Bouchet[54], M. Bucher[6], C. Burigana[46], D. N. Burrows[17], P. Cabella[33], M. Capalbi[2], M. Capellini[47], J.-F. Cardoso[70,6,54], A. Catalano[6,68], E. Cavazzuti[2], L. Cayón[21], A. Challinor[57,66,13], A. Chamballu[50], R.-R. Chary[51], L.-Y Chiang[56], P. R. Christensen[78,34], D. L. Clements[50], S. Colafrancesco[44], S. Colombi[54], F. Couchot[72], A. Coulais[68], S. Cutini[2], F. Cuttaia[46], L. Danese[80], R. D. Davies[65], R. J. Davis[65], P. de Bernardis[29], G. de Gasperis[33], A. de Rosa[46], G. de Zotti[43,80], J. Delabrouille[6], J.-M. Delouis[54], C. Dickinson[65], H. Dole[53], S. Donzelli[47,58], O. Doré[64,12], U. Dörl[74], M. Douspis[53], X. Dupac[37], G. Efstathiou[57], T. A. Enßlin[74], F. Finelli[46], O. Forni[87,11], M. Frailis[45], E. Franceschi[46], L. Fuhrmann[75], S. Galeotta[45], K. Ganga[6,51], F. Gargano[61], D. Gasparrini[2], N. Gehrels[5], M. Giard[87,11], G. Giardino[38], N. Giglietto[27,61], P. Giommi[3], F. Giordano[27], Y. Giraud-Héraud[6], J. González-Nuevo[80], K. M. Górski[64,92], S. Gratton[66,57], A. Gregorio[31], A. Gruppuso[46], D. Harrison[57,66], S. Henrot-Versillé[72], D. Herranz[60], S. R. Hildebrandt[12,71,59], E. Hivon[54], M. Hobson[7], W. A. Holmes[64], W. Hovest[74], R. J. Hoyland[59], K. M. Huffenberger[90], A. H. Jaffe[50], M. Juvela[20], E. Keihänen[20], R. Keskitalo[64,20], O. King[79], T. S. Kisner[73], L. Knox[23], T. P. Krichbaum[75], H. Kurki-Suonio[20,41], G. Lagache[53], A. Lähteenmäki[1,41], J.-M. Lamarre[68], A. Lasenby[7,66], R. J. Laureijs[38], N. Lavonen[1], C. R. Lawrence[64], S. Leach[80], R. Leonardi[37,38,24], J. León-Tavares[1], J. Linden-Vørnle[15], E. Lindfors[86], M. López-Caniego[60], P. M. Lubin[24], J. F. Macías-Pérez[71], B. Maffei[65], D. Maino[30,47], N. Mandolesi[46], R. Mann[81], M. Maris[45], E. Martínez-González[60], S. Masi[29], M. Massardi[43], S. Matarrese[26], F. Matthai[74], W. Max-Moerbeck[79], M. N. Mazziotta[61], P. Mazzotta[33], A. Melchiorri[29], L. Mendes[37], A. Mennella[30,45], P. F. Michelson[91], M. Mingaliev[84], S. Mitra[64], M.-A. Miville-Deschênes[53,10], A. Moneti[54], C. Monte[27,61], L. Montier[87,11], G. Morgante[46], D. Mortlock[50], D. Munshi[82,57], A. Murphy[77], P. Naselsky[78,34], P. Natoli[32,2,46], I. Nestoras[75], C. B. Netterfield[18], E. Nieppola[1,39], K. Nilsson[39], H. U. Nørgaard-Nielsen[15], F. Noviello[53], D. Novikov[50], I. Novikov[78], I. J. O'Dwyer[64], S. Osborne[85], F. Pajot[53], B. Partridge[40], F. Pasian[45], G. Patanchon[6], V. Pavlidou[79], T. J. Pearson[12,51], O. Perdereau[72], L. Perotto[71], M. Perri[2], F. Perrotta[80], F. Piacentini[29], M. Piat[6], S. Plaszczynski[72], P. Platania[63], E. Pointecouteau[87,11], G. Polenta[2,44], N. Ponthieu[53], T. Poutanen[41,20,1], G. Prézeau[12,64], P. Procopio[46], S. Prunet[54], J.-L. Puget[53], J. P. Rachen[74], S. Rainò[27,61], W. T. Reach[88], A. Readhead[79], R. Rebolo[59,35], R. Reeves[79], M. Reinecke[74], R. Reinthal[86], C. Renault[71], S. Ricciardi[46], J. Richards[79], T. Riller[74], D. Riquelme[55], I. Ristorcelli[87,11], G. Rocha[64,12], C. Rosset[6], M. Rowan-Robinson[50], J. A. Rubiño-Martín[59,35], B. Rusholme[51], J. Saarinen[86], M. Sandri[46], P. Savolainen[1], D. Scott[19], M. D. Seiffert[64,12], A. Sievers[55], A. Sillanpää[86], G. F. Smoot[22,73,6], Y. Sotnikova[84], J.-L. Starck[69,14], M. Stevenson[79], F. Stivoli[48], V. Stolyarov[7], R. Sudiwala[82], J.-F. Sygnet[54], L. Takalo[86], J. Tammi[1], J. A. Tauber[38], L. Terenzi[46], D. J. Thompson[5], L. Toffolatti[16], M. Tomasi[30,47], M. Tornikoski[1], J.-P. Torre[53], G. Tosti[62,28], A. Tramacere[49], M. Tristram[72], J. Tuovinen[76], M. Türler[49], M. Turunen[1], G. Umana[42], H. Ungerechts[55], L. Valenziano[46], E. Valtaoja[86], J. Varis[76], F. Verrecchia[2], P. Vielva[60], F. Villa[46], N. Vittorio[33], B. D. Wandelt[54,25], J. Wu[67], D. Yvon[14], A. Zacchei[45], J. A. Zensus[75], X. Zhou[67], and A. Zonca[24]

(Affiliations can be found after the references)

ABSTRACT

Spectral energy distributions (SEDs) and radio continuum spectra are presented for a northern sample of 104 extragalactic radio sources, based on the *Planck* Early Release Compact Source Catalogue (ERCSC) and simultaneous multifrequency data. The nine *Planck* frequencies, from 30 to 857 GHz, are complemented by a set of simultaneous observations ranging from radio to gamma-rays. This is the first extensive frequency coverage in the radio and millimetre domains for an essentially complete sample of extragalactic radio sources, and it shows how the individual shocks, each in their own phase of development, shape the radio spectra as they move in the relativistic jet. The SEDs presented in this paper were fitted with second and third degree polynomials to estimate the frequencies of the synchrotron and inverse Compton (IC) peaks, and the spectral indices of low and high frequency radio data, including the *Planck* ERCSC data, were calculated. SED modelling methods are discussed, with an emphasis on proper, physical modelling of the synchrotron bump using multiple components. *Planck* ERCSC data also suggest that the original accelerated electron energy spectrum could be much harder than commonly thought, with power-law index around 1.5 instead of the canonical 2.5. The implications of this are discussed for the acceleration mechanisms effective in blazar shocks. Furthermore in many cases the *Planck* data indicate that gamma-ray emission must originate in the same shocks that produce the radio emission.

Key words. galaxies: active – BL Lacertae objects: general – quasars: general – radiation mechanisms: non-thermal

---

★ Corresponding author: A. Lähteenmäki,
e-mail: `alien@kurp.hut.fi`
★★ Tables 1 and 4, Figs. 18–121 are available in electronic form at
`http://www.aanda.org`

1. Introduction

This paper is part of the first series of publications based on measurements made with the *Planck*[1] satellite. *Planck* (Tauber et al. 2010; Planck Collaboration 2011a) is the third-generation space mission to measure the anisotropy of the cosmic microwave background (CMB). It observes the sky in nine frequency bands covering 30−857 GHz with high sensitivity and angular resolution from 31′ to 5′. The Low Frequency Instrument (LFI; Mandolesi et al. 2010; Bersanelli et al. 2010; Mennella et al. 2011) covers the 30, 44, and 70 GHz bands with amplifiers cooled to 20 K. The High Frequency Instrument (HFI; Lamarre et al. 2010; Planck HFI Core Team 2011a) covers the 100, 143, 217, 353, 545, and 857 GHz bands with bolometers cooled to 0.1 K. Polarization is measured in all but the highest two bands (Leahy et al. 2010; Rosset et al. 2010). A combination of radiative cooling and three mechanical coolers produces the temperatures needed for the detectors and optics (Planck Collaboration 2011b). Two data processing centres (DPCs) check and calibrate the data and make maps of the sky (Planck HFI Core Team 2011b; Zacchei et al. 2011). *Planck*'s sensitivity, angular resolution, and frequency coverage make it a powerful instrument for Galactic and extragalactic astrophysics as well as cosmology.

The paper uses data from the *Planck* Early Release Compact Source Catalogue (ERCSC; Planck Collaboration 2011c). The ERCSC provides positions and flux densities of compact sources found in each of the nine *Planck* frequency maps. The flux densities are calculated using aperture photometry, with careful modelling of *Planck*'s elliptical beams. The ERCSC includes data from the first all-sky survey, taken between 13 August 2009 and 6 June 2010. This unique dataset offers the first glimpse of the previously unmapped millimetre and sub-millimetre sky. It is used here to create spectral energy distributions (SEDs) of 104 radio-bright, northern active galactic nuclei (AGN), with the most complete coverage in the radio to sub-millimetre frequencies to date.

Radio-loud AGN host jets of relativistic matter emanating symmetrically from the core. These jets produce copious amounts of non-thermal radiation, which dominates the SEDs of such sources compared with any thermal emission from the nucleus, i.e., the accretion disk. The SEDs typically consist of two broad-band bumps, the one at lower frequencies attributed to synchrotron radiation, and the other at higher frequencies attributed to inverse Compton (IC) radiation. The peak frequencies of the two bumps vary from one object to another. The peak of the synchrotron component can be between the infrared and X-ray domains, and the IC peak can range from MeV to GeV energies. The sequence in the peak frequencies of the emitted energy, and the factors that create it, have been a hot topic in blazar research for more than a decade (e.g., Fossati et al. 1997; Ghisellini et al. 1998; Padovani 2007; Ghisellini & Tavecchio 2008; Nieppola et al. 2008; Ghisellini & Tavecchio 2008; Sambruna et al. 2010).

Research on blazar SEDs has concentrated on two approaches. The first is fitting the SED with a simple function, usually a second or third order polynomial, to obtain the pivotal peak frequencies and luminosities of the radiation components in

a straightforward manner. This approach is typically used when studying large samples (Fossati et al. 1998; Nieppola et al. 2006; Sambruna et al. 2006; Nieppola et al. 2008; Abdo et al. 2010a). The second approach is detailed modelling of the SED, starting with the definition of initial parameters such as electron energy, magnetic field intensity, and Doppler factor. This method is more time-consuming and is used mostly for individual sources (e.g., Acciari et al. 2010; Collmar et al. 2010). The standard model is a leptonic, homogeneous, one-zone model, where the emission originates in a single component (for a review of the blazar emission models, see Böttcher 2010). One-zone models are useful as first-order approximations, but, in reality, AGN jets are rarely, if ever, dominated by a single source of radiation. The material in the jets flows through shocks in the jet, which locally enhance the radiation (the "shock-in-jet" model; Marscher & Gear 1985; Valtaoja et al. 1992). There can be several of these shocks in the jet simultaneously, and adding these to the emission of the quiescent jet, we have several radiation components. Therefore, ideally, the SEDs and radio spectra should be modelled with more than one component. Such modelling is also necessary for the proper identification of the high frequency (IC) emission sites.

In this paper we use the nearly complete SEDs and well-covered radio spectra provided by *Planck* to look for signs of these multiple components contributing to the total radiation that we observe. The paper is structured as follows. In Sects. 2 and 3 we introduce our sample and summarize the multifrequency data used in our study. The SEDs and radio spectra are discussed in Sects. 4 and 5, and their modelling is described in Sect. 6. In Sect. 7 we discuss the implications of our results for understanding the acceleration mechanisms in blazar jets, and in Sect. 8 we summarize our conclusions. Throughout the paper we adopt the sign convention for spectral index, α: $S_\nu \propto \nu^\alpha$. The errors of numerical values marked with a plus-minus sign correspond to one standard deviation.

2. The sample

The complete sample presented in this paper consists of 104 northern and equatorial radio-loud AGN. It includes all AGN with declination $\geq -10°$ that have a measured average radio flux density at 37 GHz exceeding 1 Jy. Most of the sample sources have been monitored at Metsähovi Radio Observatory for many years, and the brightest sources have been observed for up to 30 years. The sample can be divided into subclasses as follows: 33 high-polarization quasars (HPQs), 21 low-polarization quasars (LPQs), 21 BL Lacertae objects (BLOs), 19 normal quasars (QSOs), 9 radio galaxies (GALs), and one unclassified source (J184915+67064). (See, for example, Hovatta et al. 2008, 2009, for additional information on the classification.) By high-polarized quasars we mean objects which have a measured optical polarization $\geq 3\%$ at some epoch, while low-polarized quasars have a polarization $\leq 3\%$. Normal quasars have no polarization measured, so they could be either HPQs or LPQs. Radio galaxies are non-quasar AGN. The full sample is listed in Table 1. Columns 1 and 2 give the name and J2000 name for the source, and for some sources an alternative name is given in Col. 3. The coordinates of the sources are given in Cols. 4 and 5. The start dates of the *Planck* scans are listed in Cols. 6 and 7. The average 37 GHz flux density from Metsähovi observations is given in Col. 8. For Col. 9 onwards, see Sect. 4.

3. Multifrequency data

The core of our data set is the *Planck* ERCSC. The construction and contents of the catalogue are described in Planck

Table 2. Optical and radio observatories that participated in the *Planck* multifrequency campaigns.

Radio observatory	frequencies [GHz]
APEX, Chile	345
ATCA, Australia	4.5–40
Effelsberg, Germany	2.64–43
IRAM Pico Veleta, Spain	86, 142
Medicina, Italy	5, 8.3
Metsähovi, Finland	37
OVRO, USA	15
RATAN-600, Russia	1.1, 2.3, 4.8, 7.7, 11.2, 21.7
UMRAO	4.8, 8.0, 14.5
VLA, USA	5, 8, 22, 43
Optical observatory	band
KVA, Spain	*R*
Xinglong, China	*i*

Table 3. Parameters for the RATAN-600 receivers.

f_c [GHz]	Δf [GHz]	ΔT [mK]	T_{phys} [K]	T_{sys} [K]
21.7	2.5	3.5	15	77
11.2	1.4	3	15	65
7.7	1.0	3	15	62
4.8	0.9	2.2	15	39
2.3	0.4	8	310	95
1.1	0.12	15	310	105

Collaboration (2011c). For most sources, the ERCSC flux density values are averages of two scans, separated by about six months. To enable extensive multifrequency studies with a simultaneous data set, the *Planck* Extragalactic Working Group has coordinated a programme in which ground-based and space-borne telescopes observe the sources in unison with *Planck*. In this paper we present SEDs based on the averaged ERCSC flux densities and on multifrequency supporting observations taken within two weeks of the *Planck* scans. In a later paper we will present single-epoch SEDs, constructed from all the available *Planck* and supplementary simultaneous multifrequency data. This collaborative programme includes 12 observatories around the world (Table 2). Archival data have been obtained from the literature and from the search tool at the ASI (Agenzia Spaziale Italiana) Science Data Center (ASDC) web page[2].

3.1. Radio and submillimetre data

Centimetre-band observations were obtained with the University of Michigan Radio Astronomy Observatory's (UMRAO) 26-m prime focus paraboloid equipped with radiometers operating at central frequencies of 4.8, 8.0, and 14.5 GHz. Observations at all three frequencies employed rotating polarimeter systems permitting both total flux density and linear polarization to be measured. A typical measurement consisted of 8−16 individual measurements over a 20−40 min period. Frequent drift scans were made across stronger sources to verify the telescope pointing correction curves, and observations of programme sources were intermixed with observations of a grid of calibrator sources to correct for temporal changes in the antenna aperture efficiency. The flux scale was based on observations of Cassiopeia A (Baars et al. 1977). Details of the calibration and analysis techniques are described in Aller et al. (1985).

Six-frequency broadband radio spectra were obtained with the RATAN-600 radio telescope in transit mode by observing simultaneously at 1.1, 2.3, 4.8, 7.7, 11.2, and 21.7 GHz (Parijskij 1993; Berlin & Friedman 1996). The parameters of the receivers are listed in Table 3, where ν_c is the central frequency, $\Delta\nu$ is the bandwidth, ΔT is the sensitivity of the radiometer over a 1 s integration, T_{phys} is the physical temperature of the front-end amplifier, and T_{sys} is the noise temperature of the whole system at the given frequency. Data were reduced using the

RATAN standard software *FADPS* (Flexible Astronomical Data Processing System) reduction package (Verkhodanov 1997). The flux density measurement procedure at RATAN-600 is described by Aliakberov et al. (1985).

The 37 GHz observations were made with the 13.7-m Metsähovi radio telescope using a 1 GHz bandwidth, dual-beam receiver centred at 36.8 GHz. The observations were ON–ON observations, alternating the source and the sky in each feed horn. The integration time used to obtain each flux density data point typically ranged from 1200 to 1400 s. The detection limit of the telescope at 37 GHz is ∼0.2 Jy under optimal conditions. Data points with a signal-to-noise ratio less than four were handled as non-detections. The flux density scale was set by observations of DR 21. Sources NGC 7027, 3C 274, and 3C 84 were used as secondary calibrators. A detailed description of the data reduction and analysis is given in Teräsranta et al. (1998). The error estimate in the flux density includes the contribution from the measurement rms and the uncertainty of the absolute calibration.

Quasi-simultaneous centimetre/millimetre radio spectra for a large number of *Planck* blazars have been obtained within the framework of a *Fermi*-GST related monitoring programme of gamma-ray blazars (the F-GAMMA programme, Fuhrmann et al. 2007; Angelakis et al. 2008). The frequency range spans 2.64 GHz to 142 GHz using the Effelsberg 100-m and IRAM 30-m telescopes. The Effelsberg measurements were conducted with the secondary focus heterodyne receivers at 2.64, 4.85, 8.35, 10.45, 14.60, 23.05, 32.00, and 43.00 GHz. The observations were performed quasi-simultaneously with cross-scans, i.e., slewing over the source position in the azimuth and elevation directions, with an adaptive number of sub-scans for reaching the desired sensitivity (for details, see Fuhrmann et al. 2008; Angelakis et al. 2008). Pointing offset correction, gain correction, atmospheric opacity correction, and sensitivity correction have been applied to the data.

The Institut de Radioastronomie Millimétrique (IRAM) observations were carried out with calibrated cross-scans using the EMIR horizontal and vertical polarisation receivers operating at 86.2 and 142.3 GHz. The opacity-corrected intensities were converted to the standard temperature scale and corrected for small remaining pointing offsets and systematic gain-elevation effects. The conversion to the standard flux-density scale was done using the instantaneous conversion factors derived from frequently observed primary calibrators (Mars, Uranus) and secondary calibrators (W3(OH), K3-50A, NGC 7027). From this programme, radio spectra measured quasi-simultaneously with the *Planck* observations have been collected for a total of 37 *Planck* blazars during the period August 2009 to June 2010.

Many of the sources in the sample were monitored at 15 GHz using the 40-m telescope of the Owens Valley Radio Observatory (OVRO) as part of a larger monitoring programme (Richards et al. 2011). The flux density of each source was measured approximately twice weekly, with occasional gaps

---

[2] http://www.asdc.asi.it

due to poor weather or instrumental problems. The telescope is equipped with a cooled receiver installed at prime focus, with two symmetric off-axis corrugated horn feeds sensitive to left circular polarization. The telescope and receiver combination produces a pair of approximately Gaussian beams (157″ FWHM), separated in azimuth by 12′.95. The receiver has a centre frequency of 15.0 GHz, a 3.0 GHz bandwidth, and a noise-equivalent reception bandwidth of 2.5 GHz. Measurements were made using a Dicke-switched dual-beam system, with a second level of switching in azimuth to alternate source and sky in each of the two horns. Calibration was referred to 3C 286, for which a flux density of 3.44 Jy at 15 GHz is assumed (Baars et al. 1977). Details of the observations, calibration, and analysis are given by Richards et al. (2011).

The Very Large Array (VLA) and (since spring 2010) the Expanded VLA also observed a subset of the sources as simultaneously as possible. Most of the VLA and EVLA runs were brief 1–2 h blocks of time. In a one-hour block of time, in addition to flux calibrators and phase calibrators, typically 5–8 *Planck* sources were observed. In many cases, VLA flux density and phase calibrators were themselves of interest, since they were bright enough to be detected by *Planck*. For these bright sources, the integration times could be extremely short. At 4.86 GHz and 8.46 GHz, each target was observed for approximately 30 s. The integration times were typically 100 s at 22.46 GHz and 120 s at 43.34 GHz. All VLA/EVLA flux density measurements were calibrated using standard values for one or both of the primary calibrator sources used by NRAO (3C 48 or 3C 286), and the *uv* data were flagged, calibrated and imaged using standard NRAO software, *AIPS* or *CASA*. The VLA and EVLA were in different configurations at different times in the several months duration of the observations. As a consequence, the angular resolution changed. In addition, for a given configuration, the resolution was much finer at higher frequencies. For that reason, sources that showed signs of resolution in any VLA configuration or at any VLA frequency have been carefully flagged.

The *Planck*-ATCA Co-eval Observations (PACO) project (Massardi et al. 2011a) consists of observations of a compilation of sources selected in the Australia Telescope 20 GHz survey (AT20G; Massardi et al. 2011b) taken with the Australia Telescope Compact Array (ATCA) in the frequency range 4.5–40 GHz. The observations were carried out at several epochs close in time with *Planck* satellite observations covering July 2009–August 2010. The PACO sample is a complete, flux-density limited, and spectrally-selected sample over the whole southern sky, with the exception of the region with Galactic latitude $|b| < 5°$.

The Simultaneous Medicina *Planck* Experiment (SiMPlE; Procopio et al. 2011) uses the 32-m Medicina single-dish antenna at 5 and 8.3 GHz to observe the 263 sources of the New Extragalactic WMAP Point Source (NEWPS) sample (Massardi et al. 2009) with $\delta > 0°$, and partially overlapping with the PACO observations for $-10° < \delta < 0°$. The project began in June 2010. Because of the lack of simultaneity with the ERCSC, the data have been used here to match the PACO observations in the overlapping region and to add information for $\delta > 70°$, a region so far poorly covered at 5 GHz.

Twelve sources from our sample were observed in the submillimetre domain with the 12-m Atacama Pathfinder EXperiment (APEX) in Chile. The observations were made using the LABOCA bolometer array centred at 345 GHz. Data were taken at two epochs in 2009: September 3–4 2009 and November 12 2009. The data were reduced using the script

package *minicrush*[3], version 30-Oct.-2009, with Uranus used as calibrator.

3.2. Optical data

The optical observations were made with the 35-cm KVA (Kungliga Vetenskapsakademien) telescope on La Palma, Canary islands. All observations were made through the *R*-band filter ($\lambda_{eff} = 640$ nm) using a Santa Barbara ST-8 CCD camera with a gain factor of 2.3 e$^-$/ADU and readout noise of 14 electrons. The binning of pixels by 2×2 pixels resulted in a plate scale of 0″.98 per pixel. We obtained three to six exposures of 180 s per target. The images were reduced in the standard way of subtracting the bias and dark frames and dividing by twilight flat-fields.

The flux densities of the target and three to five stars in the target field were measured with aperture photometry and the magnitude difference between the target and a primary reference star in the same field was determined. Using differential mode makes the observations insensitive to variations in atmospheric transparency and accurate measurements can be obtained even in partially cloudy conditions. The *R*-band magnitude of the primary reference star was determined from observations made on photometric nights, using comparison stars in known blazar fields as calibrators (Fiorucci & Tosti 1996; Fiorucci et al. 1998; Raiteri et al. 1998; Villata et al. 1998; Nilsson et al. 2007) and taking into account the color term of the *R*-band filter employed. After the *R*-band magnitude of the primary reference star was determined, the object magnitudes were computed from the magnitude differences. At this phase we assumed $V - R = 0.5$ for the targets. Several stars in the field were used to check the quality of the photometry and stability of the primary reference. The uncertainties in the magnitudes include the contribution from both measurement and calibration errors.

The monitoring at Xinglong Station, National Astronomical Observatories of China, was performed with a 60/90-cm f/3 Schmidt telescope. The telescope is equipped with a 4096×4096 E2V CCD, which has a pixel size of 12 μm and a spatial resolution of 1″.3 per pixel. The observations were made with an *i* filter. Its central wavelength and passband width are 668.5 and 51.4 nm, respectively. The exposure times are mostly 120 s but can range from 60 to 180 s, depending on weather and moon phase.

3.3. Swift

The *Swift* Gamma-Ray-Burst (GRB) Explorer (Gehrels et al. 2004) is a multi-frequency space observatory devoted to the discovery and rapid follow up of GRBs. There are three instruments on board the spacecraft: the UV and Optical Telescope (UVOT, Roming et al. 2005), the X-Ray Telescope (XRT, Burrows et al. 2005) sensitive in the 0.3–10.0 keV band, and the Burst Alert Telescope (BAT, Barthelmy et al. 2005) sensitive in the 15–150 keV band. Although the primary scientific goal of the satellite is the observation of GRBs, the wide frequency coverage is useful for AGN studies because it covers the region where the transition between synchrotron and inverse Compton emission usually occurs.

When not engaged in GRB observations, *Swift* is available for target of opportunity (ToO) requests. The *Swift* team decided to devote an average of three ToO per week to the simultaneous observations of *Planck* AGN. The simultaneity of

---

[3] http://www.submm.caltech.edu/~sharc/crush/

Swift observations within two weeks to the *Planck* first or second scan, or both, is shown in Table 4, marked sim_1st, sim_2nd, or sim_1st_2nd, respectively.

3.3.1. UVOT

Swift UVOT observations were carried out using the "filter of the day", i.e., one of the lenticular filters (*V*, *B*, *U*, *UVW1*, *UVM2*, and *UVW2*), unless otherwise specified in the ToO request. Therefore images are not always available for all filters.

The photometry analysis of all our sources was performed using the standard UVOT software distributed within the *HEAsoft 6.8.0* package, and the calibration included in the latest release of the "Calibration Database" (CALDB). A specific procedure has been developed to process all the ToO observations requested by the *Planck* project. Counts were extracted from an aperture of 5″ radius for all filters and converted to flux densities using the standard zero points (Poole et al. 2008). The flux densities were then de-reddened using the appropriate values of $E(B - V)$ for each source taken from Schlegel et al. (1998), with $A_\lambda/E(B - V)$ ratios calculated for UVOT filters using the mean galactic interstellar extinction curve from Fitzpatrick (1999). No variability was detected within single exposures in any filter.

3.3.2. XRT

The XRT is usually operated in "Auto State" mode which automatically adjusts the CCD read-out mode to the source brightness, in an attempt to avoid pile-up (see Burrows et al. 2005; Hill et al. 2004, for details of the XRT observing modes). As a consequence, part of the data sample was collected using the most sensitive Photon Counting (PC) mode while Windowed Timing (WT) mode was used for bright sources.

The XRT data were processed with the *XRTDAS* software package (v. 2.5.1, Capalbi et al. 2005) developed at the ASDC and distributed by the NASA High Energy Astrophysics Archive Research Center (HEASARC) within the *HEASoft* package (v. 6.9). Event files were calibrated and cleaned with standard filtering criteria with the *xrtpipeline* task, using the latest calibration files available in the *Swift* CALDB. Events in the energy range 0.3−10 keV with grades 0−12 (PC mode) and 0−2 (WT mode) were used for the analysis.

Events for the spectral analysis were selected within a circle of a 20-pixel (∼47″) radius, centred on the source position, which encloses about 90% of the point spread function (PSF) at 1.5 keV (Moretti et al. 2005). For PC mode data, when the source count rate is above ∼0.5 counts/s data are significantly affected by pile-up in the inner part of the PSF. For such cases, after comparing the observed PSF profile with the analytical model derived by Moretti et al. (2005), we removed pile-up effects by excluding events detected within a certain inner radius around the source position, and used an outer radius of 30 pixels. The value of the inner radius was evaluated individually for each observation affected by pile-up, depending on the observed source count rate.

Ancillary response files were generated with the *xrtmkarf* task applying corrections for the PSF losses and CCD defects. Source spectra were binned to ensure a minimum of 20 counts per bin to allow the χ^2 minimization fitting technique to be used. We fitted the spectra adopting an absorbed power-law model with photon index Γ_x. When deviations from a single power-law model were found, we adopted a log-parabolic law of the form

$F(E) = KE^{-(a+b\log(E))}$ (Massaro et al. 2004) which has been shown to fit the X-ray spectrum of blazars well (e.g., Giommi et al. 2005; Tramacere et al. 2009). This spectral model is described by only two parameters: *a*, the photon index at 1 keV, and *b*, the curvature of the parabola. For both models the amount of hydrogen-equivalent column density (N_H) was fixed to the Galactic value along the line of sight (Kalberla et al. 2005).

3.4. Fermi-LAT observations and data analysis

The Large Area Telescope (LAT) onboard *Fermi* is an electron-positron pair-conversion telescope sensitive to gamma-rays of energies from 20 MeV to above 300 GeV. The *Fermi*-LAT consists of a high-resolution silicon microstrip tracker, a CsI hodoscopic electromagnetic calorimeter, and an anticoincidence detector for charged particles background identification. A full description of the instrument and its performance can be found in Atwood et al. (2009). The large field of view (∼2.4 sr) allows the LAT to observe the full sky in survey mode every 3 h. The LAT PSF strongly depends on both the energy and the conversion point in the tracker, but less on the incidence angle. For 1 GeV normal incidence conversions in the upper section of the tracker, the PSF 68% containment radius is 0.6°.

The *Fermi*-LAT data considered for this analysis cover the period from 4 August 2008 to 4 November 2010. They have been analyzed using the standard *Fermi*-LAT ScienceTools software package[4] (version v9r16) and selecting for each source only photons above 100 MeV, belonging to the diffuse class (Pass6 V3 IRF, Atwood et al. 2009) which have the lowest background contamination. For each source, we selected only photons within a 15° region of interest (RoI) centred around the source itself. In order to avoid background contamination from the bright Earth limb, time intervals where the Earth entered the LAT Field of View (FoV) were excluded from the data sample. In addition, we have excluded observations in which the source was viewed at zenith angles larger than 105°, where Earth's albedo gamma-rays increase the background contamination. The data were analyzed with a binned maximum likelihood technique (Mattox et al. 1996) using the analysis software (*gtlike*) developed by the LAT team[5]. A model accounting for the diffuse emission as well as the nearby gamma-ray sources is included in the fit.

The diffuse foreground, including Galactic interstellar emission, extragalactic gamma-ray emission, and residual cosmic ray (CR) background, has been modelled using the models[6] *gll_iem_v02* for the Galactic diffuse emission and *isotropic_iem_v02* for the extra-galactic isotropic emission. Each source has been fit with a power law function

$$\frac{\mathrm{d}N}{\mathrm{d}E} = \frac{N(\gamma + 1)E^\gamma}{E_{\max}^{\gamma+1} - E_{\min}^{\gamma+1}} \qquad (1)$$

where both the normalization factor N and the photon index γ are left free in the model fit. The model also includes all the sources within a 20° RoI included in the *Fermi*-LAT one year catalogue (Abdo et al. 2010b), modelled using power law functions. If a source included in the model is a pulsar belonging to the *Fermi* pulsar catalog (Abdo et al. 2010d), we have modelled

---

[4] http://fermi.gsfc.nasa.gov/ssc/data/analysis/documentation/Cicerone/

[5] http://fermi.gsfc.nasa.gov/ssc/data/analysis/documentation/Cicerone/Cicerone_Likelihood

[6] http://fermi.gsfc.nasa.gov/ssc/data/access/lat/BackgroundModels.html

the source using a power-law with exponential cut-off and the spectral parameters from the pulsar catalogue. For the evaluation of the gamma-ray SEDs, the whole energy range from 100 MeV to 300 GeV is divided into two equal logarithmically spaced bins per decade. In each energy bin the standard *gtlike* binned analysis has been applied assuming for all the point sources in the model a power law spectrum with photon index fixed to −2.0. Assuming that in each energy bin the spectral shape can be approximated by a power law, the flux density of the source in all selected energy bins was evaluated, requiring in each energy bin a test statistic (TS)[7] greater than 10. If the TS is lower than 10, an upper limit is evaluated in that energy bin. Only statistical errors for the fit parameters are shown in the plots. Systematic effects are mainly based on uncertainties in the LAT effective area derived from the on-orbit estimations, and are <5% near 1 GeV, 10% below 0.10 GeV, and 20% above 10 GeV.

The LAT gamma-ray spectra of all AGN detected by *Fermi* are studied in Abdo et al. (2010c), based on 11 months of *Fermi*-LAT data. For this paper, we derived the gamma-ray SEDs of the 104 sources in the sample in three time intervals, presented in Table 4. In the first interval the *Fermi*-LAT observations are simultaneous to the *Planck* first or second scan, or both, within two weeks (marked sim_1st, sim_2nd, or sim_1st_2nd in Table 4). The *Fermi*-LAT data have in this case been integrated over two weeks. In the second interval the gamma-ray data are quasi-simultaneous to the *Planck* first or second scan, or both, having been integrated over two months (2M_1st, 2M_2nd, or 2M_1st_2nd in Table 4). In the third interval are sources for which *Fermi*-LAT data have been averaged over 27 months due to their faintness (27 m in Table 4).

Note that eight sources (0306+102, 0355+508, 0804+499, 0945+408, J1130+3815, 1413+135, 1928+738, 2005+403) that appear as significant gamma-ray detections in the 27 month dataset presented in this work, have not been included in any *Fermi* catalogue published so far (Abdo et al. 2010b). They can be considered new gamma-ray emitting sources, taking into account the possibility that their association with the radio source is purely spatial.

4. Spectral energy distributions

The SEDs for the whole sample are shown in Figs. 18−121 (in panels on the left). The *Planck* measurements and the simultaneous auxiliary data are indicated by red circles. The grey points represent archival data obtained from the literature and using the ASDC search tool. The measurements were regarded as simultaneous if they were taken within two weeks (for radio frequencies) or five days (for optical and higher energies) of the *Planck* measurement. Previous studies of the radio variability of blazars (Hovatta et al. 2008; Nieppola et al. 2009) have shown that the two-week simultaneity limit is appropriate, as large-scale radio flux density changes on that timescale are quite rare. The SEDs were fitted with second and third degree polynomials, namely

$$\log \nu F_\nu = c_1 (\log \nu)^2 + c_2 (\log \nu) + c_3, \qquad (2)$$

and

$$\log \nu F_\nu = c_4 (\log \nu)^3 + c_5 (\log \nu)^2 + c_6 (\log \nu) + c_7, \qquad (3)$$
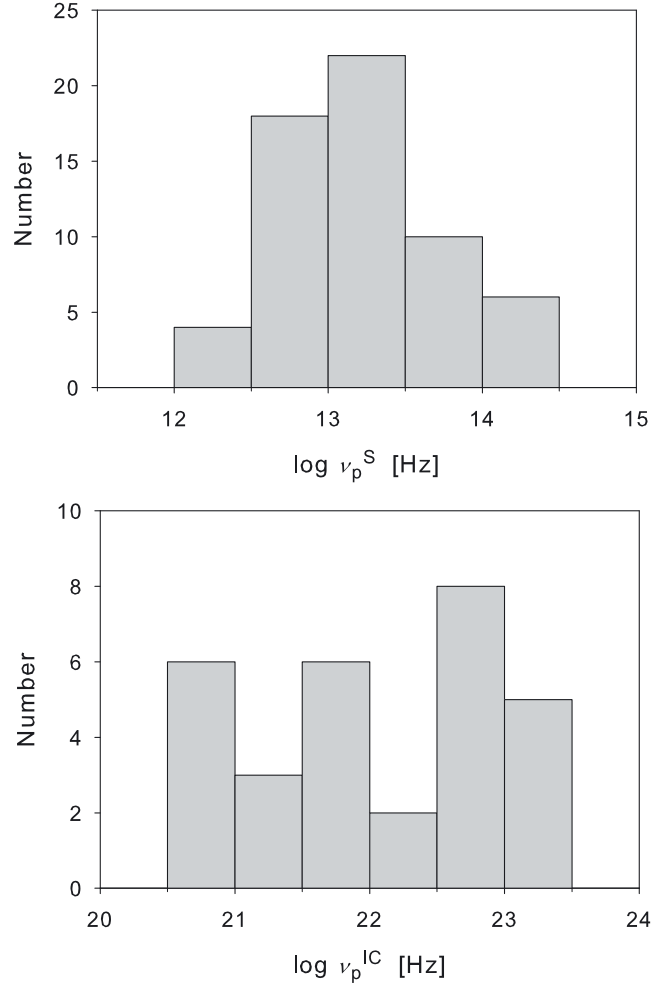
Fig. 1. The distributions of the synchrotron (*top panel*) and IC (*bottom panel*) peak frequencies.

where c_i ($i = 1 \ldots 7$) are fit parameters. We calculated the peak frequencies of the components from the third degree fit by default and used the second degree fit only if it seemed by visual inspection to be more accurate. Typically, in these cases, the third degree fit would not yield a sensible result at all. In the SEDs in Figs. 18−121, third degree fits are marked with a dashed line, second degree fits with a dotted line.

The fits were divided into two classes, A and B, according to the fit quality, A being superior. We emphasize that this division is the subjective view of the authors, and is only meant to illustrate the varying quality of the SED fits. The classes have not been used in calculating the correlation coefficients (see below). We were able to obtain meaningful synchrotron fits for 60 sources (15 class A fits), and IC fits for 30 sources (10 class A fits). For 21 sources we were able to fit both components. The synchrotron and IC peak frequencies are listed in Table 1. Columns 9 and 10 give the peak frequency and the fit quality for the synchrotron component, and Cols. 11 and 12 give the peak frequency and the fit quality for the inverse Compton component.

Figure 1 shows the distributions of the logarithms of the peak frequencies. The synchrotron peak frequencies, $\log \nu_p^S$, are typically very low, as we are dealing with bright radio sources. They range over two orders of magnitude, from 12.2 to 14.3, the average of the distribution being 13.2 ± 0.5. The source with the highest ν_p^S in the near-ultraviolet domain is 0716+714. The
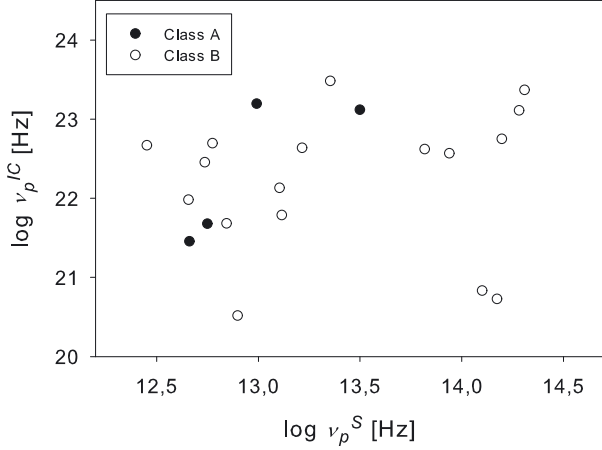
Fig. 2. The correlation of the peak frequencies of the synchrotron and the IC components. Solid circles denote class A fits, and open circles class B fits.

IC peak frequencies, $\log \nu_p^{\mathrm{IC}}$, range over three orders of magnitude, from MeV to the high GeV gamma-ray region. The distribution average is 22.0 ± 0.9. The source with the highest IC peak frequency is 1156+295, with $\log \nu_p^{\mathrm{IC}} = 23.5$. The source with the lowest IC peak frequency, with $\log \nu_p^{\mathrm{IC}} = 20.5$, is 0836+710.

We have plotted the interdependence of the component peaks in Fig. 2. The two peak frequencies seem to have no significant correlation, which is confirmed by the Spearman rank correlation test ($\rho = 0.301$, $P = 0.092$, both class fits included). There is, however, a tendency for the sources with high ν_p^{S} to have a high ν_p^{IC}. In the synchrotron-self-Compton (SSC) scenario, the separation of the component peaks depends on many factors, such as the electron Lorentz factors, magnetic field strengths, and particle densities. Therefore the lack of correlation as such does not allow any strong statements to be made about the origin of the IC radiation (SSC, or external Compton, EC).

We also compared our peak frequencies with those of Abdo et al. (2010a). These comparisons are illustrated in Fig. 3, where the one-to-one correspondence is shown with a dashed line. Both correlations are significant according to the Spearman test ($\rho = 0.629$, $P = 0.003$ for the synchrotron peaks and $\rho = 0.660$, $P = 0.010$ for the IC ones).

5. Radio spectra

In addition to the SEDs, we have plotted the standard radio spectra for the sample sources. The aim was to look for signs of multiple components contributing to the synchrotron emission. The spectra are shown in Figs. 18−121 (in panels on the right). Red circles indicate low frequency (LF; $\leq$70 GHz) data simultaneous to *Planck*, red stars indicate ERCSC LFI data, blue circles indicate high frequency (HF; >70 GHz) data simultaneous to *Planck*, and blue stars indicate ERCSC HFI data. As can be seen, the *Planck* data and the supporting multifrequency data provide an excellent opportunity to find the signatures of possible multiple components or anomalous spectral shapes. A statistical study of extragalactic radio sources in the ERCSC is presented in Planck Collaboration (2011i), and SEDs of extreme radio sources, such as gigahertz-peaked spectrum (GPS) sources in Planck Collaboration (2011j).

In Figs. 4 and 5 we have plotted the distributions of the LF and HF spectral indices using only the *Planck* data for the latter. When plotting the HF α values, we have only taken into account
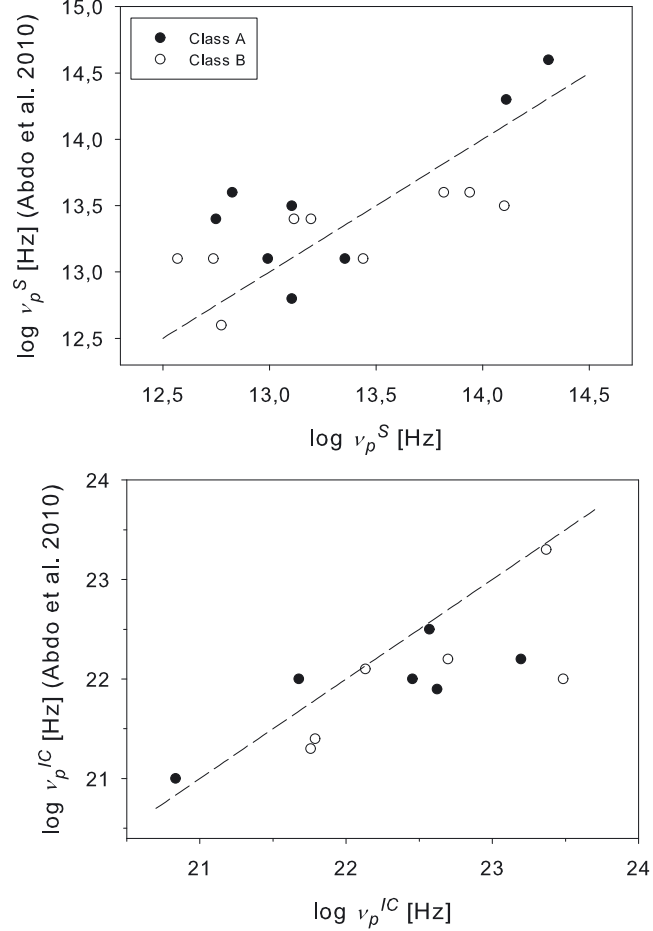
Fig. 3. Comparison between our synchrotron and IC peak frequencies and those of Abdo et al. (2010a). The synchrotron peak frequencies are shown in *the top panel* and IC peak frequencies in *the bottom panel*. The dashed lines illustrate the one-to-one correspondence. Solid circles denote class A fits, and open circles class B fits.

those sources with three or more data points. This leaves us with 84 sources out of the 104. The sources with only one *Planck* scan are shown hatched in Figs. 4 and 5. Figure 6 shows α_{LF} versus α_{HF}. As expected, the LF indices are fairly flat, with an average of −0.06. Their distribution is narrow, with 91% of the indices being in the range $\alpha_{\mathrm{LF}} = -0.5$−0.5. There are a couple of sources with remarkably steep LF spectra, namely 0552+398 and 2021+614, both having $\alpha_{\mathrm{LF}} \leq -0.8$. At the other end we have 0007+106 which has an inverted spectrum with $\alpha_{\mathrm{LF}} = 0.86$. Also 1228+126 has a steep spectrum, although the fit value may be exaggerated in this case (see Fig. 75). For clarity, this source has been omitted from Figs. 4 and 6.

The HF indices are concentrated around −0.5, having an average of −0.56. Rather similar distributions for LF and HF spectral indices were found in Planck Collaboration (2011i), especially in their Fig. 7. However, a large part of the α_{HF} distribution is in the flat domain with $\alpha_{\mathrm{HF}} \geq -0.5$. Extreme examples are 1413+135 ($\alpha_{\mathrm{HF}} = 0.02$) and 0954+658 ($\alpha_{\mathrm{HF}} = 0.34$). It is unexpected that the spectral indices of blazars at sub-millimetre and FIR frequencies should be this flat. Only 28 of the 84 sources with HF spectral fits shown in Figs. 18−121 have $\alpha < -0.7$, the "canonical" value for optically thin spectra, corresponding to an electron energy index s of about 2.4. This has two possible explanations: either the total HF spectra are defined by several underlying components, or the energy spectrum of the electron
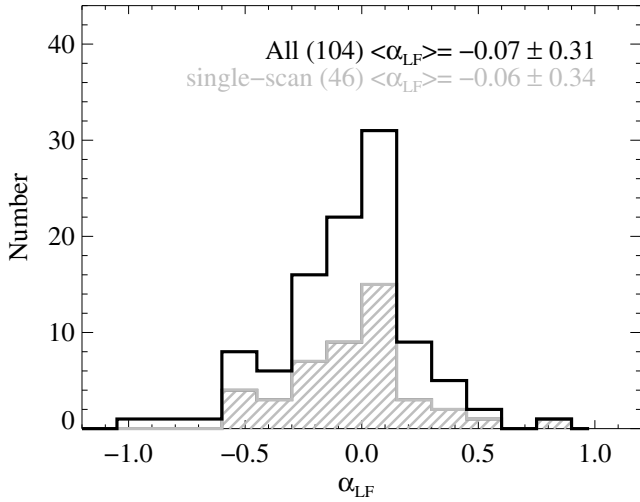
Fig. 4. Distribution of LF spectral indices for the whole sample (104 sources). The sources that have only been scanned once by *Planck* are shown hatched (46 sources).
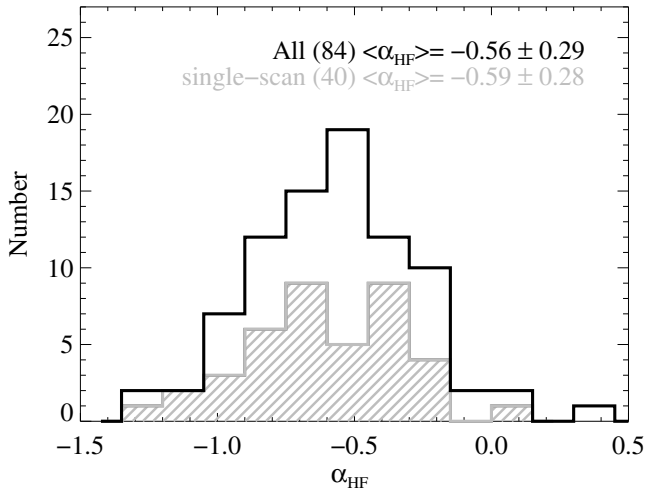
Fig. 5. Distribution of HF spectral indices for the 84 sources that had three or more data points. The sources that have only been scanned once by *Planck* are shown hatched (40 sources).

Fig. 6. LF spectral indices α_{LF} versus HF spectral indices α_{HF} for the various AGN subclasses.
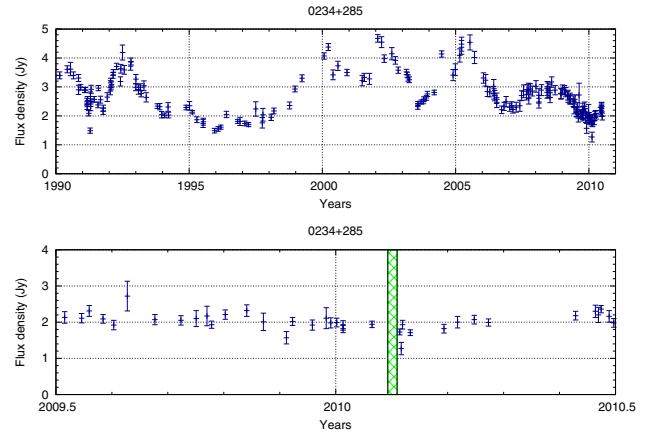
Fig. 7. The 37 GHz lightcurve of 0234+285, measured at Metsähovi Radio Observatory, showing continuous variability. The period when *Planck* was observing the source is indicated by the hatched region in *the lower panel*, which is a blow-up of the last year.

population producing the radiation is much harder than generally assumed. Although some HF spectra show evidence for several sub-components or even an upturn at the highest frequencies, many others appear to be perfectly straight and therefore perhaps originate from a single optically thin component. At the highest *Planck* frequencies the lifetimes of radiating electrons are short, and one would in most cases expect to see the optically thin spectra steepened by energy losses, with indices ranging from the original α_{thin} to $\alpha_{thin} - 0.5$ and beyond. This makes spectral indices > -0.7 even more remarkable.

To rule out contamination by dust in the host galaxies, we have estimated the possible contribution of an extremely bright submillimetre galaxy. We also estimated the flux densities of 2251+158 at several submillimetre bands in the case its luminosity were similar to the submillimetre galaxy. The comparison shows that if the dust component in 2251+158 were of the same brightness as in the extremely bright submillimetre galaxy, its emission would be completely swamped by the non-thermal emission from the jet. The LF and HF spectral indices have been calculated using ERCSC data which for most sources is

an average of two *Planck* scans separated by about six months. However, the HF spectral index distribution for the sources that have been observed only once by *Planck* is quite similar to that of the whole sample. The implications of this result are discussed in more detail in Sect. 7.

As Fig. 6 shows, BLOs, HPQs and LPQs have different α_{HF} distributions. In Table 5 we have listed the average spectral indices for both frequency ranges for all subgroups. The LF spectra of radio galaxies are very steep on average, but the value is greatly influenced by the uncertain fit of 1228+126. If this source is left out of the calculations, the average α_{LF} for galaxies is 0.10 ± 0.52. LPQs have the steepest spectra in the HF range. However, the standard deviations of the samples are substantial, which can also be seen as the large scatter in Fig. 6. To quantify the possible differences between the AGN classes, we ran the Kruskal-Wallis ANOVA test. For the LF indices we could find no significant differences. However, in the case of the HF indices, the distributions of the subgroups differ significantly ($P < 0.001$). Multiple-comparisons test with t distribution tells us that LPQs differ from all other subgroups ($P \leq 0.031$). Also, BLO indices have a different distribution from all quasar subgroups ($P \leq 0.019$).

Table 5. Average spectral indices for AGN subclasses.

Class	Number LF	Number HF	Average α_{LF}	Average α_{HF}
BLO	21	20	-0.01 ± 0.25	-0.34 ± 0.26
HPQ	33	28	-0.06 ± 0.22	-0.58 ± 0.27
LPQ	21	18	-0.08 ± 0.30	-0.80 ± 0.27
QSO	19	10	-0.05 ± 0.28	-0.57 ± 0.26
GAL	9	7	-0.25 ± 0.66	-0.55 ± 0.19

Notes. The errors correspond to one standard deviation.

6. Modelling the SEDs and spectra of blazars

Spectral energy distributions rapidly became one of the main tools for understanding blazar physics after the EGRET instrument aboard the *Compton* Gamma-Ray Observatory (CGRO) satellite discovered strong gamma-ray emission from 3C 279 (Hartman et al. 1992) and, subsequently, from a large number of other radio-bright AGN. It was rapidly accepted that the double-peaked overall shape of the radio-to-gamma SED was due to synchrotron and inverse Compton radiation, but beyond this the agreement ended. The data simply lacked the sensitivity and the time coverage to sufficiently constrain the models. Even the most detailed and convincing effort for 3C 279 (Hartman et al. 2001) could be criticized for unrealistic physical assumptions (Lindfors et al. 2005).

With the coming of the *Fermi* and *Swift* satellites, ground-based TeV telescopes, and other satellite data, the inverse Compton high-energy SED of a large number of AGN can now be determined with hugely improved accuracy and time coverage. This has initiated a new era of AGN modelling (e.g., Proceedings of the Workshop "*Fermi* meets Jansky: AGN in Radio and Gamma Rays"; Fermi meets Jansky 2010). However, since the IC spectrum is created by the relativistic electrons scattering either the synchrotron photons (SSC) or external photons (EC), accurate knowledge of the shape of the synchrotron component is essential for all realistic modelling. Here the *Planck* data are invaluable, since they provide the first simultaneous multifrequency coverage of the crucial radio-to-IR part of the synchrotron spectrum.

However, most of the ERCSC data are not suitable for detailed modelling, since they are averages of two spectra taken about six months apart. Considering the strong SED variability, accurate modelling can be done only with the final *Planck* datasets and their several individual scans. Here we limit ourselves to a short discussion of how *Planck* and supporting data can be used to improve our understanding of blazar physics.

The basic picture of a blazar is well established: a black hole surrounded by an accretion disk and a broad-line emitting region (BLR), and a relativistic jet which produces the lower-frequency bump of the SED through synchrotron emission. The jet is not totally stable; VLBI imaging shows how new components, identified as relativistic shocks in the jet, emerge from the radio core at intervals ranging from months to years. These growing and decaying shocks are also responsible for the total flux density variations in the radio-to-IR, and at least partly also in the optical regime. The important thing to note is that the synchrotron SED is rarely, if ever, the product of a single synchrotron-radiating component. The nature of the radio core is still being debated, as is the nature and the extent of the jet flow upstream of the radio core, between it and the black hole (e.g., Marscher & Jorstad 2010; Marscher et al. 2010). Shocked jet models (Marscher & Gear 1985; Hughes et al. 1989; Valtaoja et al. 1992) provide a good account of the multifrequency variations in the total flux

density. In the particular case of 3C 279, Lindfors et al. (2006) showed that the optical variations can also be moderately well explained as the higher-frequency part of the shock emission.

The origin of the IC component is a matter of intense debate. In the *CGRO* era, the favoured alternative was that the high-frequency radiation originates close to the black hole and the accretion disk, inside the BLR and well upstream of the radio core. With a strong radiation field external to the jet, external Compton is then likely to be the dominant emission mechanism. A minority view was that at least a part of the gamma-ray flaring comes from much farther out, at or downstream from the radio core. The evidence for this was that, statistically speaking, strong gamma-ray flaring tended to occur after the beginning of a millimetre flare (Valtaoja & Teräsranta 1996; Lähteenmäki & Valtaoja 2003) and after the ejection of a new VLBI component (Jorstad et al. 2001). Occurring well outside the BLR, SSC seems in this case to be the only viable emission mechanism, but on the other hand simple SSC models have generally failed to explain the gamma-ray emission, requiring unrealistically low magnetic field strengths in other than the extreme TeV BL Lac objects. With new *Fermi* data, the evidence for gamma-ray emission from the radio jet has strengthened (Kovalev et al. 2009; Pushkarev et al. 2010; León-Tavares et al. 2011; Nieppola et al. 2010; Tornikoski et al. 2010; Valtaoja et al. 2010), but the source of the upscattered photons remains a puzzle.

Most of the attempts to model the high-energy bump have adopted a "reverse engineering" method, starting from the secondary IC SED and not from the primary synchrotron SED. The original electron energy spectrum is considered to be rather freely adjustable, with parameters chosen to produce a good fit of the calculated IC spectrum to the observations within the assumed model. In most cases, the synchrotron spectrum is assumed to originate in a single homogeneous component, and often the spectrum is adjusted only to the optical data, without any attempt to explain the radio-to-IR part of the SED. There is not much observational or theoretical evidence for the actual physical existence of such an IR-to-optical component: it is simply assumed to be there, because it can produce the observed IC spectrum.

To some extent such an approach is justifiable if the gamma-rays originate upstream of the radio core, and are therefore not directly connected to the observed radio jet and shocks, and their lower-frequency synchrotron emission. However, even in this case physically more realistic models must take into account also the radio-to-IR part, for several reasons. First, whatever the exact mechanism, the radio shocks also contribute to the IC spectrum, and their contribution must be accounted for in the model fits. Assuming reasonable physical parameters, the shocks can quite often produce part or all of the observed X-ray emission through the SSC mechanism (e.g., Lindfors et al. 2006). Indeed, a standard method for estimating the physical parameters of VLBI components is to assume that the X-ray emission is produced through SSC (Ghisellini et al. 1993; Marscher 1987). Secondly, the components seen in the radio, especially in the *Planck* HFI regime, contribute to the optical synchrotron emission, and this contribution must be subtracted from the putative IR-to-optical component, which, as explained above, in many models generates the whole IC spectrum. For example, in the present sample, at least 0235+164, 0917+449, 0954+658, 2227−088, and especially 2251+158 show ongoing millimetre-to-submillimetre flaring, which leaves little room for any additional components between the highest *Planck* frequencies and
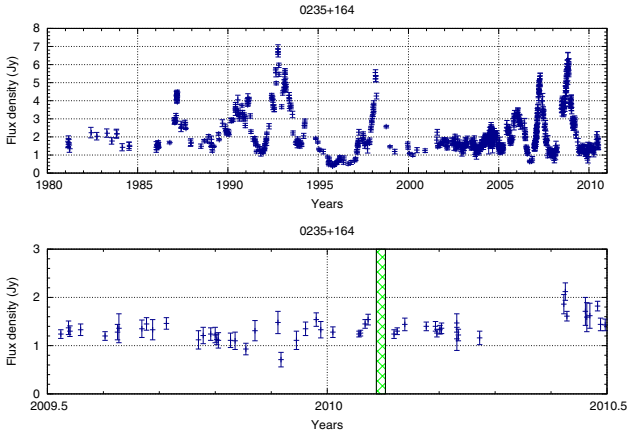
Fig. 8. The 37 GHz lightcurve of 0235+164, details as in Fig. 7.

the optical. This is the case in particular if the optically thin spectra are originally very flat, as we argue in Sects. 6.1 and 7.

On the other hand, if gamma-rays do come from the shocks at, or downstream from, the radio core, as increasing evidence indicates, the obvious first step is to model the shocks themselves and their spectra as accurately as possible using *Planck* and other radio data, and only after that attempt to calculate the IC radiation they produce.

Finally, it is clear that the more realistic multicomponent models, whatever their exact details, will give rather different physical parameter values than the single-component models. As an example, if the X-ray emission and the gamma-ray emission are not produced by a single component but by two (or even more) components, the derived electron energy spectral parameters will be quite different.

6.1. Some examples of different spectra and their implications

In this section we highlight five examples of different spectra of ERCSC sources which have been scanned only once by *Planck* and therefore have true snapshot spectra presented in Figs. 18−121. As stated before, our aim at this stage is not to model these sources, but to draw attention to some features commonly seen in the SEDs, and to their implications for future multi-epoch modelling of the *Planck* sources. We have fitted the radio-to-optical spectra with one or several standard self-absorbed sychrotron components (based on a power-law assumption for the electron energy spectrum). These are not model fits from a numerical, physical code (except for Figs. 16 and 17), but rather are meant to guide the eye and to illustrate the general shape of the radio-to-optical spectra.

We also use support observations to address the behaviour of the five example sources. In Figs. 7−11 we have plotted the 37 GHz long-term flux density curves for the five sources. The long-term data have been taken at Metsähovi Radio Observatory.

Even without numerical modelling we can address two important topics with these sources. The first one is the spectral flatness of the optically thin radiation possibly hinting at non-standard acceleration processes. The second one concerns the origin of the IC component. As Figs. 12−17 show there does not appear to be room for additional synchrotron components between the *Planck* and the optical frequencies. The IC radiation must therefore originate in the same shocks that also produce the radio emission, in contradiction to most theoretical models.
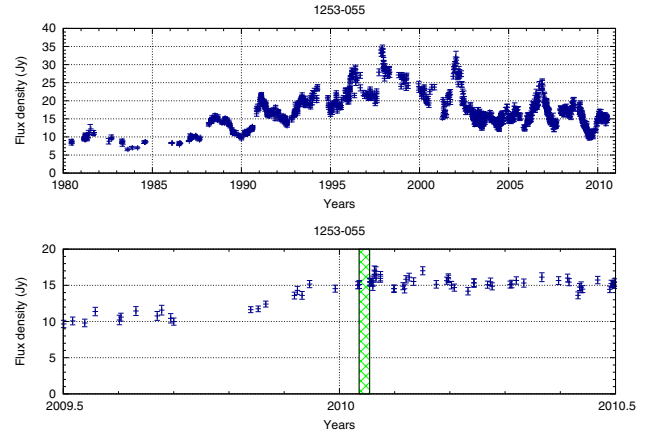
Fig. 9. The 37 GHz lightcurve of 1253−055 (3C 279), details as in Fig. 7.
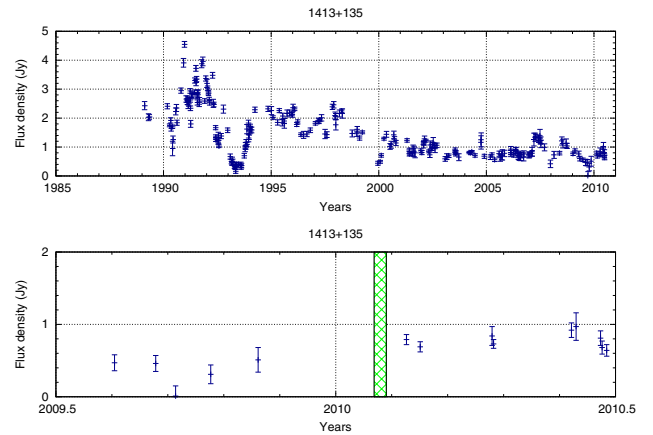
Fig. 10. The 37 GHz lightcurve of 1413+135, details as in Fig. 7.
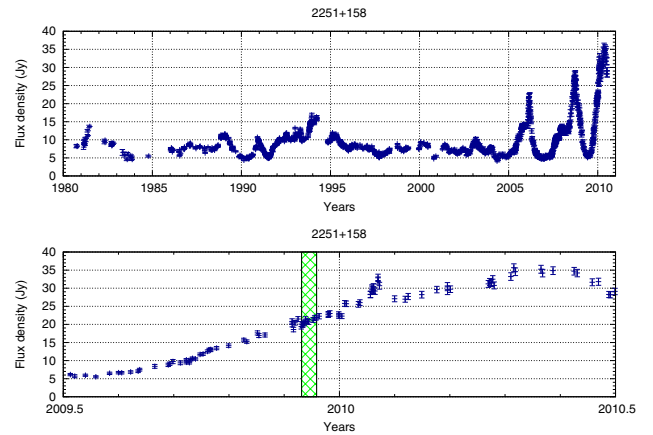
Fig. 11. The 37 GHz lightcurve of 2251+158 (3C 454.3), details as in Fig. 7.

0234+285 (Fig. 12). This source was in a very uneventful state during the *Planck* observing period (Fig. 7) and shows a spectrum typical of sources in a quiescent stage. The radio spectrum can be modelled with a single synchrotron component, having $\alpha_{thin} = -0.61$, which apparently steepens by $\Delta\alpha = -0.5$ and smoothly joins the optical spectrum (see also Fig. 29). This synchrotron component can be identified with the latest significant flare (new shock), which peaked about two years earlier at 37 GHz (Fig. 7). During low flux levels, in the absence of recent flares/shocks, the underlying, relatively stable
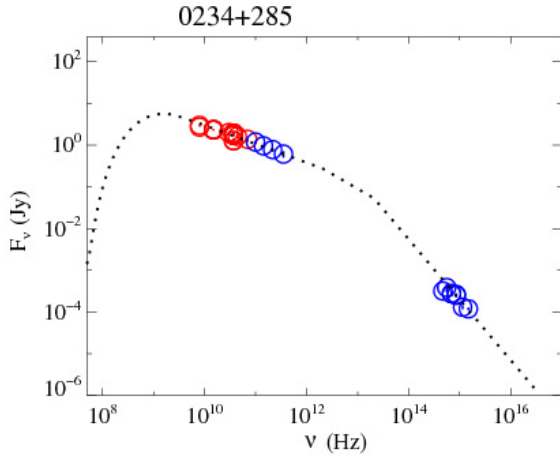
Fig. 12. A possible single-component spectrum for 0234+285 to illustrate the general shape. Red circles, LF data simultaneous to *Planck*; blue circles, HF data simultaneous to *Planck*.
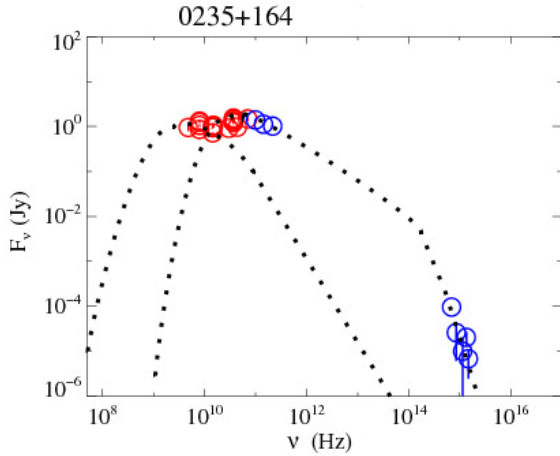
Fig. 13. A possible multiple-component spectrum for 0235+164 to illustrate the general shape. Symbols as in Fig. 12.
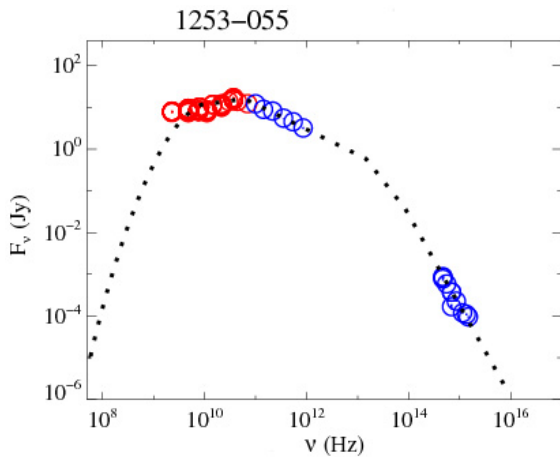
Fig. 14. The radio spectrum of 1253−055 shows that there is no room for another component between radio and optical regimes. Symbols as in Fig. 12.

Fig. 15. The radio spectrum of 1413+135 is very flat and can be fitted with multiple components. Symbols as in Fig. 12.
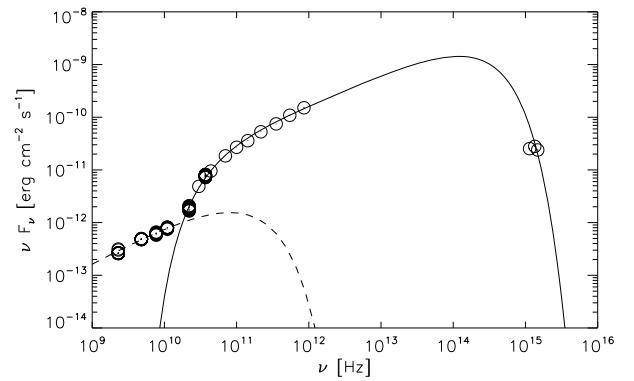
Fig. 16. The radio-optical SED of 2251+158 (3C 454.3) fitted with one component and synchrotron emission from the jet (dashed line) using a model by Tammi et al. (in prep.). The radio spectrum is shown in Fig. 17.
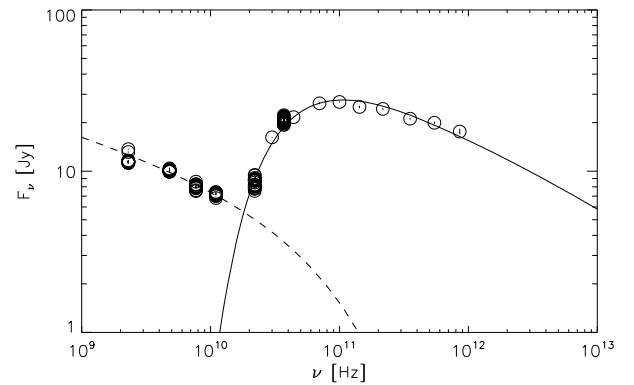
Fig. 17. A close-up of the radio spectrum and model fit of 2251+158 (3C 454.3), details as in Fig. 16.

jet may also contribute significantly to the synchrotron emission. Another similar example is the source 0007+106 (Fig. 19). Lacking mid-IR data, we cannot prove that there is no additional synchrotron component, between the *Planck* frequencies and the optical, that might be the main source of the IC flux (Fig. 29). However, the most straightforward interpretation of the data is that the IC flux also comes from the synchrotron component outlined in Fig. 12: from a rather old shock far downstream the jet, and far beyond the BLR.

0235+164 (Fig. 13). The bumpiness of the radio spectrum shows clear evidence of multiple components (shocks) contributing to the observed total flux density. We have outlined two possible synchrotron components, which together could explain most of the observed radio spectrum. Although 0235+164 was relatively quiescent during the *Planck* observation (Fig. 8), there were at least four strong flares during the previous five years, and they all are likely to be still contributing significantly to the total

radio flux density, at least around 10^{10} Hz and below. Assuming reasonable physical parameters for these shocks, they can also produce significant amounts of X-rays through the SSC mechanism, which must be accounted for in a proper multicomponent modelling of the IC spectrum. As with 0234+285, the higher-turnover component with $\alpha_{\rm thin} = -0.4$ can be joined smoothly to the optical spectrum assuming a steepening by about $\Delta\alpha = -0.5$, leaving no room for additional mid-IR components. *Fermi* measured only upper limits for the gamma-ray flux, which may be due to the fact that even the most recent shock, peaking around 100 GHz, is already about two years old (Fig. 8).

1253−055 (3C 279). (Fig. 14). Again, the highest-peaking radio component with $\alpha_{\rm thin} = -0.6$ can be made to smoothly join the steep optical spectrum. From Fig. 14 it is rather obvious that there can be no additional mid-IR components which might provide a significant contribution to the IC spectrum. If we assume that there is another synchrotron component turning over somewhere above the *Planck* frequencies and joining smoothly to the optical spectrum, Fig. 14 shows that its flux density cannot exceed the dashed line at any IR frequency between 10^{12} and $10^{14.5}$ Hz. This is the case even if we make the assumption that the spectrum of the component seen at the highest *Planck* frequencies steepens very rapidly above 857 GHz. Consequently, the *Fermi* gamma-rays must originate in the latest shock, which started a few months before the *Planck* observation (Fig. 9).

1413+135 (Fig. 15). This source exhibits a totally flat spectrum, with both the LF and the HF spectral indices approximately 0. Possible explanations are: an underlying electron energy index $s \approx 1$, which is rather unlikely; the superposition of many self-absorbed synchrotron components (shocks of various ages) with different turnover frequencies; or a continuous jet dominating the flux and having an integrated spectral index close to zero over a wide frequency range. As Fig. 10 shows, the source has been rather inactive for over a decade, with no major ourbursts. The HFI spectrum may indicate an upturn, hinting at the presence of an IR component. We show a possible spectral decomposition, including an IR-peaking component. Further *Planck* observations are needed to ascertain the reality and the nature of this component, which may be either a synchrotron flare seen at an early developmental stage or, possibly, an infrared dust component. The correct alternative can be identified through variability information.

2251+158 (3C 454.3). (Figs. 16 and 17). This source exhibits the most spectacular case of ongoing IR flaring, showing a very strong synchrotron component with a self-absorption turnover at about 80 GHz and a very flat ($\alpha = -0.2$) optically thin spectrum. As Fig. 11 shows, a series of spectacular flaring events has occurred in 2251+158 during the last five years, with *Planck* observing the source during the early stages of the strongest outburst ever seen in the source. In Fig. 16 we show a model fit to the radio-to-optical data, using a preliminary version of the code that we are developing (Tammi et al., in prep.). A close-up of the fit in the radio regime is shown in Fig. 17. As Fig. 119 also shows, it is impossible to squeeze in another component between the strong radio-IR flare and the optical regime. The gamma-ray emission must come from the growing shock that we see both in the total flux density monitoring curve (Fig. 11) and in the SED (Fig. 119). Most of the theoretical model scenarios assume that gamma-rays originate close to the black hole and the accretion disk, well within the BLR and far upstream of the radio core. This is not a viable alternative for 2251+158, in which gamma-rays must come from the new shock component, parsecs downstream from the radio core. As Fig. 11 shows, at the time of the *Planck* observation the shock had already been growing

for about half a year, which, changed into the source frame, translates into a distance $L = D^2 c (1 + z)^{-1} \Delta t_{\rm obs}$ (where D is the Doppler boosting factor, c the speed of light, z the redshift, and $\Delta t_{\rm obs}$ the time elapsed from the onset of the flare), of at least 10 pc down the jet, assuming a modest value of $D \approx 10$, or 90 pc using the value of $D = 33.2$ from Hovatta et al. (2009). This is the distance that the shock has moved downstream after emerging from the radio core.

7. The shape of the synchrotron spectrum: nonstandard acceleration mechanisms?

If the electron energy distribution is assumed to be a simple power-law with the form $N(E) = K E^{-s}$, the synchrotron spectrum of a single homogeneous source has an optically thick low-frequency part with a spectral index $\alpha = +2.5$, a turnover, and an optically thin part with a spectral index α related to the electron energy index by $\alpha = -(s - 1)/2$. Energy losses eventually cause the spectrum to steepen to $\alpha - 0.5$.

Since the earliest times of AGN research, the canonical value for α has been assumed to be about -0.75, corresponding to $s = 2.5$. Such an electron energy index emerges naturally from the simplest first-order *Fermi* acceleration mechanism, and blazars also tend to show slopes around this value at the high-frequency (10 to 100 GHz) end of the radio spectrum, where the sources are typically assumed to be optically thin. However, *Planck* data now challenge this commonly accepted view. As Fig. 4 shows, the LF spectral slopes are, in the main, quite flat, and sometimes even rising. It is likely that in most cases this results from the superposition of several distinct synchrotron components, since the spectra are generally not smooth, and we also know from VLBI observations that there are nearly always several components (shocks) present in any source (see also Sect. 6). The HF spectra (Fig. 5), on the other hand, are often straight within the *Planck* flux density error bars, and give a definite impression of optically thin radiation. In some cases, such as 2251+158, the spectrum even shows a clear self-absorption turnover at high frequencies, followed by a flat optically thin part with $\alpha = -0.2$ (Figs. 16 and 17).

The flatness of the HF spectra, shown in Fig. 5, is remarkable. Only a third of the sources have α steeper than -0.7, while 15 have $\alpha > -0.3$. While the present data are not sufficient to exclude the possibility that multiple components produce the flatness, and some sources such as 0954+658 do show evidence of an additional IR component (see also, e.g., Raiteri et al. 1999), we consider such an explanation unlikely for the whole sample. The errors in $\alpha_{\rm HF}$ cannot explain the very flat spectral indices, since they generally are smaller than $\Delta\alpha \approx 0.1$.

In Table 6 we list the 10 sources that fullfill the following criteria. They have been scanned only once by *Planck* and they have $\alpha_{\rm HF} > -0.5 + \Delta\alpha$, where $\Delta\alpha$ is the HF spectral fit error shown in Figs. 18−121. These form the most extreme end of the $\alpha_{\rm HF}$ distribution shown in Fig. 5. Three of them may show indications of multiple HF components in the spectra, but for the seven other sources the HF spectra appear to be straight within the *Planck* errors. If this is indeed the case, they cannot be explained with standard acceleration mechanisms with $s \geq 2$.

The rise of a submillimetre flare is quite fast (see, for example, the JCMT monitoring data of Stevens et al. 1994); the self-absorption turnover of a fresh shock component passes through the *Planck* HFI frequencies rather rapidly, and one therefore sees it only rarely in the snapshot high frequency spectra. (In the present data only 2251+158 is clearly such a case, although 0235+164 and 1652+398 might be others.) Instead, in most

Table 6. A list of the 10 sources scanned only once by *Planck* and with $\alpha_{HF} > -0.5 + \Delta\alpha$.

Source	α_{HF}	Spectral shape
0003−066	−0.38 ± 0.09	S
0059+581	−0.19 ± 0.09	S
0235+164	−0.40 ± 0.03	S
0430+052	−0.34 ± 0.05	S
1308+326	−0.41 ± 0.08	B?
1413+135	0.02 ± 0.12	B
1418+546	−0.16 ± 0.04	S
1652+398	−0.21 ± 0.04	B
1823+568	−0.31 ± 0.13	S
2251+158	−0.20 ± 0.02	S

Notes. S = straight HF spectrum; B = bumpy HF spectrum, possibly indicating multiple components.

cases we expect to see optically thin submillimetre spectra which have already experienced energy losses. Therefore the observed high-frequency spectral-index distribution of a sample of sources should show a range from $\alpha_{thin} = -(s-1)/2$ to $\alpha_{thin} - 0.5$ and beyond, as the exponential steepening sets in, with spectral indices steeper than the initial α_{thin} dominating. The observed distribution in Fig. 5 is thus incompatible with an initial α_{thin} around −0.7, as we should then see a few values around $\alpha = -0.7$ and a distribution peaking towards −1.2, reflecting the $\Delta\alpha = -0.5$ steepening due to energy losses.

Instead, the spectral index distribution is compatible with an electron index $s \approx 1.5$, resulting in a distribution of α_{thin} having smallest values around −0.2 to −0.3 and a maximum around −0.7. Such a suggestion of a very hard original electron spectrum is not entirely new; Valtaoja et al. (1988) studied the shock spectra and concluded that α is around −0.2, and Hughes et al. (1991) also concluded that the flux density variations can best be modelled with very hard spectra. Gear et al. (1994) also found that submillimetre spectra in a sample of 48 sources tended to be flat. Indeed, the distribution they found (their Fig. 7) is quite similar to ours (Fig. 5).

As noted above, alternative explanations for the α_{HF} distribution cannot be totally excluded. However, we consider sources such as 2251+158 (Figs. 16 and 17) to be compelling evidence for the existence of very hard non-standard electron spectra. The implications of this possibility are discussed below.

If the original α_{thin} really is around −0.2, the distribution shown in Fig. 5 becomes easy to understand: in many slightly older HFI components we see the expected spectral steepening from −0.2 to −0.7 and beyond. One way to test this hypothesis is to try to estimate the ages of the highest-frequency spectral components, either from their turnover frequencies or from the total flux density monitoring: the older the component, the lower the turnover frequency and the steeper the spectra. However, this analysis is beyond the scope of this paper and reliable conclusions require more *Planck* data than presently exist.

An electron energy spectral index as hard as 1.5 has major implications for the acceleration mechanisms dominating in blazar shocks. Particle acceleration efficiency is strongly governed by the compression ratio of the flow, which in turn is confined by well-known plasma physics, preventing the spectral index from becoming arbitrarily small. For a relativistic shock the traditional first-order *Fermi* mechanism usually produces spectral indices of 2.2 or so (and not 2.5, which follows from the nonrelativistic theory), but not smaller. There are a few options, however, for bypassing the $s \approx 2.2$ limit. For example, power-law spectra with $s \gtrsim 1$ have been found in certain kinds of oblique shocks (e.g., Kirk & Heavens 1989), as well as in parallel shocks in the case of large-angle particle scattering due to very strong turbulence (e.g., Stecker et al. 2007), or when the compression ratio felt by the particles is higher than that felt by the plasma (Ellison et al. 1990; Virtanen & Vainio 2005). The last alternative is an especially interesting one, because the combination of low density and relatively strong magnetic field – conditions likely to be found in Poynting-flux-dominated AGN jets – quickly leads to non-negligible Alfvén speeds and enhancement of the compression ratio felt by the particles and, consequently, to very hard particle spectra (Tammi 2008a,b, and references therein). High Alfvén speeds and scattering centres that are not frozen into the plasma also enable *second-order Fermi* acceleration, which can produce power-law spectra even with $s < 1$ in relativistic parallel shocks (Virtanen & Vainio 2005) and can work on time-scales comparable to the fastest blazar flares (Tammi & Duffy 2009).

As a simple order-of-magnitude reality check we can estimate the conditions required by the standard first-order acceleration in a parallel step shock in the presence of an increased scattering-centre compression ratio due to turbulence transmission (Vainio et al. 2003). Following the analysis of Tammi (2008b), we can estimate that in order to achieve $s \approx 1.5$ in a shock with Lorentz factor $\Gamma = 10$, magnetic field strength of the order of $0.02 - 2$ Gauss (depending on the composition and the density of the plasma) is needed. This is in good agreement with the usual modelling parameters of these sources, although we emphasise that the analysis used here is a simple one and may be limited to parallel shocks and weak turbulence.

8. Conclusions

We have presented the averaged *Planck* ERCSC spectra together with supporting ground and satellite observations obtained simultaneously with the *Planck* scans. The 104 SEDs, supplemented with archival data, demonstrate the usefulness of *Planck* data in determining the SED peak frequencies and fluxes and in modelling the SEDs in greater detail. In particular, the data demonstrate that the synchrotron spectrum contains contributions from several physically distinct AGN components: the LF and HF spectra are rarely smooth, except at the highest radio frequencies where the source component with the highest turnover becomes optically thin. The LF spectral indices cluster around $\alpha = 0$, also indicating the superposition of many components with different turnover frequencies. In modelling the synchrotron and inverse-Compton SEDs, a multicomponent approach is therefore necessary. While physical modelling is beyond the scope of this paper, which uses averaged, rather than single-epoch, *Planck* ERCSC flux densities, we have shown some examples of multicomponent decomposition of the SEDs and the conclusions that can be drawn from the data.

The sources display remarkable variability, which must also be taken into account in modelling the SEDs. We have presented some examples of total flux density monitoring to demonstrate how sources have been observed during *Planck* scans in different stages of activity.

The *Planck* HFI spectra are remarkably flat, with only a minority of sources having spectral indices steeper than the "canonical" $\alpha = -0.7$, and many apparently having α_{thin} around −0.2 to −0.4. We suggest that the most likely interpretation for the very flat and straight synchrotron spectra observed by *Planck* is a very hard original electron spectral energy index, clearly below $s = 2$. While this possiblity must be confirmed by future data, an index $s = 1.5$ is compatible with the HF spectral index

distribution seen in our sample. In a number of sources, energy losses steepen the HF spectra by $\Delta\alpha = 0.5$ from about -0.3 to about -0.8, and further to -1 and beyond, which can explain the observed distribution. The hardness of the electron spectrum would also mean that the synchrotron SED peak is in most cases related to the maximum electron Lorentz factor achieved in the acceleration process. The hard spectra also require a rethinking of the acceleration processes dominating in the relativistic jets and shocks.

For some sources the HF spectra are flat or even rising, indicating the presence of multiple synchrotron-emitting components peaking in the gigahertz to terahertz regime, and ongoing flaring at still higher frequencies. However, in many cases the *Planck* HFI spectrum appears to join the optical spectrum smoothly, leaving little room for additional still higher-frequency components. In these cases, the inverse-Compton gamma-rays must originate in the synchrotron (i.e., shock) components seen in the *Planck* data.

References

Abdo, A. A., Ackermann, M., Agudo, I., et al. 2010a, ApJ, 716, 30
Abdo, A. A., Ackermann, M., Ajello, M., et al. 2010b, ApJS, 188, 405
Abdo, A. A., Ackermann, M., Ajello, M., et al. 2010c, ApJ, 715, 429
Abdo, A. A., Ackermann, M., Ajello, M., et al. 2010d, ApJS, 187, 460
Acciari, V. A., Aliu, E., Arlen, T., et al. 2010, ApJ, 715, L49

Aliakberov, K., Mingaliev, M., Naugol'naya, M., et al. 1985, Astrophys. Issled. (Izvestiya SAO), 19, 60
Aller, H. D., Aller, M. F., Latimer, G. E., & Hodge, P. E. 1985, ApJS, 59, 513
Angelakis, E., Fuhrmann, L., Marchili, N., Krichbaum, T. P., & Zensus, J. A. 2008, Mem. Soc. Astron. Italiana, 79, 1042
Atwood, W. B., Abdo, A. A., Ackermann, M., et al. 2009, ApJ, 697, 1071
Baars, J. W. M., Genzel, R., Pauliny-Toth, I. I. K., & Witzel, A. 1977, A&A, 61, 99
Barthelmy, S. D., Barbier, L. M., Cummings, J. R., et al. 2005, Space Sci. Rev., 120, 143
Berlin, A., & Friedman, P. 1996, in 25th General Assembly of the International Union of Radio Science, 750
Bersanelli, M., Mandolesi, N., Butler, R. C., et al. 2010, A&A, 520, A4
Böttcher, M. 2010, in Fermi Meets Jansky – AGN at Radio and Gamma-Rays, ed. T. Savolainen, E. Ros, R. W. Porcas, & J. A. Zensus, 41 [arXiv:1006.5048]
Burrows, D. N., Hill, J. E., Nousek, J. A., et al. 2005, Space Sci. Rev., 120, 165
Capalbi, M., Perri, M., Saija, B., Tamburelli, F., & Angelini, L. 2005, available at http://heasarc.gsfc.nasa.gov/docs/swift/analysis/xrt_swguide_v1_2.pdf
Collmar, W., Böttcher, M., Krichbaum, T. P., et al. 2010, A&A, 522, A66
Ellison, D. C., Reynolds, S. P., & Jones, F. C. 1990, ApJ, 360, 702
Fermi meets Jansky 2010, in Proceedings of the Workshop, Fermi meets Jansky: AGN in Radio and Gamma Rays, ed. T. Savolainen, E. Ros, R. W. Porcas, & J. A. Zensus, Max-Planck-Institut für Radioastronomie, Bonn, Germany
Fiorucci, M., & Tosti, G. 1996, A&AS, 116, 403
Fiorucci, M., Tosti, G., & Rizzi, N. 1998, PASP, 110, 105
Fitzpatrick, E. L. 1999, PASP, 111, 63
Fossati, G., Celotti, A., Ghisellini, G., & Maraschi, L. 1997, MNRAS, 289, 136
Fossati, G., Maraschi, L., Celotti, A., Comastri, A., & Ghisellini, G. 1998, MNRAS, 299, 433
Fuhrmann, L., Zensus, J. A., Krichbaum, T. P., Angelakis, E., & Readhead, A. C. S. 2007, in The First GLAST Symposium, ed. S. Ritz, P. Michelson, & C. A. Meegan, Am. Inst. Phys. Conf. Ser., 921, 249
Fuhrmann, L., Krichbaum, T. P., Witzel, A., et al. 2008, A&A, 490, 1019
Gear, W. K., Stevens, J. A., Hughes, D. H., et al. 1994, MNRAS, 267, 167
Gehrels, N., Chincarini, G., Giommi, P., et al. 2004, ApJ, 611, 1005
Ghisellini, G., & Tavecchio, F. 2008, MNRAS, 387, 1669
Ghisellini, G., Padovani, P., Celotti, A., & Maraschi, L. 1993, ApJ, 407, 65
Ghisellini, G., Celotti, A., Fossati, G., Maraschi, L., & Comastri, A. 1998, MNRAS, 301, 451
Giommi, P., Piranomonte, S., Perri, M., & Padovani, P. 2005, A&A, 434, 385
Hartman, R. C., Bertsch, D. L., Fichtel, C. E., et al. 1992, ApJ, 385, L1
Hartman, R. C., Böttcher, M., Aldering, G., et al. 2001, ApJ, 553, 683
Hill, J. E., Burrows, D. N., Nousek, J. A., et al. 2004, in SPIE Conf. Ser. 5165, ed. K. A. Flanagan, & O. H. W. Siegmund, 217
Hovatta, T., Nieppola, E., Tornikoski, M., et al. 2008, A&A, 485, 51
Hovatta, T., Valtaoja, E., Tornikoski, M., & Lähteenmäki, A. 2009, A&A, 494, 527
Hughes, P. A., Aller, H. D., & Aller, M. F. 1989, ApJ, 341, 54
Hughes, P. A., Aller, H. D., & Aller, M. F. 1991, ApJ, 374, 57
Jorstad, S. G., Marscher, A. P., Mattox, J. R., et al. 2001, ApJ, 556, 738
Kalberla, P. M. W., Burton, W. B., Hartmann, D., et al. 2005, A&A, 440, 775
Kirk, J. G., & Heavens, A. F. 1989, MNRAS, 239, 995
Kovalev, Y. Y., Aller, H. D., Aller, M. F., et al. 2009, ApJ, 696, L17
Lähteenmäki, A., & Valtaoja, E. 2003, ApJ, 590, 95
Lamarre, J., Puget, J., Ade, P. A. R., et al. 2010, A&A, 520, A9
Leahy, J. P., Bersanelli, M., D'Arcangelo, O., et al. 2010, A&A, 520, A8
León-Tavares, J., Valtaoja, E., Tornikoski, M., Lahteenmaki, A., & Nieppola, E. 2011, A&A, 532, A146
Lindfors, E. J., Valtaoja, E., & Türler, M. 2005, A&A, 440, 845
Lindfors, E. J., Türler, M., Valtaoja, E., et al. 2006, A&A, 456, 895
Mandolesi, N., Bersanelli, M., Butler, R. C., et al. 2010, A&A, 520, A3
Marscher, A. P. 1987, in Superluminal Radio Sources, ed. J. A. Zensus, & T. J. Pearson, 280
Marscher, A. P., & Gear, W. K. 1985, ApJ, 298, 114
Marscher, A. P., & Jorstad, S. G. 2010 [arXiv:1005.5551]
Marscher, A. P., Jorstad, S. G., Larionov, V. M., et al. 2010, ApJ, 710, L126
Marshall, D. J., Robin, A. C., Reylé, C., Schultheis, M., & Picaud, S. 2006, A&A, 453, 635
Massardi, M., López-Caniego, M., González-Nuevo, J., et al. 2009, MNRAS, 392, 733
Massardi, M., Bonaldi, A., Bonavera, L., et al. 2011a, MNRAS, 415, 1597
Massardi, M., Ekers, R. D., Murphy, T., et al. 2011b, MNRAS, 412, 318
Massaro, E., Perri, M., Giommi, P., & Nesci, R. 2004, A&A, 413, 489
Mattox, J. R., Bertsch, D. L., Chiang, J., et al. 1996, ApJ, 461, 396
Mennella, A., Maino, D., Baccigalupi, C., et al. 2011, A&A, 536, A3

Moretti, A., Campana, S., Mineo, T., et al. 2005, in SPIE Conf. Ser. 5898, ed. O. H. W. Siegmund, 360

Nieppola, E., Tornikoski, M., & Valtaoja, E. 2006, A&A, 445, 441

Nieppola, E., Valtaoja, E., Tornikoski, M., Hovatta, T., & Kotiranta, M. 2008, A&A, 488, 867

Nieppola, E., Hovatta, T., Tornikoski, M., et al. 2009, AJ, 137, 5022

Nieppola, E., Tornikoski, M., Valtaoja, E., et al. 2010, in proceedings of the Workshop Fermi meets Jansky: AGN in Radio and Gamma Rays, ed. T. Savolainen, E. Ros, R. W. Porcas, & J. A. Zensus, Max-Planck-Institut für Radioastronomie, Bonn, Germany, 89

Nilsson, K., Pasanen, M., Takalo, L. O., et al. 2007, A&A, 475, 199

Padovani, P. 2007, Astrophys. Space Sci., 309, 63

Parijskij, Y. N. 1993, IEEE Antennas Propagation Magazine, 35, 7

Planck Collaboration 2011a, A&A, 536, A1

Planck Collaboration 2011b, A&A, 536, A2

Planck Collaboration 2011c, A&A, 536, A7

Planck Collaboration 2011d, A&A, 536, A8

Planck Collaboration 2011e, A&A, 536, A9

Planck Collaboration 2011f, A&A, 536, A10

Planck Collaboration 2011g, A&A, 536, A11

Planck Collaboration 2011h, A&A, 536, A12

Planck Collaboration 2011i, A&A, 536, A13

Planck Collaboration 2011j, A&A, 536, A14

Planck Collaboration 2011k, A&A, 536, A15

Planck Collaboration 2011l, A&A, 536, A16

Planck Collaboration 2011m, A&A, 536, A17

Planck Collaboration 2011n, A&A, 536, A18

Planck Collaboration 2011o, A&A, 536, A19

Planck Collaboration 2011p, A&A, 536, A20

Planck Collaboration 2011q, A&A, 536, A21

Planck Collaboration 2011r, A&A, 536, A22

Planck Collaboration 2011s, A&A, 536, A23

Planck Collaboration 2011t, A&A, 536, A24

Planck Collaboration 2011u, A&A, 536, A25

Planck Collaboration 2011v, The Explanatory Supplement to the Planck Early Release Compact Source Catalogue (ESA)

Planck Collaboration 2011w, A&A, 536, A26

Planck HFI Core Team 2011a, A&A, 536, A4

Planck HFI Core Team 2011b, A&A, 536, A6

Poole, T. S., Breeveld, A. A., Page, M. J., et al. 2008, MNRAS, 383, 627

Procopio, P., Massardi, M., Righini, S., et al. 2011, MNRAS, 417, 1123

Pushkarev, A. B., Kovalev, Y. Y., & Lister, M. L. 2010, ApJ, 722, L7

Raiteri, C. M., Villata, M., Lanteri, L., Cavallone, M., & Sobrito, G. 1998, A&AS, 130, 495

Raiteri, C. M., Villata, M., Tosti, G., et al. 1999, A&A, 352, 19

Richards, J. L., Max-Moerbeck, W., Pavlidou, V., et al. 2011, ApJS, 194, 29

Roming, P. W. A., Kennedy, T. E., Mason, K. O., et al. 2005, Space Sci. Rev., 120, 95

Rosset, C., Tristram, M., Ponthieu, N., et al. 2010, A&A, 520, A13

Sambruna, R. M., Gliozzi, M., Tavecchio, F., Maraschi, L., & Foschini, L. 2006, ApJ, 652, 146

Sambruna, R. M., Donato, D., Ajello, M., et al. 2010, ApJ, 710, 24

Schlegel, D. J., Finkbeiner, D. P., & Davis, M. 1998, ApJ, 500, 525

Stecker, F. W., Baring, M. G., & Summerlin, E. J. 2007, ApJ, 667, L29

Stevens, J. A., Litchfield, S. J., Robson, E. I., et al. 1994, ApJ, 437, 91

Tammi, J. 2008a, in International Cosmic Ray Conference, 2, 251

Tammi, J. 2008b, International Journal of Modern Physics D, 17, 1811

Tammi, J., & Duffy, P. 2009, MNRAS, 393, 1063

Tauber, J. A., Mandolesi, N., Puget, J., et al. 2010, A&A, 520, A1

Teräsranta, H., Tornikoski, M., Mujunen, A., et al. 1998, A&AS, 132, 305

Tornikoski, M., Nieppola, E., Valtaoja, E., León-Tavares, J., & Lähteenmäki, A. 2010, in Proceedings of the Workshop Fermi meets Jansky: AGN in Radio and Gamma Rays, ed. T. Savolainen, E. Ros, R. W. Porcas, & J. A. Zensus, Max-Planck-Institut für Radioastronomie, Bonn, Germany, 85

Tramacere, A., Giommi, P., Perri, M., Verrecchia, F., & Tosti, G. 2009, A&A, 501, 879

Vainio, R., Virtanen, J. J. P., & Schlickeiser, R. 2003, A&A, 409, 821

Valtaoja, E., & Teräsranta, H. 1996, A&AS, 120, 491

Valtaoja, E., Haarala, S., Lehto, H., & Valtaoja, L. 1988, A&A, 203, 1

Valtaoja, E., Teräsranta, H., Urpo, S., et al. 1992, A&A, 254, 71

Valtaoja, E., Tornikoski, M., León-Tavares, J., et al. 2010, in Proceedings of the Workshop Fermi meets Jansky: AGN in Radio and Gamma Rays, ed. T. Savolainen, E. Ros, R. W. Porcas, & J. A. Zensus, Max-Planck-Institut für Radioastronomie, Bonn, Germany, 73

Verkhodanov, O. V. 1997, in Astronomical Data Analysis Software and Systems VI, ed. G. Hunt, & H. Payne, ASP Conf. Ser., 125, 46

Villata, M., Raiteri, C. M., Lanteri, L., Sobrito, G., & Cavallone, M. 1998, A&AS, 130, 305

Virtanen, J. J. P., & Vainio, R. 2005, ApJ, 621, 313

Zacchei, A., Maino, D., Baccigalupi, C., et al. 2011, A&A, 536, A5

[1] Aalto University Metsähovi Radio Observatory, Metsähovintie 114, 02540 Kylmälä, Finland

[2] Agenzia Spaziale Italiana Science Data Center, c/o ESRIN, via Galileo Galilei, Frascati, Italy

[3] Agenzia Spaziale Italiana, Viale Liegi 26, Roma, Italy

[4] Astronomy Department, University of Michigan, 830 Dennison Building, 500 Church Street, Ann Arbor, Michigan 48109-1042, USA

[5] Astroparticle Physics Laboratory, NASA/Goddard Space Flight Center, Greenbelt, MD 20771, USA

[6] Astroparticule et Cosmologie, CNRS (UMR7164), Université Denis Diderot Paris 7, Bâtiment Condorcet, 10 rue A. Domon et Léonie Duquet, Paris, France

[7] Astrophysics Group, Cavendish Laboratory, University of Cambridge, J J Thomson Avenue, Cambridge CB3 0HE, UK

[8] Atacama Large Millimeter/submillimeter Array, ALMA Santiago Central Offices, Alonso de Cordova 3107, Vitacura, Casilla 763 0355, Santiago, Chile

[9] Australia Telescope National Facility, CSIRO, PO Box 76, Epping, NSW 1710, Australia

[10] CITA, University of Toronto, 60 St. George St., Toronto, ON M5S 3H8, Canada

[11] CNRS, IRAP, 9 Av. colonel Roche, BP 44346, 31028 Toulouse Cedex 4, France

[12] California Institute of Technology, Pasadena, California, USA

[13] DAMTP, University of Cambridge, Centre for Mathematical Sciences, Wilberforce Road, Cambridge CB3 0WA, UK

[14] DSM/Irfu/SPP, CEA-Saclay, 91191 Gif-sur-Yvette Cedex, France

[15] DTU Space, National Space Institute, Juliane Mariesvej 30, Copenhagen, Denmark

[16] Departamento de Física, Universidad de Oviedo, Avda. Calvo Sotelo s/n, Oviedo, Spain

[17] Department of Astronomy and Astrophysics, Pennsylvania State University, 525 Davey Lab, University Park, PA 16802, USA

[18] Department of Astronomy and Astrophysics, University of Toronto, 50 Saint George Street, Toronto, Ontario, Canada

[19] Department of Physics & Astronomy, University of British Columbia, 6224 Agricultural Road, Vancouver, British Columbia, Canada

[20] Department of Physics, Gustaf Hällströmin katu 2a, University of Helsinki, Helsinki, Finland

[21] Department of Physics, Purdue University, 525 Northwestern Avenue, West Lafayette, Indiana, USA

[22] Department of Physics, University of California, Berkeley, California, USA

[23] Department of Physics, University of California, One Shields Avenue, Davis, California, USA

[24] Department of Physics, University of California, Santa Barbara, California, USA

[25] Department of Physics, University of Illinois at Urbana-Champaign, 1110 West Green Street, Urbana, Illinois, USA

[26] Dipartimento di Fisica G. Galilei, Università degli Studi di Padova, via Marzolo 8, 35131 Padova, Italy

[27] Dipartimento di Fisica M. Merlin dell'Università e del Politecnico di Bari, 70126 Bari, Italy

[28] Dipartimento di Fisica, Università degli Studi di Perugia, 06123 Perugia, Italy

[29] Dipartimento di Fisica, Università La Sapienza, P. le A. Moro 2, Roma, Italy

[30] Dipartimento di Fisica, Università degli Studi di Milano, via Celoria, 16, Milano, Italy

[31] Dipartimento di Fisica, Università degli Studi di Trieste, via A. Valerio 2, Trieste, Italy

[32] Dipartimento di Fisica, Università di Ferrara, via Saragat 1, 44122 Ferrara, Italy

[33] Dipartimento di Fisica, Università di Roma Tor Vergata, via della Ricerca Scientifica 1, Roma, Italy

[34] Discovery Center, Niels Bohr Institute, Blegdamsvej 17, Copenhagen, Denmark

[35] Dpto. Astrofísica, Universidad de La Laguna (ULL), 38206 La Laguna, Tenerife, Spain

[36] European Southern Observatory, ESO Vitacura, Alonso de Cordova 3107, Vitacura, Casilla 19001, Santiago, Chile

[37] European Space Agency, ESAC, Planck Science Office, Camino bajo del Castillo, s/n, Urbanización Villafranca del Castillo, Villanueva de la Cañada, Madrid, Spain

[38] European Space Agency, ESTEC, Keplerlaan 1, 2201 AZ Noordwijk, The Netherlands

[39] Finnish Centre for Astronomy with ESO (FINCA), University of Turku, Väisäläntie 20, 21500 Piikkiö, Finland

[40] Haverford College Astronomy Department, 370 Lancaster Avenue, Haverford, Pennsylvania, USA

[41] Helsinki Institute of Physics, Gustaf Hällströmin katu 2, University of Helsinki, Helsinki, Finland

[42] INAF – Osservatorio Astrofisico di Catania, via S. Sofia 78, Catania, Italy

[43] INAF – Osservatorio Astronomico di Padova, Vicolo dell'Osservatorio 5, Padova, Italy

[44] INAF – Osservatorio Astronomico di Roma, via di Frascati 33, Monte Porzio Catone, Italy

[45] INAF – Osservatorio Astronomico di Trieste, via G.B. Tiepolo 11, Trieste, Italy

[46] INAF/IASF Bologna, via Gobetti 101, Bologna, Italy

[47] INAF/IASF Milano, via E. Bassini 15, Milano, Italy

[48] INRIA, Laboratoire de Recherche en Informatique, Université Paris-Sud 11, Bâtiment 490, 91405 Orsay Cedex, France

[49] ISDC Data Centre for Astrophysics, University of Geneva, ch. d'Ecogia 16, Versoix, Switzerland

[50] Imperial College London, Astrophysics group, Blackett Laboratory, Prince Consort Road, London, SW7 2AZ, UK

[51] Infrared Processing and Analysis Center, California Institute of Technology, Pasadena, CA 91125, USA

[52] Institut Néel, CNRS, Université Joseph Fourier Grenoble I, 25 rue des Martyrs, Grenoble, France

[53] Institut d'Astrophysique Spatiale, CNRS (UMR8617) Université Paris-Sud 11, Bâtiment 121, Orsay, France

[54] Institut d'Astrophysique de Paris, CNRS UMR7095, Université Pierre & Marie Curie, 98 bis boulevard Arago, Paris, France

[55] Institut de Radioastronomie Millimétrique (IRAM), Avenida Divina Pastora 7, Local 20, 18012 Granada, Spain

[56] Institute of Astronomy and Astrophysics, Academia Sinica, Taipei, Taiwan

[57] Institute of Astronomy, University of Cambridge, Madingley Road, Cambridge CB3 0HA, UK

[58] Institute of Theoretical Astrophysics, University of Oslo, Blindern, Oslo, Norway

[59] Instituto de Astrofísica de Canarias, C/Vía Láctea s/n, La Laguna, Tenerife, Spain

[60] Instituto de Física de Cantabria (CSIC-Universidad de Cantabria), Avda. de los Castros s/n, Santander, Spain

[61] Istituto Nazionale di Fisica Nucleare, Sezione di Bari, 70126 Bari, Italy

[62] Istituto Nazionale di Fisica Nucleare, Sezione di Perugia, 06123 Perugia, Italy

[63] Istituto di Fisica del Plasma, CNR-ENEA-EURATOM Association, via R. Cozzi 53, Milano, Italy

[64] Jet Propulsion Laboratory, California Institute of Technology, 4800 Oak Grove Drive, Pasadena, California, USA

[65] Jodrell Bank Centre for Astrophysics, Alan Turing Building, School of Physics and Astronomy, The University of Manchester, Oxford Road, Manchester, M13 9PL, UK

[66] Kavli Institute for Cosmology Cambridge, Madingley Road, Cambridge, CB3 0HA, UK

[67] Key Laboratory of Optical Astronomy, National Astronomical Observatories, Chinese Academy of Sciences, 20A Datun Road, Chaoyang District, Beijing 100012, PR China

[68] LERMA, CNRS, Observatoire de Paris, 61 Avenue de l'Observatoire, Paris, France

[69] Laboratoire AIM, IRFU/Service d'Astrophysique – CEA/DSM – CNRS – Université Paris Diderot, Bât. 709, CEA-Saclay, 91191 Gif-sur-Yvette Cedex, France

[70] Laboratoire Traitement et Communication de l'Information, CNRS (UMR 5141) and Télécom ParisTech, 46 rue Barrault, 75634 Paris Cedex 13, France

[71] Laboratoire de Physique Subatomique et de Cosmologie, CNRS/IN2P3, Université Joseph Fourier Grenoble I, Institut National Polytechnique de Grenoble, 53 rue des Martyrs, 38026 Grenoble Cedex, France

[72] Laboratoire de l'Accélérateur Linéaire, Université Paris-Sud 11, CNRS/IN2P3, Orsay, France

[73] Lawrence Berkeley National Laboratory, Berkeley, California, USA

[74] Max-Planck-Institut für Astrophysik, Karl-Schwarzschild-Str. 1, 85741 Garching, Germany

[75] Max-Planck-Institut für Radioastronomie, Auf dem Hügel 69, 53121 Bonn, Germany

[76] MilliLab, VTT Technical Research Centre of Finland, Tietotie 3, Espoo, Finland

[77] National University of Ireland, Department of Experimental Physics, Maynooth, Co. Kildare, Ireland

[78] Niels Bohr Institute, Blegdamsvej 17, Copenhagen, Denmark

[79] Owens Valley Radio Observatory, Mail code 249-17, California Institute of Technology, 1200 E California Blvd, Pasadena, CA 91125, USA

[80] SISSA, Astrophysics Sector, via Bonomea 265, 34136 Trieste, Italy

[81] SUPA, Institute for Astronomy, University of Edinburgh, Royal Observatory, Blackford Hill, Edinburgh EH9 3HJ, UK

[82] School of Physics and Astronomy, Cardiff University, Queens Buildings, The Parade, Cardiff, CF24 3AA, UK

[83] Space Sciences Laboratory, University of California, Berkeley, California, USA

[84] Special Astrophysical Observatory, Russian Academy of Sciences, Nizhnij Arkhyz, Zelenchukskiy region, Karachai-Cherkessian Republic 369167, Russia

[85] Stanford University, Dept of Physics, Varian Physics Bldg, 382 via Pueblo Mall, Stanford, California, USA

[86] Tuorla Observatory, Department of Physics and Astronomy, University of Turku, Väisäläntie 20, 21500, Piikkiö, Finland

[87] Université de Toulouse, UPS-OMP, IRAP, 31028 Toulouse Cedex 4, France

[88] Universities Space Research Association, Stratospheric Observatory for Infrared Astronomy, MS 211-3, Moffett Field, CA 94035, USA

[89] University of Granada, Departamento de Física Teórica y del Cosmos, Facultad de Ciencias, Granada, Spain

[90] University of Miami, Knight Physics Building, 1320 Campo Sano Dr., Coral Gables, Florida, USA

[91] W. W. Hansen Experimental Physics Laboratory, Kavli Institute for Particle Astrophysics and Cosmology, Department of Physics and SLAC National Accelerator Laboratory, Stanford University, Stanford, CA 94305, USA

[92] Warsaw University Observatory, Aleje Ujazdowskie 4, 00-478 Warszawa, Poland

Pages 17 to 56 are available in the electronic edition of the journal at `http://www.aanda.org`

Table 1. The complete 1 Jy northern sample of AGN. Column 8 refers to the 37 GHz observations of Metsähovi Radio Observatory.

(1) Name	(2) J2000 Name	(3) Alias	(4) RA(J2000)	(5) Dec(J2000)	(6) 1st scan	(7) 2nd scan	(8) S_{ave} [Jy]	(9) $\log \nu_s$	(10) Syn quality	(11) $\log \nu_{IC}$	(12) IC quality
0003−066	0006−0623	NRAO5	00:06:13.90	−06:23:36.00	2009-12-12	...	2.06	13.1	A	...	...
0007+106	0010+1058	IIIZW2	00:10:31.01	10:58:29.50	2009-12-25	...	1.04	...	...	...	...
0048−097	0050−0929	PKS 0048−097	00:50:41.20	−09:29:06.00	2009-12-23	...	1.34	14.1	A	...	...
0059+581	0102+5824	TXS 0059+581	01:02:45.76	58:24:11.14	2010-01-28	...	2.97	13.6	B	...	...
0106+013	0108+0135	OC012	01:08:38.77	01:35:00.30	2010-01-04	...	1.85	12.7	B	...	...
J0125−0005	0125−0005		01:25:28.84	−00:05:56.00	2010-01-08	...	1.24	13.6	B	...	...
0133+476	0136+4751	DA55	01:36:58.59	47:51:29.10	2010-01-29	...	3.02	12.8	A	...	...
0149+218	0152+2207		01:52:18.06	22:07:07.70	2010-01-24	...	1.06	...	...	...	...
0202+149	0204+1514	4C 15.05	02:04:50.41	15:14:11.00	2010-01-24	...	1.64	...	...	...	...
0212+735	0217+7349		02:17:30.81	73:49:32.60	2009-09-13	2010-02-11	2.05	12.4	B	...	...
0224+671	0228+6721		02:28:50.05	67:21:03.00	2009-09-13	2010-02-10	1.28	...	...	...	...
0234+285	0237+2848	4C 28.07	02:37:52.41	28:48:09.00	2010-02-03	...	2.86	13.1	A	22.1	B
0235+164	0238+1636		02:38:38.80	16:36:59.00	2010-02-01	...	2.33	13.1	A	...	...
0238−084	0241−0815		02:41:04.80	−08:15:20.75	2010-01-24	...	1.33	...	...	...	...
0306+102	0309+1029	PKS 0306+102	03:09:03.60	10:29:16.00	2010-02-06	...	1.01	12.9	B	...	...
0316+413	0319+4130	3C 84	03:19:48.16	41:30:42.10	2010-02-13	...	14.01	...	...	22.9	B
0333+321	0336+3218	NRAO140	03:36:30.11	32:18:29.30	2010-02-15	...	1.49	...	...	...	...
0336−019	0339−0146	CTA026	03:39:30.94	−01:46:36.00	2010-02-10	...	2.21	13.1	B	...	...
0355+508	0359+5057	NRAO150	03:59:29.75	50:57:50.20	2009-09-13	2010-02-19	5.92	...	...	...	...
0415+379	0418+3801	3C 111	04:18:21.28	38:01:35.80	2010-02-22	...	5.97	...	...	...	...
0420−014	0423−0120	OA129	04:23:15.80	−01:20:33.10	2010-02-21	...	7.27	13.2	B	...	...
0430+052	0433+0521	3C 120	04:33:11.10	05:21:15.60	2010-02-24	...	2.65	...	...	...	...
0446+112	0449+1121	PKS 0446+112	04:49:07.67	11:21:28.00	2010-02-27	...	1.41	...	...	...	...
0458−020	0501−0159	PKS 0458−020	05:01:12.81	−01:59:14.00	2010-03-01	...	1.86	...	...	...	...
0507+179	0510+1800		05:10:02.37	18:00:41.58	2009-09-13	2010-03-03	1.14	...	...	...	...
0528+134	0530+1331	PKS 0528+134	05:30:56.42	13:31:55.15	2009-09-14	2010-03-07	4.55	...	...	21.8	B
0552+398	0555+3948	DA193	05:55:30.81	39:48:49.17	2009-09-22	2010-03-09	3.18	...	...	21.4	B
0605−085	0607−0834	PKS 0605−085	06:07:59.70	−08:34:50.00	2009-09-19	2010-03-17	1.73	13.2	B	...	...
0642+449	0646+4451	OH471	06:46:32.03	44:51:16.59	2009-09-30	2010-03-16	2.36	12.5	B	22.7	B
0716+714	0721+7120		07:21:53.30	71:20:36.00	2009-10-04	2010-03-10	2.12	14.3	A	23.4	B
0723−008	0725−0054	PKS 0723−008	07:25:50.70	−00:54:56.00	2009-10-09	2010-04-02	1.05	13.0	A	...	...
0735+178	0738+1742	PKS 0735+17	07:38:07.40	17:42:19.00	2009-10-10	2010-03-31	1.93	...	...	...	...
0736+017	0739+0137		07:39:18.03	01:37:04.60	2009-10-12	2010-04-04	1.85	14.0	B	...	...
0748+126	0750+1231		07:50:52.05	12:31:04.83	2009-10-14	2010-04-04	2.42	12.7	A	21.5	A
0754+100	0757+0956	OI090.4	07:57:06.64	09:56:34.90	2009-10-15	2010-04-06	1.33	13.0	B	...	...
0805−077	0808−0751		08:08:15.54	−07:51:09.89	2009-10-22	2010-04-12	1.05	12.7	B	...	...
0804+499	0808+4950		08:08:39.67	49:50:36.50	2009-10-12	2010-03-27	1.30	13.3	B	...	...
0823+033	0825+0309	PKS 0823+033	08:25:50.30	03:09:24.00	2009-10-24	2010-04-14	1.48	13.7	B	...	...
0827+243	0830+2411	OJ248	08:30:52.08	24:10:60.00	2009-10-21	2010-04-09	1.48	...	...	...	...
0836+710	0841+7053	4C 71.07	08:41:24.37	70:53:42.20	2009-10-12	2010-03-17	1.80	12.9	B	20.5	B
0851+202	0854+2006	OJ287	08:54:48.80	20:06:30.00	2009-10-27	2010-04-15	3.90	13.1	B	21.8	B
0906+430	0909+4253	3C 216	09:09:33.50	42:53:46.08	2009-10-23	2010-04-09	1.02	13.2	B	...	...
0917+449	0920+4441		09:20:58.46	44:41:53.99	2009-10-25	2010-04-11	1.27	12.7	A	21.7	A

Table 1. continued.

(1) Name	(2) J2000 Name	(3) Alias	(4) RA(J2000)	(5) Dec(J2000)	(6) 1st scan	(7) 2nd scan	(8) S_{ave} [Jy]	(9) log ν_s	(10) Syn quality	(11) log ν_{IC}	(12) IC quality
0923+392	0927+3902	4C 39.25	09:27:03.01	39:02:20.90	2009-10-28	2010-04-15	7.06	...	...	22.7	B
0945+408	0948+4039	4C 40.24	09:48:55.34	40:39:44.60	2009-10-31	2010-04-18	1.32	13.1	B	...	...
0953+254	0956+2515		09:56:49.88	25:15:16.05	2009-11-08	2010-04-27	1.13	13.1	B	...	B
0954+658	0958+6533	S40954+65	09:58:47.20	65:33:54.00	2009-10-21	2010-03-30	1.03	12.8	B	21.7	B
1036+054	1038+0512		10:38:46.78	05:12:29.09	2009-11-29	2010-05-16	1.13	...	...	...	...
TEX1040+244	1043+2408		10:43:09.00	24:08:35.00	2009-11-19	2010-05-10	1.02	...	...	...	...
1055+018	1058+0133	OL093	10:58:29.61	01:33:58.80	2009-12-07	2010-05-24	3.96	12.7	B	22.5	A
J1130+3815	1130+3815	QSO B1128+385?	11:30:53.28	38:15:18.50	2009-11-21	2010-05-15	1.16	12.9	B	...	...
1150+812	1153+8058		11:53:12.50	80:58:29.15	2009-10-16	2010-03-07	1.11	...	...	...	...
1150+497	1153+4931		11:53:24.47	49:31:08.83	2009-11-16	2010-05-11	1.40	...	...	...	...
1156+295	1159+2914	4C 29.45	11:59:31.83	29:14:44.00	2009-12-04	2010-05-31	2.00	13.4	A	23.5	B
1219+044	1222+0413		12:22:22.55	04:13:15.78	2009-12-29	...	1.39	...	...	...	...
1222+216	1224+2122	PKS 1222+216	12:24:54.51	21:22:47.00	2009-12-18	...	1.16	14.2	B	22.7	B
1226+023	1229+0203	3C 273	12:29:06.69	02:03:08.60	2010-01-02	...	24.37	14.1	B	20.8	A
1228+126	1230+1223	3C 274	12:30:49.42	12:23:28.00	2009-12-26	...	14.04	13.4	B	...	...
1253−055	1256−0547	3C 279	12:56:11.17	−05:47:21.50	2010-01-13	...	17.20	12.8	B	22.7	B
1308+326	1310+3220	AUCVn	13:10:28.66	32:20:43.80	2009-12-21	...	2.26	12.6	B	...	...
1324+224	1327+2210		13:27:00.86	22:10:50.16	2010-01-05	...	1.15	12.8	B	...	...
1413+135	1415+1320		14:15:58.80	13:20:24.00	2010-01-25	...	1.51	...	...	...	...
1418+546	1419+5423	OQ530	14:19:46.60	54:23:14.00	2009-12-06	...	1.16	...	...	20.6	B
1502+106	1504+1029	OR103	15:04:24.98	10:29:39.00	2010-02-08	...	1.30	...	...	...	...
1510−089	1512−0905	PKS 1510−089	15:12:50.53	−09:05:59.00	2010-02-14	...	2.48	13.4	B	...	...
1546+027	1549+0237		15:49:29.44	02:37:01.20	2010-02-21	...	2.42	13.8	B	...	...
1548+056	1550+0527		15:50:35.27	05:27:10.45	2010-02-21	...	2.04	...	...	...	...
1606+106	1608+1029	4C 10.45	16:08:46.20	10:29:07.80	2010-02-24	...	1.65	...	...	...	...
1611+343	1613+3412	DA406	16:13:41.00	34:12:48.00	2010-02-23	...	3.03	13.5	B	21.6	B
1633+382	1635+3808	4C 38.41	16:35:15.49	38:08:04.50	2010-03-02	...	2.90	...	...	...	...
1638+398	1640+3946		16:40:29.63	39:46:46.03	2010-03-04	...	1.18	...	...	...	...
1642+690	1642+6856		16:42:07.85	68:56:39.76	2009-11-06	2010-01-17	1.74	12.2	A	...	...
1641+399	1642+3948	3C 345	16:42:58.81	39:48:37.00	2010-03-05	...	7.89	...	...	...	...
1652+398	1653+3945	MARK501	16:53:52.20	39:45:36.00	2010-03-09	...	1.00	...	A	...	...
1739+522	1740+5211	S41739+52	17:40:36.98	52:11:43.00	2010-03-30	...	1.45	...	...	...	...
1741−038	1743−0350	PKS 1741−038	17:43:58.86	−03:50:04.60	2009-09-13	2010-03-18	4.39	13.0	A	23.2	A
1749+096	1751+0939	PKS 1749+096	17:51:32.70	09:39:01.00	2009-09-13	2010-03-21	4.50	13.5	A	23.1	A
1803+784	1800+7828	S51803+784	18:00:45.40	78:28:04.00	2009-10-11	2010-02-02	1.90	14.3	A	23.1	B
1807+698	1806+6949	3C 371.0	18:06:50.70	69:49:28.00	2009-10-21	2010-01-07	1.37	13.0	B	...	...
1823+568	1824+5651	4C 56.27	18:24:07.07	56:51:01.50	2010-04-17	...	1.60	14.0	B	...	...
1828+487	1829+4844	3C 380	18:29:31.80	48:44:46.62	2010-04-11	...	2.38	12.6	A	...	...
J184915+67064	1849+6705		18:49:15.89	67:06:40.90	2009-10-12	2009-12-25	1.82	...	...	...	...
1928+738	1927+7358	4C 73.18	19:27:48.50	73:58:01.60	2009-09-28	2010-01-18	2.61	13.7	B	21.0	B
1954+513	1955+5131		19:55:42.74	51:31:48.55	2009-10-09	2010-05-06	1.35	13.1	B	...	...
2007+776	2005+7752	S52007+77	20:05:31.10	77:52:43.00	2009-09-25	2010-01-27	1.40	...	B	...	...
2005+403	2007+4029		20:07:44.94	40:29:48.60	2009-10-17	2010-05-02	2.04	...	...	...	...

Table 1. continued.

(1) Name	(2) J2000 Name	(3) Alias	(4) RA(J2000)	(5) Dec(J2000)	(6) 1st scan	(7) 2nd scan	(8) S_{ave} [Jy]	(9) $\log \nu_s$	(10) Syn quality	(11) $\log \nu_{IC}$	(12) IC quality
2021+614	2022+6136	OW637	20:22:06.68	61:36:58.80	2009-12-20	2010-05-26	1.25	...	...	...	...
2037+511	2038+5119		20:38:37.04	51:19:12.66	2009-11-25	2010-05-18	2.46	13.2	B	...	...
2121+053	2123+0535		21:23:44.52	05:35:22.09	2009-11-02	2010-05-08	1.74	...	...	...	...
2131−021	2134−0153	PKS 2131−021	21:34:10.31	−01:53:17.24	2009-11-02	2010-05-09	1.46	...	...	...	...
2134+004	2136+0041	OX057	21:36:38.59	00:41:54.21	2009-11-04	2010-05-10	3.34	12.5	...	21.0	A
2136+141	2139+1423		21:39:01.31	14:23:36.00	2009-11-11	2010-05-16	1.29	...	...	...	...
2145+067	2148+0657		21:48:05.46	06:57:38.60	2009-11-10	2010-05-16	7.37	...	...	...	...
2200+420	2202+4216	BLLAC	22:02:43.30	42:16:39.00	2009-12-13	2010-06-06	3.35	13.8	B	22.6	A
2201+315	2203+3145	4C 31.63	22:03:14.98	31:45:38.30	2009-12-02	2010-05-30	2.53	14.2	B	20.7	B
2201+171	2203+1725		22:03:26.89	17:25:48.20	2009-11-21	2010-05-24	1.21	13.5	B	...	...
2216−038	2218−0335		22:18:52.04	−03:35:36.90	2009-11-14	2010-05-21	1.41	14.0	B	...	...
2223−052	2225−0457	3C 446	22:25:47.26	−04:57:01.40	2009-11-15	2010-05-23	5.58	12.7	B	22.0	A
2227−088	2229−0832		22:29:40.09	−08:32:54.50	2009-11-14	2010-05-23	1.94	...	...	20.7	B
2230+114	2232+1143	CTA102	22:32:36.41	11:43:50.90	2009-11-27	2010-05-31	3.84	13.2	B	22.6	B
2234+282	2236+2828		22:36:22.47	28:28:57.41	2009-12-10	...	1.03	13.0	B	...	...
2251+158	2253+1608	3C 454.3	22:53:57.75	16:08:53.60	2009-12-06	...	9.42	13.9	B	22.6	A
4C 45.51	2354+4553		23:54:21.68	45:53:04.00	2010-01-11	...	1.12	...	...	...	...
2353+816	2356+8152		23:56:22.79	81:52:52.26	2009-09-19	2010-02-08	1.59	...	...	...	...

Table 4. Simultaneity of high energy data to *Planck* observations displayed in the SEDs.

B1950 Name	J2000 Name	UVOT	*Swift*-XRT	*Fermi*
0003−066	0006−0623	sim_1st	sim_1st	sim_1st
0007+106	0010+1058	...	...	27m
0048−097	0050−0929	sim_1st	sim_1st	sim_1st
0059+581	0102+5824	...	...	sim_1st
0106+013	0108+0135	...	...	sim_1st
J0125−0005	0125−0005	...	...	sim_1st
0133+476	0136+4751	sim_1st	sim_1st	sim_1st
0149+218	0152+2207	...	...	sim_1st
0202+149	0204+1514	...	...	sim_1st
0212+735	0217+7349	...	...	27m
0224+671	0228+6721	...	...	sim_1st
0234+285	0237+2848	sim_1st	sim_1st	sim_1st
0235+164	0238+1636	sim_1st	sim_1st	sim_1st
0238−084	0241−0815	...	...	sim_1st
0306+102	0309+1029	...	...	27m
0316+413	0319+4130	...	...	27m
0333+321	0336+3218	...	...	27m
0336−019	0339−0146	...	...	sim_1st
0355+508	0359+5057	...	...	sim_1st
0415+379	0418+3801	...	...	sim_1st
0420−014	0423−0120	sim_1st	sim_1st	sim_1st
0430+052	0433+0521	sim_1st	sim_1st	sim_1st
0446+112	0449+1121	...	...	27m
0458−020	0501−0159	...	...	27m
0507+179	0510+1800	...	...	sim_1st
0528+134	0530+1331	sim_2nd	sim_1st_2nd	sim_1st
0552+398	0555+3948	sim_1st	sim_1st	sim_1st
0605−085	0607−0834	...	...	sim_1st
0642+449	0646+4451	sim_1st	sim_1st	sim_1st
0716+714	0721+7120	sim_1st_2nd	sim_1st_2nd	sim_1st_2nd
0723−008	0725−0054	...	...	...
0735+178	0738+1742	...	...	27m
0736+017	0739+0137	sim_1st	sim_1st	sim_1st
0748+126	0750+1231	sim_2nd	sim_2nd	2M_2nd
0754+100	0757+0956	...	...	2M_1st
0805−077	0808−0751	...	...	sim_1st
0804+499	0808+4950	sim_1st	sim_1st	2M_1st
0823+033	0825+0309	...	...	27m
0827+243	0830+2411	...	...	2M_1st
0836+710	0841+7053	sim_2nd	sim_2nd	2M_2nd
0851+202	0854+2006	sim_2nd	sim_2nd	2M_1st_2nd
0906+430	0909+4253	...	...	...
0917+449	0920+4441	sim_1st	sim_1st	2M_1st
0923+392	0927+3902	sim_2nd	sim_2nd	sim_2nd
0945+408	0948+4039	...	...	2M_1st
0953+254	0956+2515	...	...	2M_1st
0954+658	0958+6533	sim_1st	sim_1st	2M_1st
1036+054	1038+0512	...	...	2M_1st
TEX1040+244	1043+2408	...	...	2M_1st
1055+018	1058+0133	sim_1st	sim_1st	2M_1st
J1130+3815	1130+3815	...	...	2M_1st
1150+812	1153+8058	...	...	sim_1st
1150+497	1153+4931	sim_1st	sim_1st	2M_1st
1156+295	1159+2914	sim_1st_2nd	sim_1st_2nd	sim_1st_2nd
1219+044	1222+0413	...	...	27m
1222+216	1224+2122	sim_1st	sim_1st	sim_1st
1226+023	1229+0203	sim_1st	sim_1st	sim_1st
1228+126	1230+1223	sim_1st	sim_1st	sim_1st
1253−055	1256−0547	sim_1st	sim_1st	sim_1st
1308+326	1310+3220	sim_1st	sim_1st	sim_1st
1324+224	1327+2210	...	...	sim_1st
1413+135	1415+1320	...	...	sim_1st
1418+546	1419+5423	...	sim_1st	27m
1502+106	1504+1029	...	...	27m
1510−089	1512−0905	sim_1st	...	sim_1st
1546+027	1549+0237	sim_1st	sim_1st	sim_1st

Table 4. continued.

B1950 Name	J2000 Name	UVOT	*Swift*-XRT	*Fermi*
1548+056	1550+0527	...	...	sim_1st
1606+106	1608+1029	...	...	sim_1st
1611+343	1613+3412	sim_1st	sim_1st	sim_1st
1633+382	1635+3808	...	sim_1st	sim_1st
1638+398	1640+3946	...	...	27m
1642+690	1642+6856	...	...	2M_1st
1641+399	1642+3948	sim_1st	sim_1st	sim_1st
1652+398	1653+3945	...	...	27m
1739+522	1740+5211	...	...	27m
1741−038	1743−0350	...	...	sim_1st
1749+096	1751+0939	sim_2nd	sim_2nd	sim_2nd
1803+784	1800+7828	sim_1st	sim_1st	sim_1st
1807+698	1806+6949	sim_1st	sim_1st	2M_1st
1823+568	1824+5651	...	...	27m
1828+487	1829+4844	...	...	27m
J184915+670	1849+6705	sim_2nd	sim_2nd	...
1928+738	1927+7358	sim_1st	sim_1st	2M_1st
1954+513	1955+5131	...	...	...
2007+776	2005+7752	...	...	27m
2005+403	2007+4029	...	...	2M_1st
2021+614	2022+6136	...	...	2M_1st
2037+511	2038+5119	...	...	2M_1st
2121+053	2123+0535	...	...	2M_1st
2131−021	2134−0153	...	...	2M_1st
2134+004	2136+0041	sim_2nd	sim_2nd	2M_2nd
2136+141	2139+1423	...	...	2M_1st
2145+067	2148+0657	sim_1st	sim_1st	sim_1st
2200+420	2202+4216	sim_1st_2nd	sim_1st_2nd	sim_1st_2nd
2201+315	2203+3145	sim_1st	sim_1st	sim_1st
2201+171	2203+1725	...	...	2M_1st
2216−038	2218−0335	...	...	sim_1st
2223−052	2225−0457	sim_2nd	sim_2nd	2M_2nd
2227−088	2229−0832	...	sim_1st	2M_1st
2230+114	2232+1143	sim_1st	sim_1st	sim_1st
2234+282	2236+2828	...	...	sim_1st
2251+158	2253+1608	sim_1st	sim_1st	sim_1st
4C 45.51	2354+4553	...	...	sim_1st
2353+816	2356+8152	...	...	27m
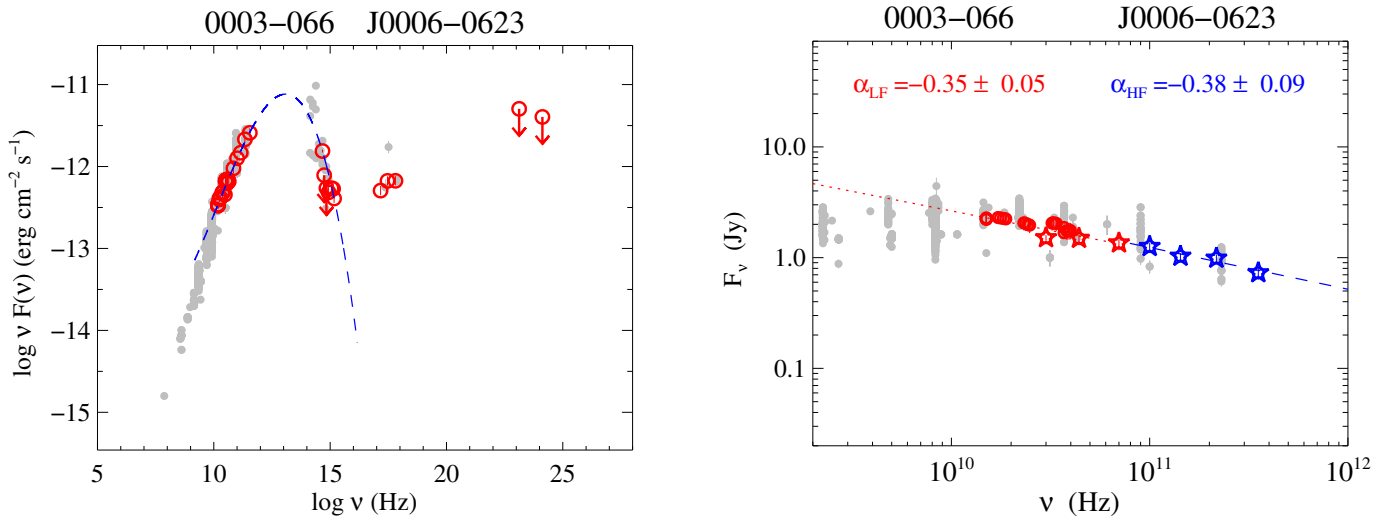
Fig. 18. *Left-panel*: the SED of the source 0003−066. Grey circles show the historical data. The red circles show data simultaneous to the *Planck* observations. The dotted and dashed lines show the second and third degree polynomials, respectively, fitted to the synchrotron and IC bumps in the SED. *Right-panel*: the radio spectrum of 0003−066. Red circles, LF data simultaneous to *Planck*; red stars, ERCSC LFI data; blue circles, HF data simultaneous to *Planck*; blue stars, ERCSC HFI data. The dashed and dotted lines are fits to simultaneous LF and HF data.

0007+106   J0010+1058

Fig. 19. 0007−106.

0048−097   J0050−0929

Fig. 20. 0048−097.

0059+581   J0102+5824
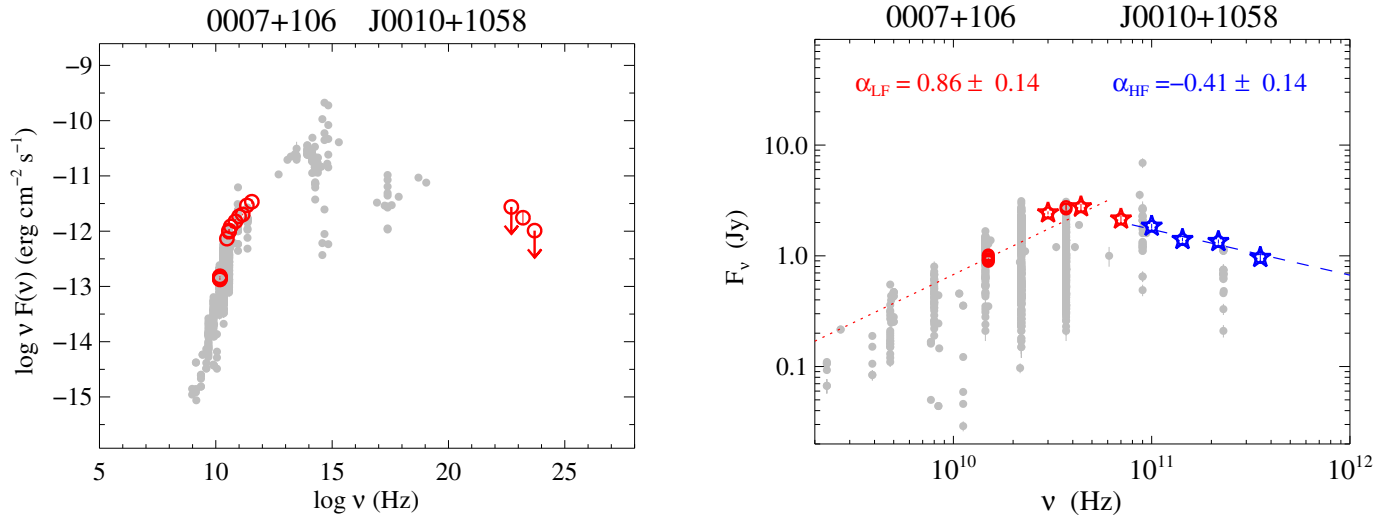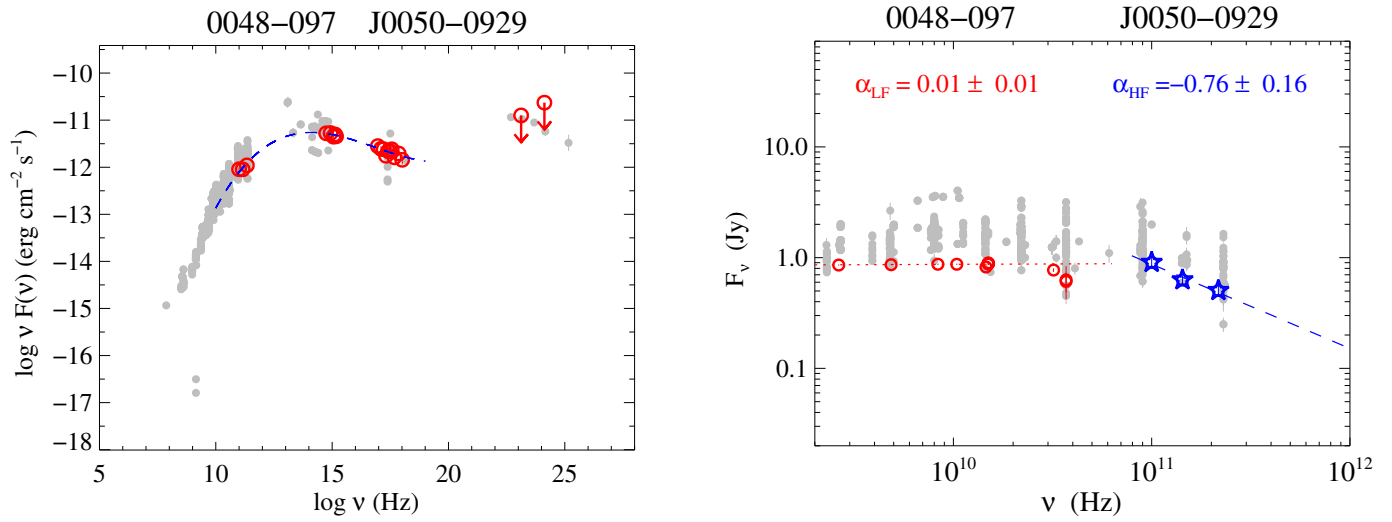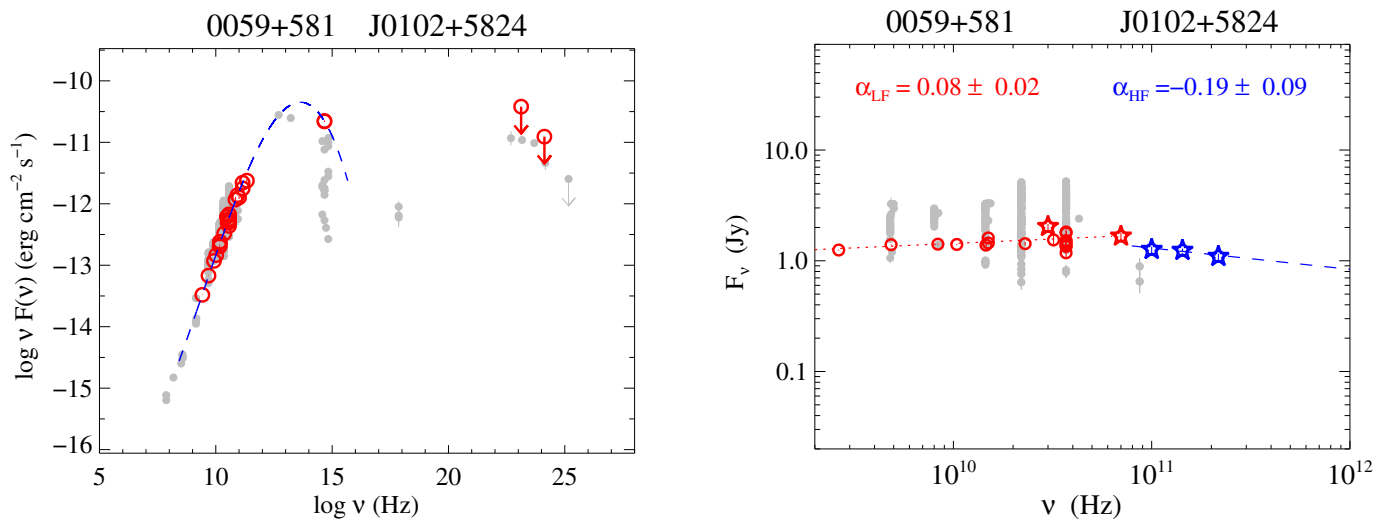
Fig. 21. 0059+581.
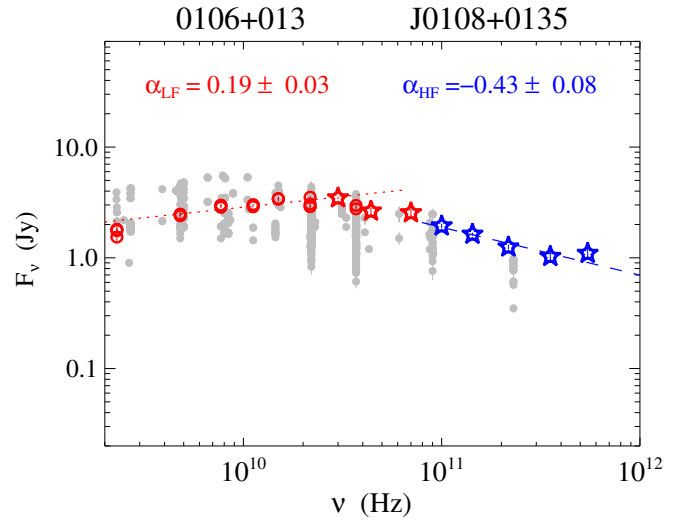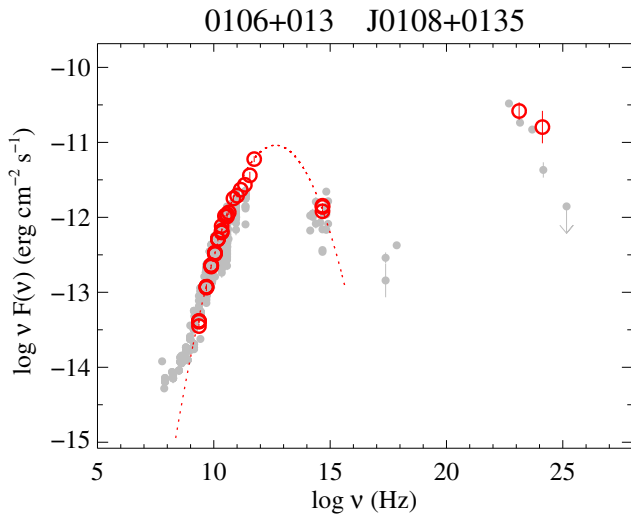
Fig. 22. 0106+013.
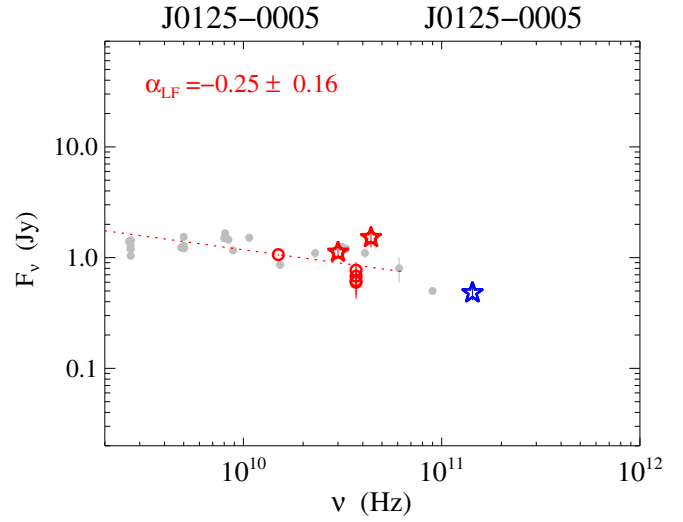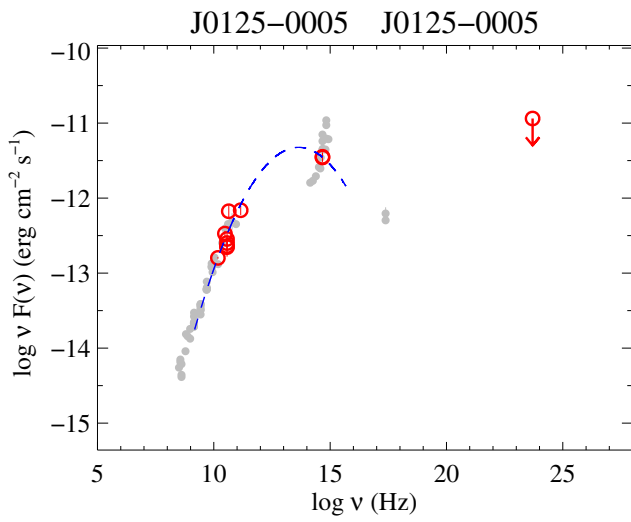
Fig. 23. J0125−0005.

Fig. 24. 0133+476.

0149+218   J0152+2207

0149+218   J0152+2207

Fig. 25. 0149+218.

0202+149   J0204+1514

0202+149   J0204+1514

Fig. 26. 0202+149.

0212+735   J0217+7349
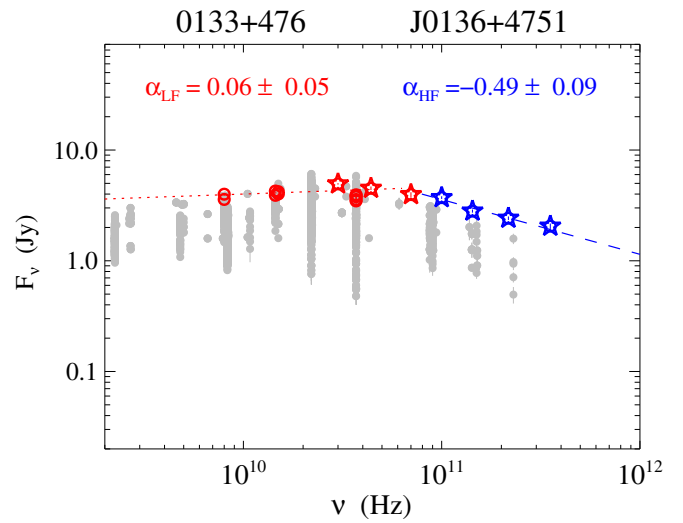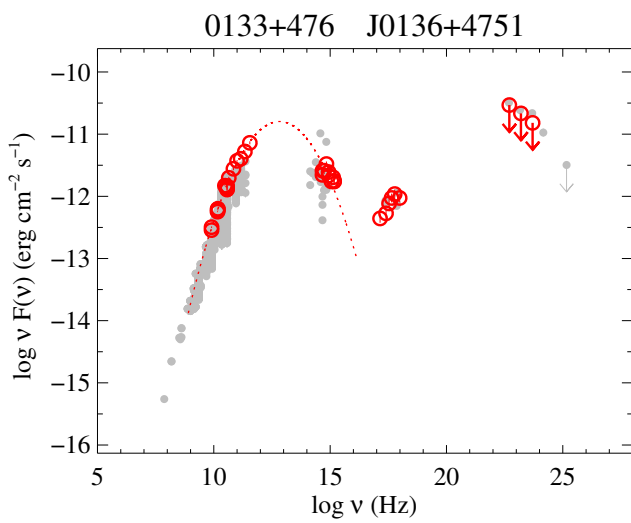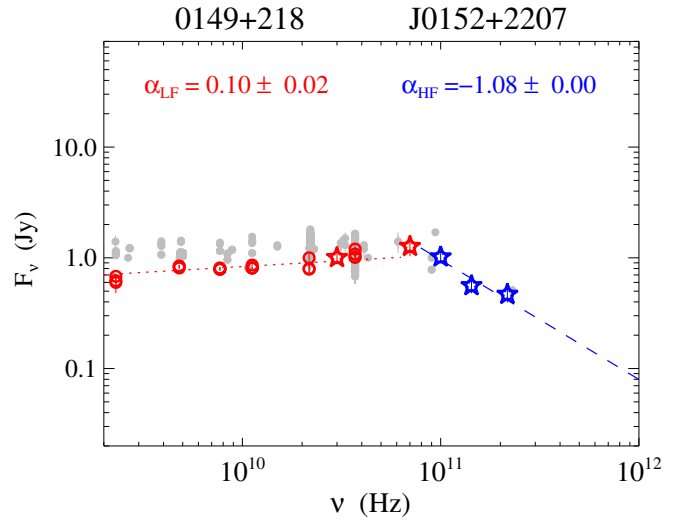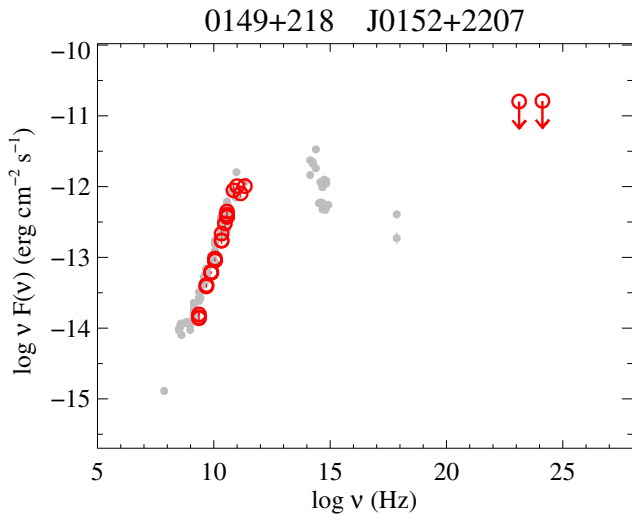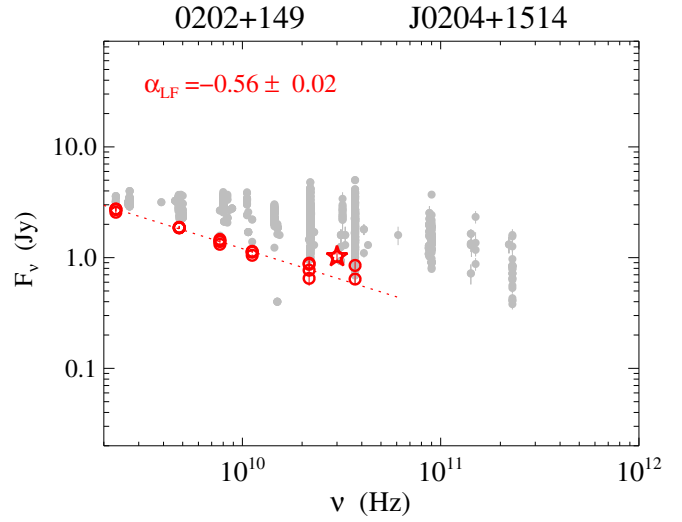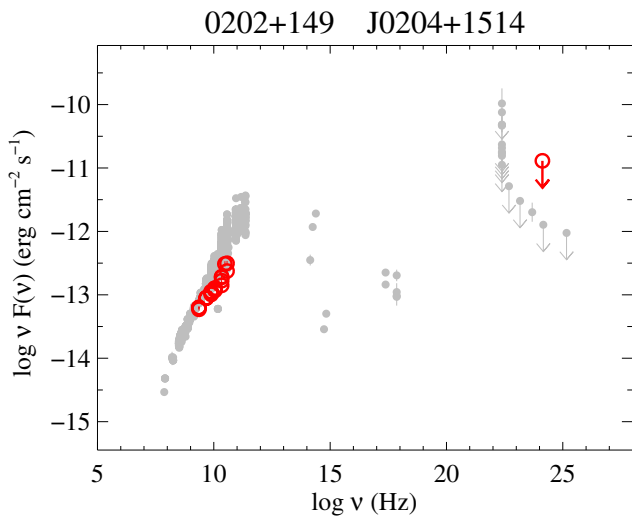
0212+735   J0217+7349
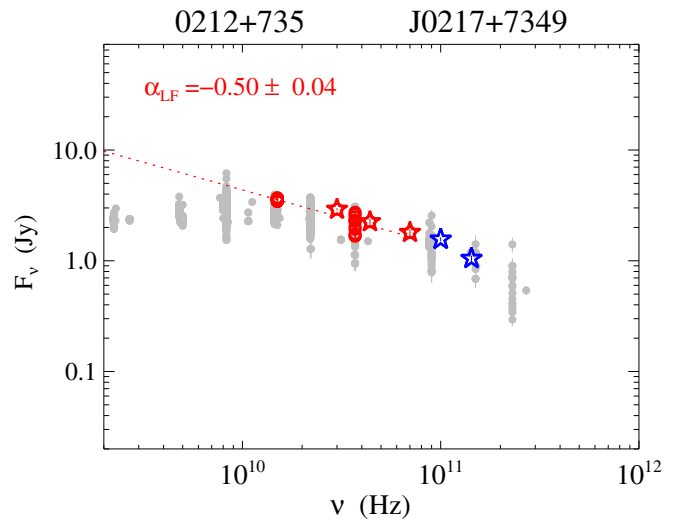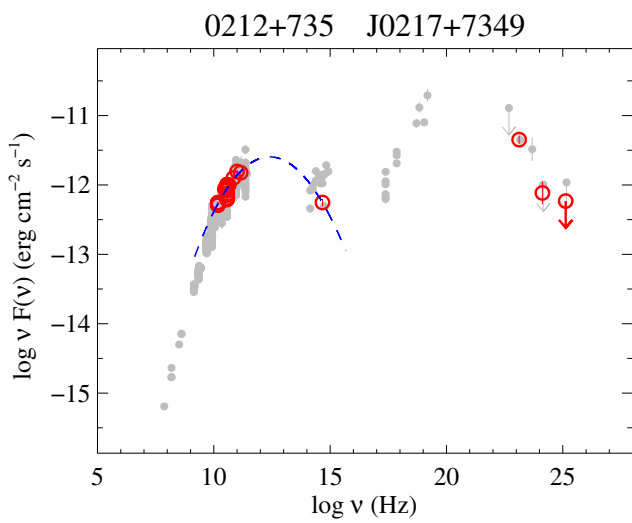
Fig. 27. 0212+735.
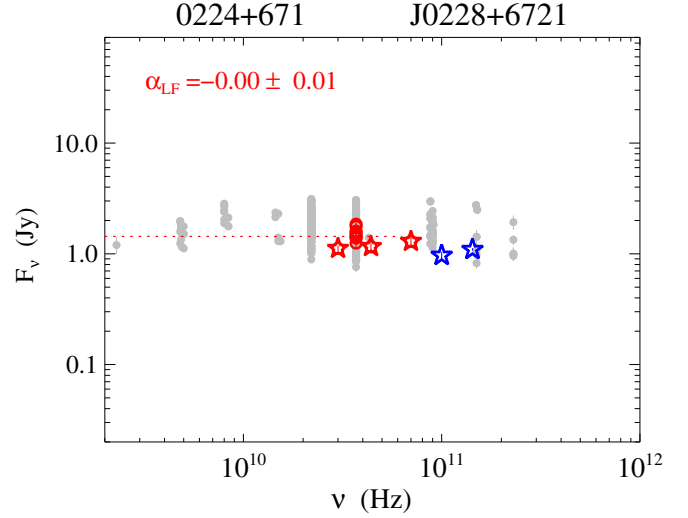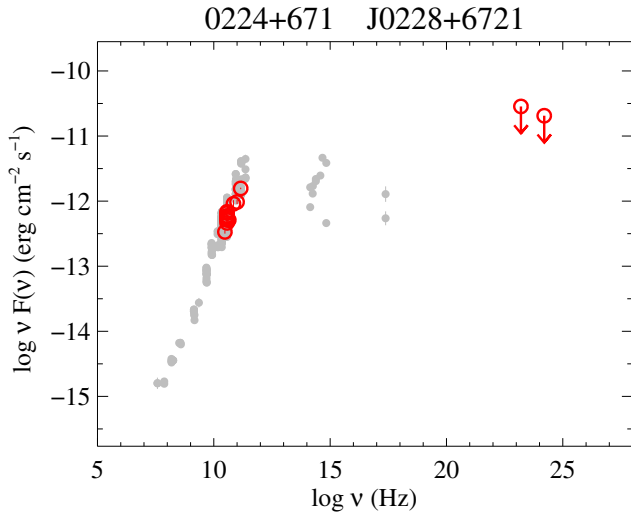
Fig. 28. 0224+671.
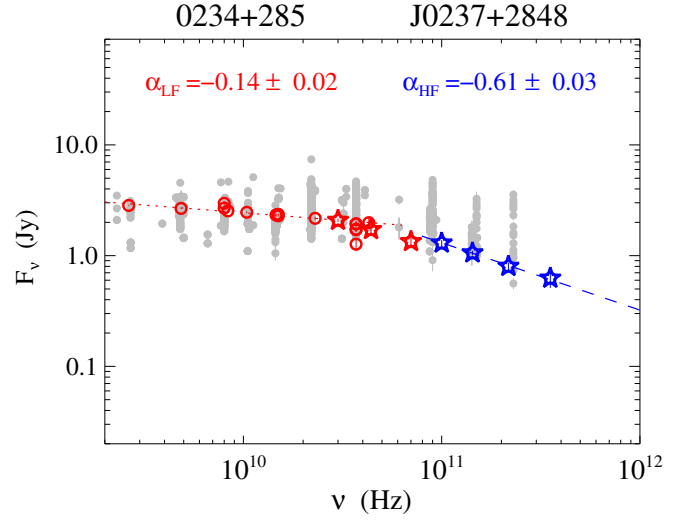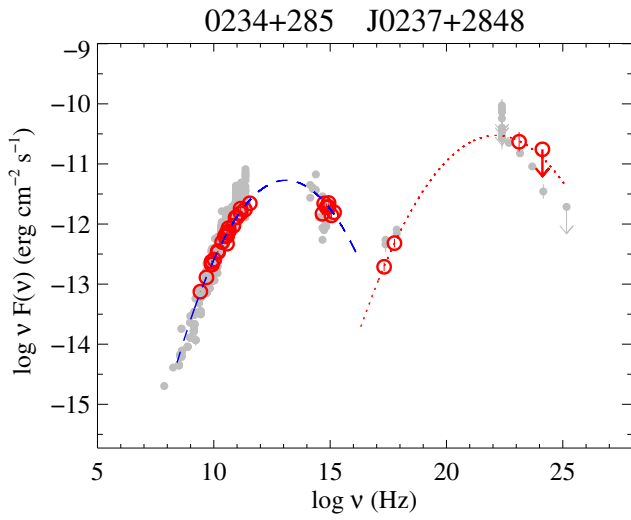
Fig. 29. 0234+285.
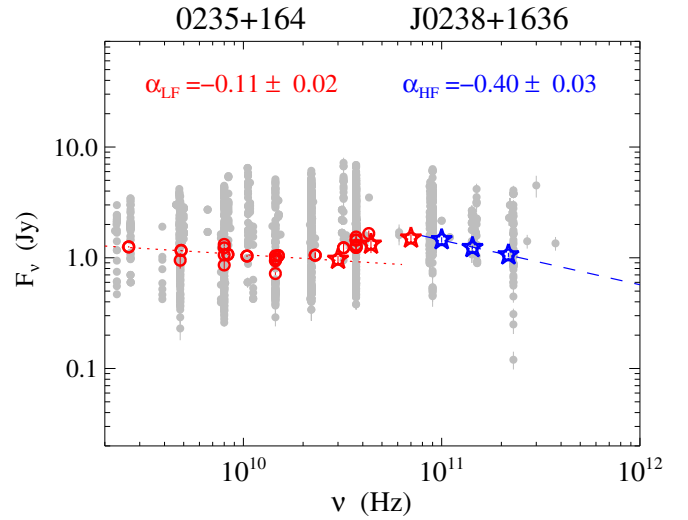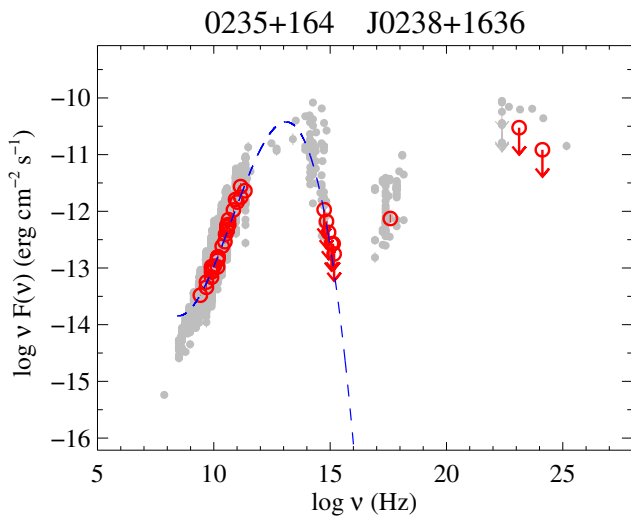
Fig. 30. 0235+164.

0238−084   J0241−0815

0238−084   J0241−0815

$\alpha_{LF} = -0.15 \pm 0.02$

Fig. 31. 0238−084.

0306+102   J0309+1029

0306+102   J0309+1029

$\alpha_{LF} = 0.00 \pm 0.00$ $\alpha_{HF} = -0.56 \pm 0.06$

Fig. 32. 0306+102.

0316+413   J0319+4130

0316+413   J0319+4130

$\alpha_{LF} = 0.01 \pm 0.02$ $\alpha_{HF} = -0.67 \pm 0.01$

Fig. 33. 0316+413.

0333+321   J0336+3218

0333+321   J0336+3218

$\alpha_{LF} = 0.26 \pm 0.06$

Fig. 34. 0333+321.

0336−019   J0339−0146

0336−019   J0339−0146

$\alpha_{LF} = -0.24 \pm 0.01$ $\alpha_{HF} = -1.10 \pm 0.00$

Fig. 35. 0336−019.

0355+508   J0359+5057

0355+508   J0359+5057

$\alpha_{LF} = 0.21 \pm 0.04$ $\alpha_{HF} = -0.75 \pm 0.02$

Fig. 36. 0355+508.

0415+379   J0418+3801

Fig. 37. 0415+379.

0415+379   J0418+3801

$\alpha_{LF} = -0.58 \pm 0.04$ $\alpha_{HF} = -0.37 \pm 0.26$

0420−014   J0423−0120

Fig. 38. 0420−014.

0420−014   J0423−0120

$\alpha_{LF} = 0.33 \pm 0.03$ $\alpha_{HF} = -0.60 \pm 0.02$

0430+052   J0433+0521

Fig. 39. 0430+052.

0430+052   J0433+0521

$\alpha_{LF} = -0.30 \pm 0.02$ $\alpha_{HF} = -0.34 \pm 0.05$

Fig. 40. 0446+112.
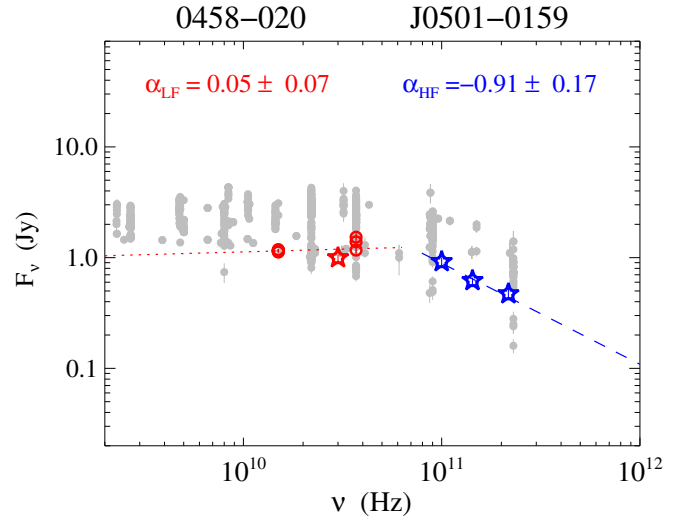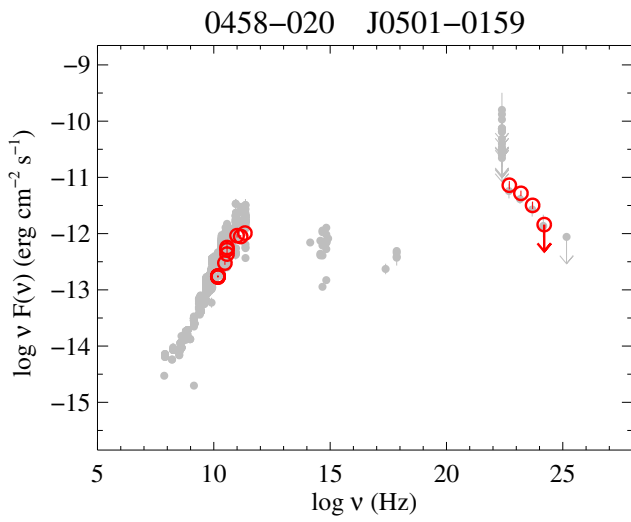
Fig. 41. 0458−020.
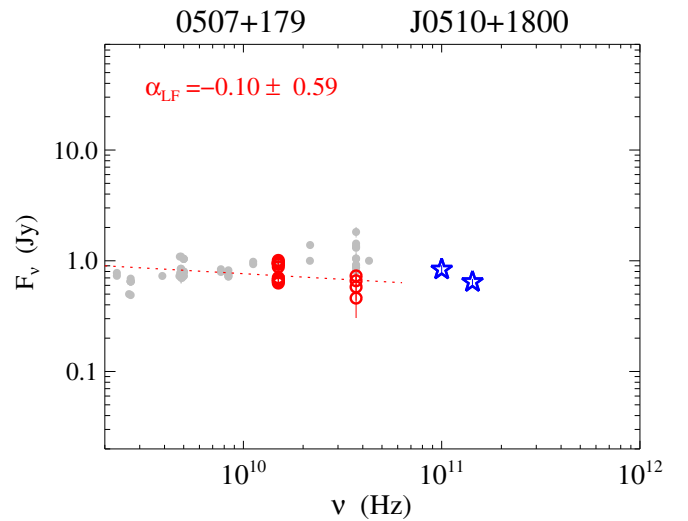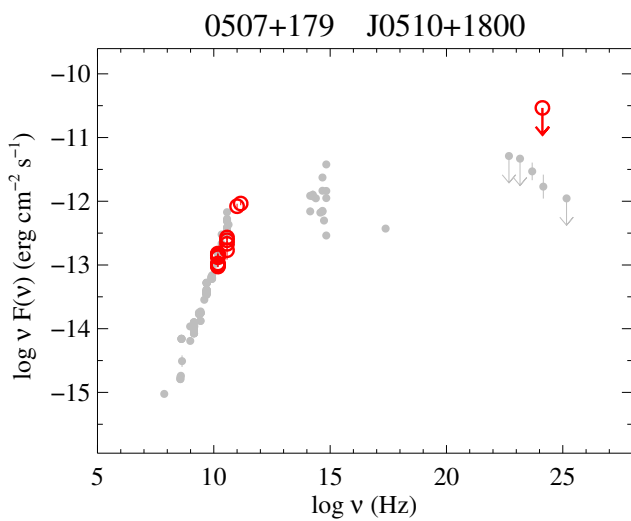
Fig. 42. 0507+179.
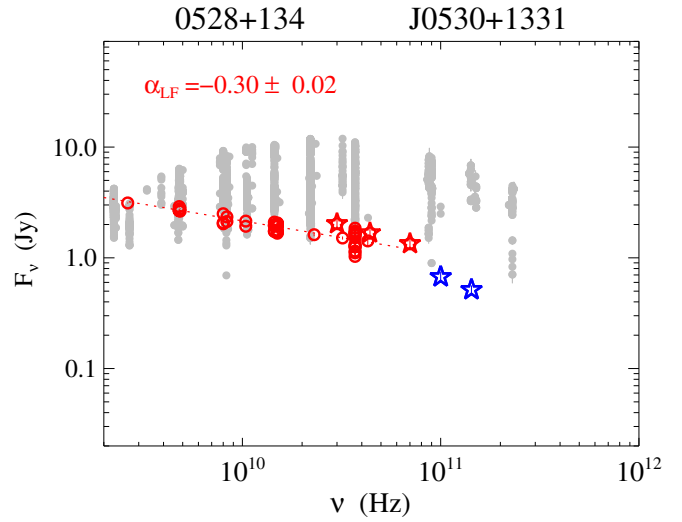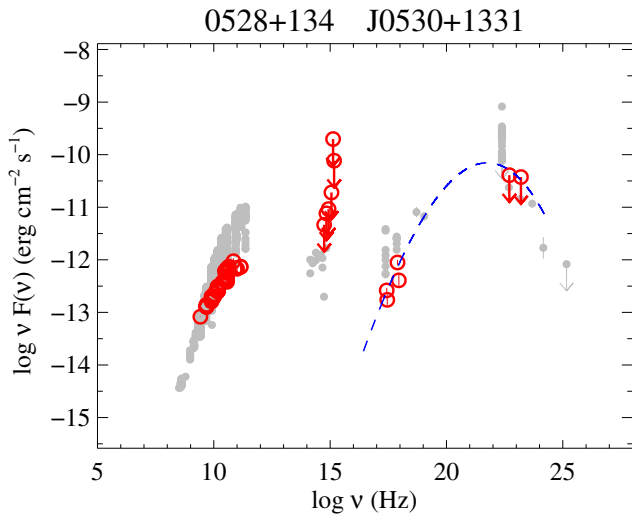
Fig. 43. 0528+134.
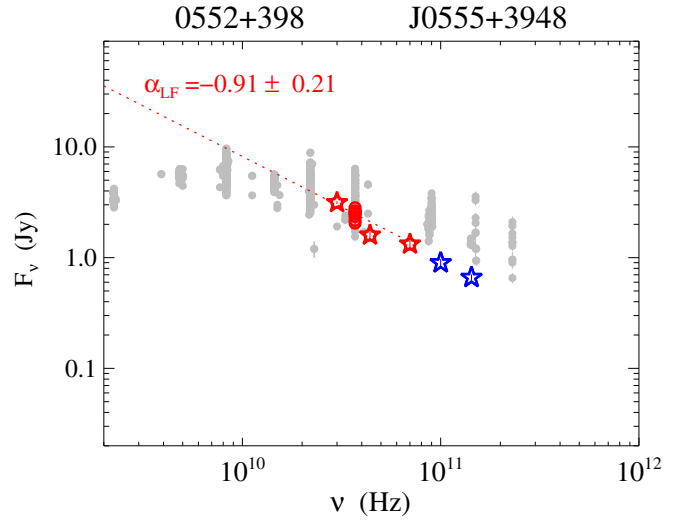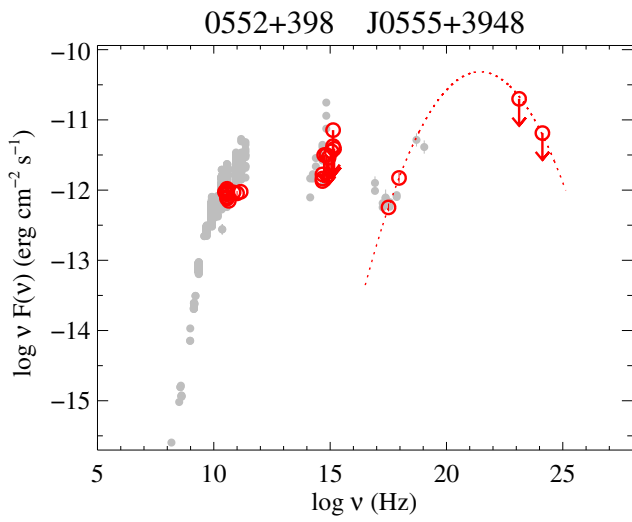
Fig. 44. 0552+398.

Fig. 45. 0605−085.

0642+449   J0646+4451

0642+449   J0646+4451

$\alpha_{LF} = -0.05 \pm 0.04$ $\alpha_{HF} = -0.70 \pm 0.01$

Fig. 46. 0642+449.

0716+714   J0721+7120

0716+714   J0721+7120

$\alpha_{LF} = 0.13 \pm 0.04$ $\alpha_{HF} = -0.27 \pm 0.03$

Fig. 47. 0716+714.

0723−008   J0725−0054

0723−008   J0725−0054

$\alpha_{LF} = 0.16 \pm 0.03$ $\alpha_{HF} = -0.49 \pm 0.03$
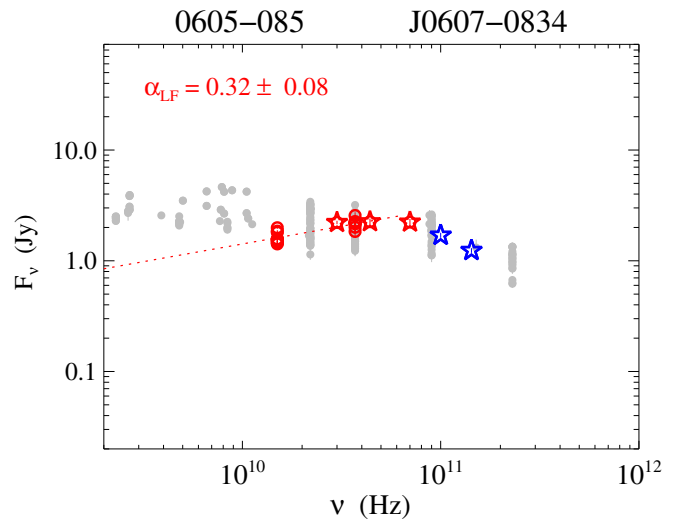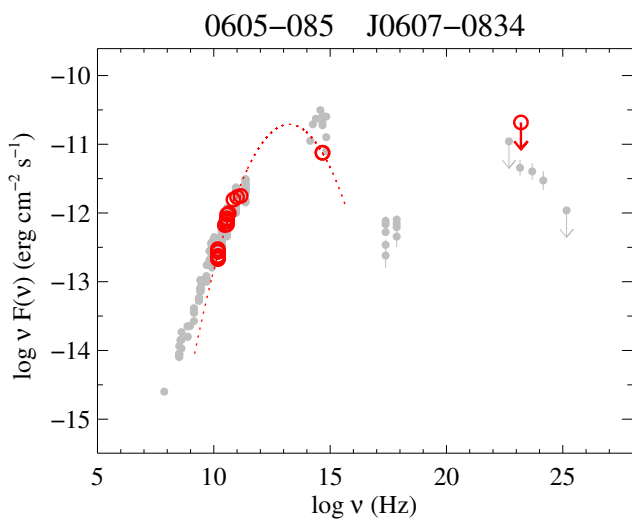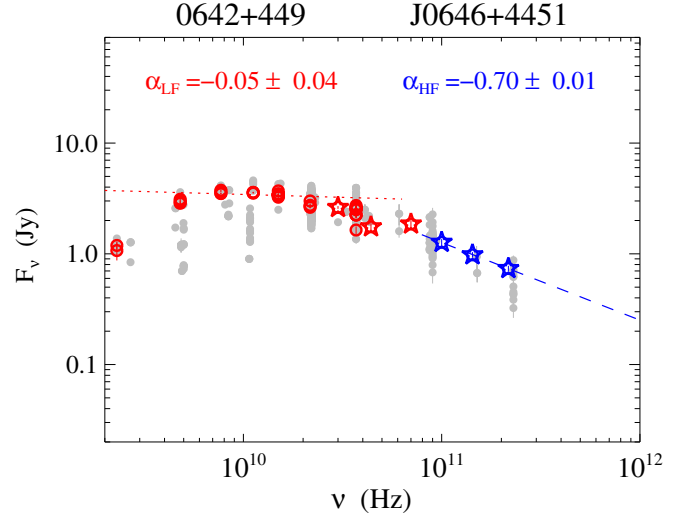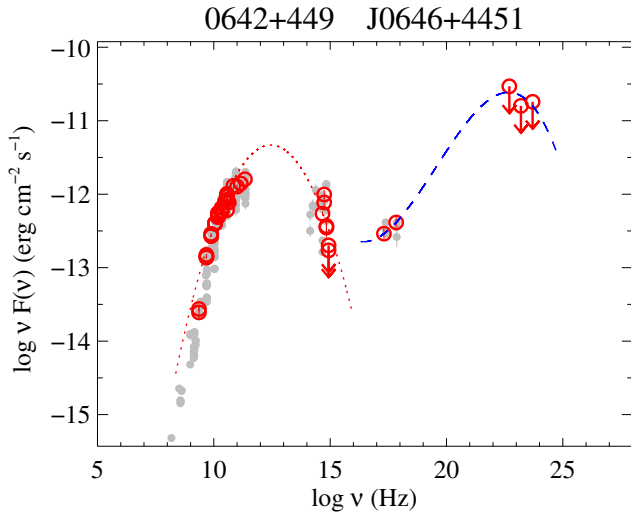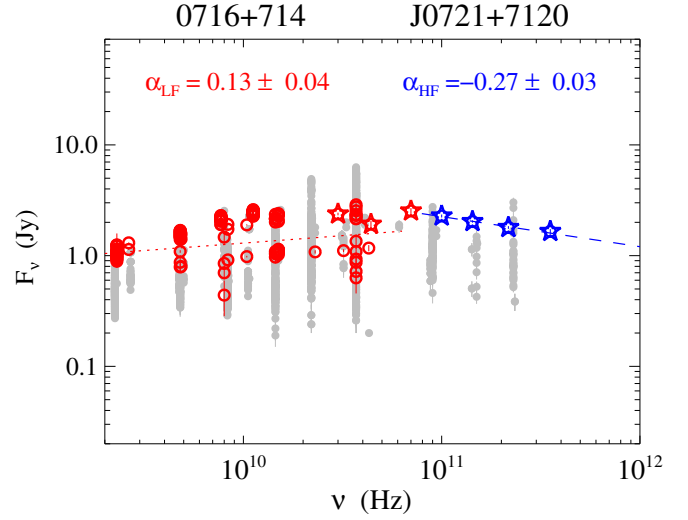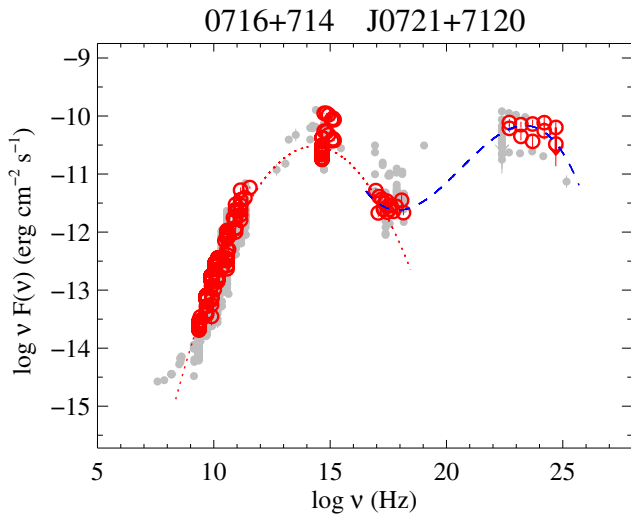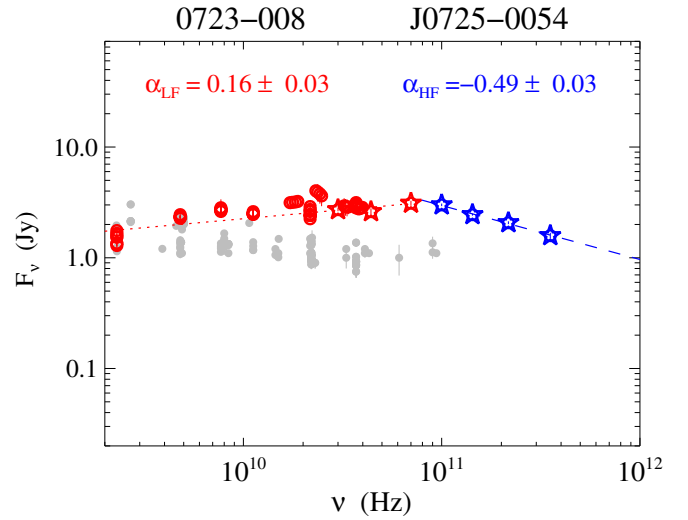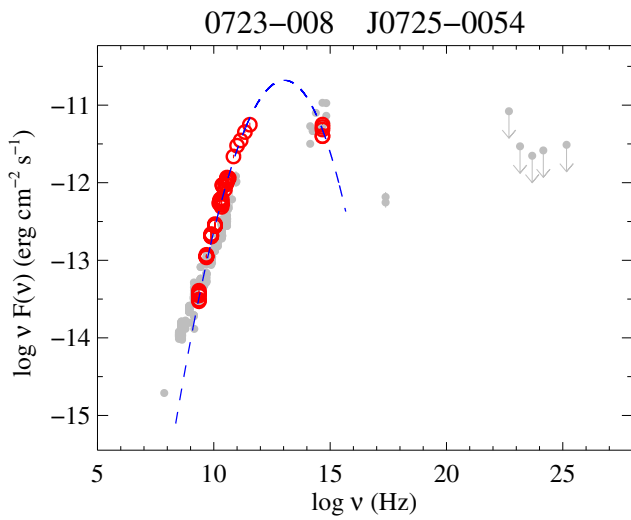
Fig. 48. 0723−008.
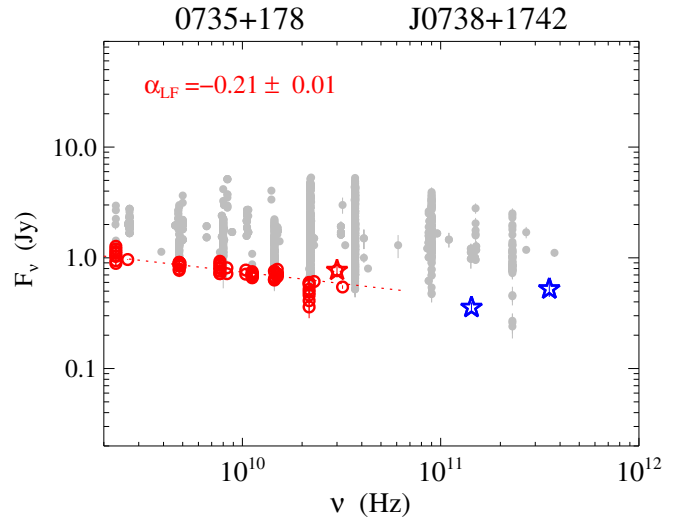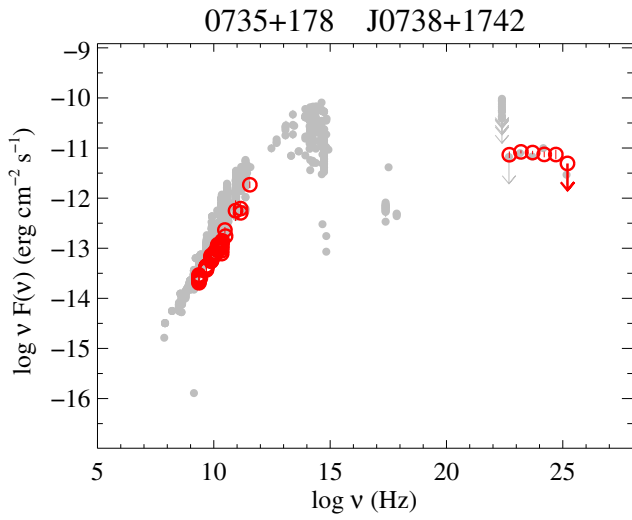
Fig. 49. 0735+178.
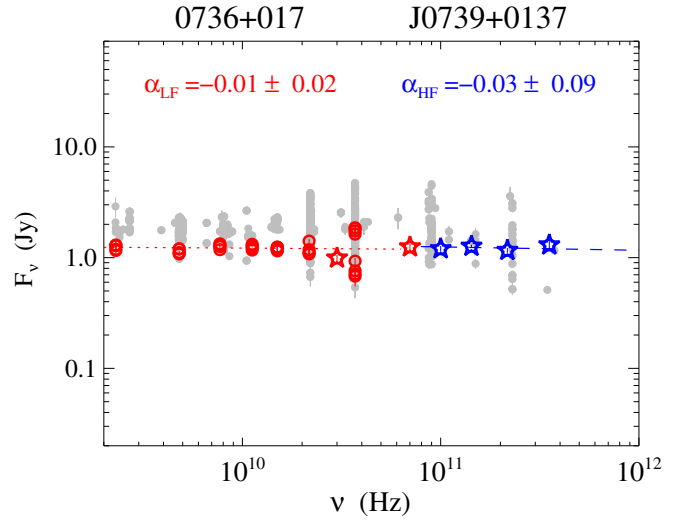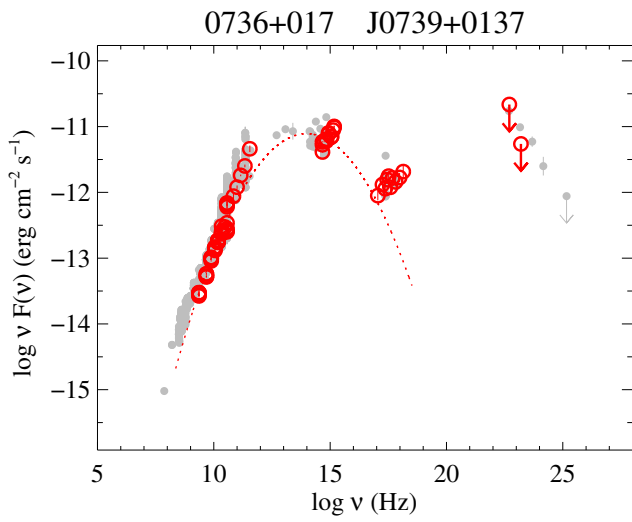
Fig. 50. 0736+017.
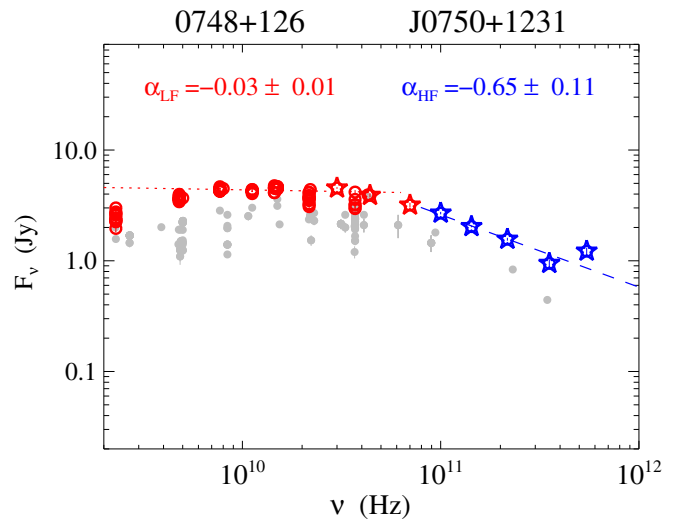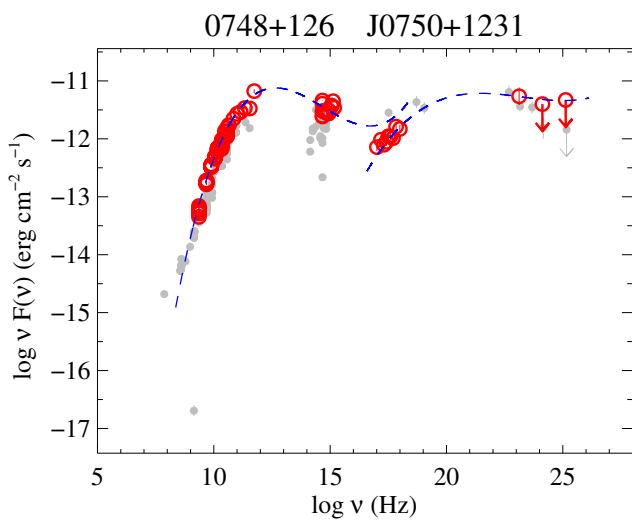
Fig. 51. 0748+126.

0754+100   J0757+0956

0754+100   J0757+0956

$\alpha_{LF} = 0.15 \pm 0.01$ $\alpha_{HF} = -0.51 \pm 0.03$

Fig. 52. 0754+100.

0805−077   J0808−0751

0805−077   J0808−0751

$\alpha_{LF} = -0.11 \pm 0.01$ $\alpha_{HF} = -0.51 \pm 0.05$

Fig. 53. 0805−077.

0804+499   J0808+4950

0804+499   J0808+4950

$\alpha_{LF} = 0.18 \pm 0.04$

Fig. 54. 0804+499.

0823+033   J0825+0309

0823+033   J0825+0309

Fig. 55. 0823+033.

0827+243   J0830+2411

0827+243   J0830+2411

Fig. 56. 0827+243.

0836+710   J0841+7053
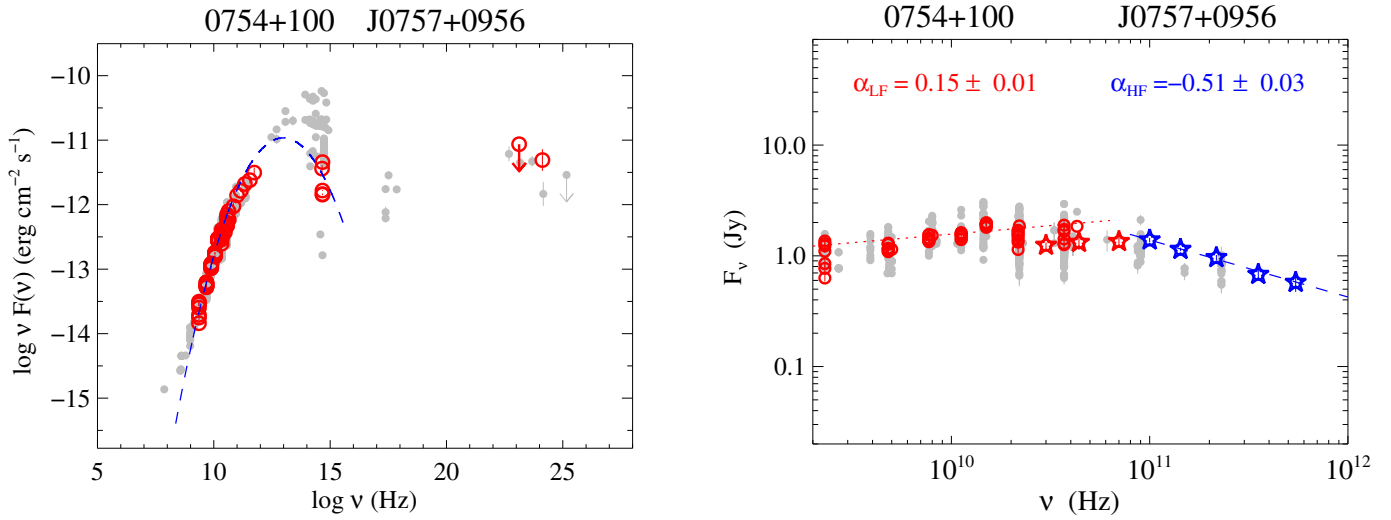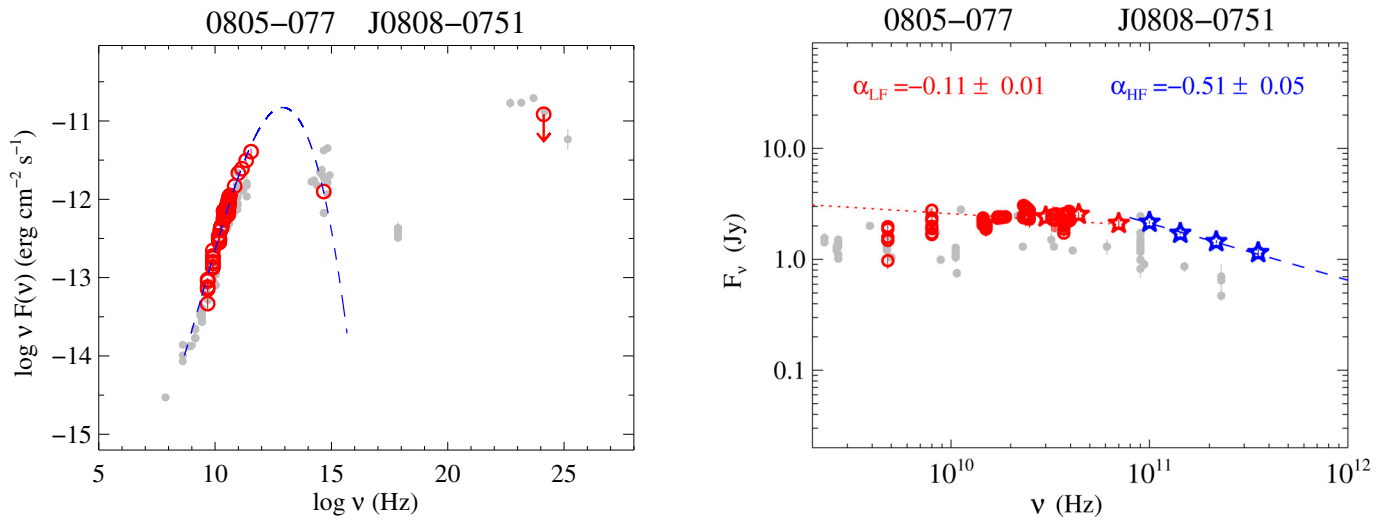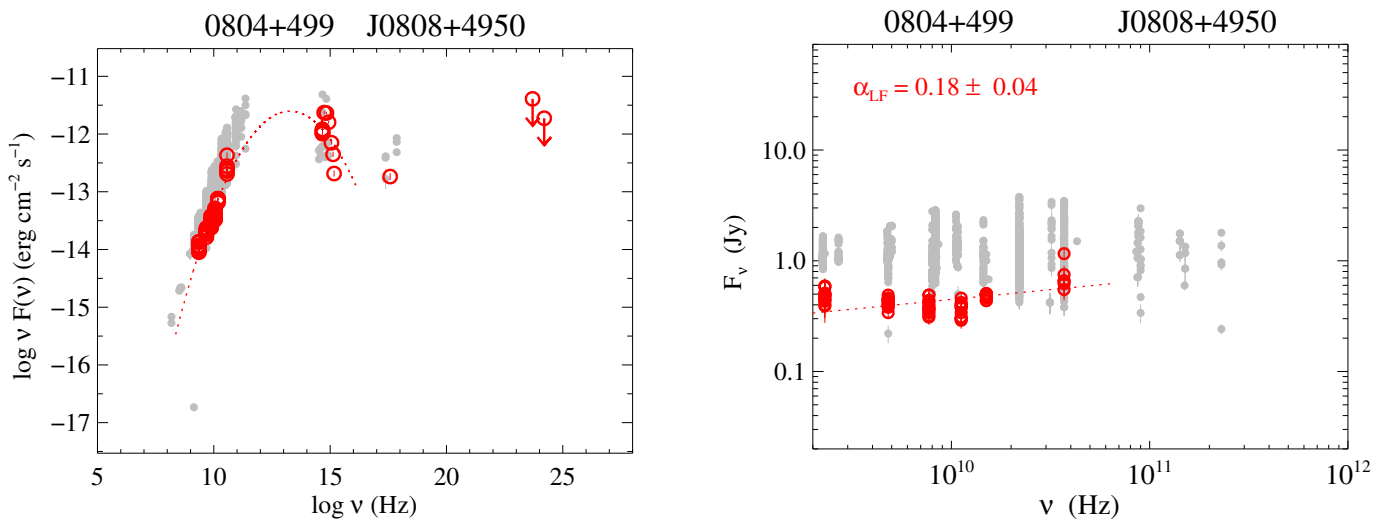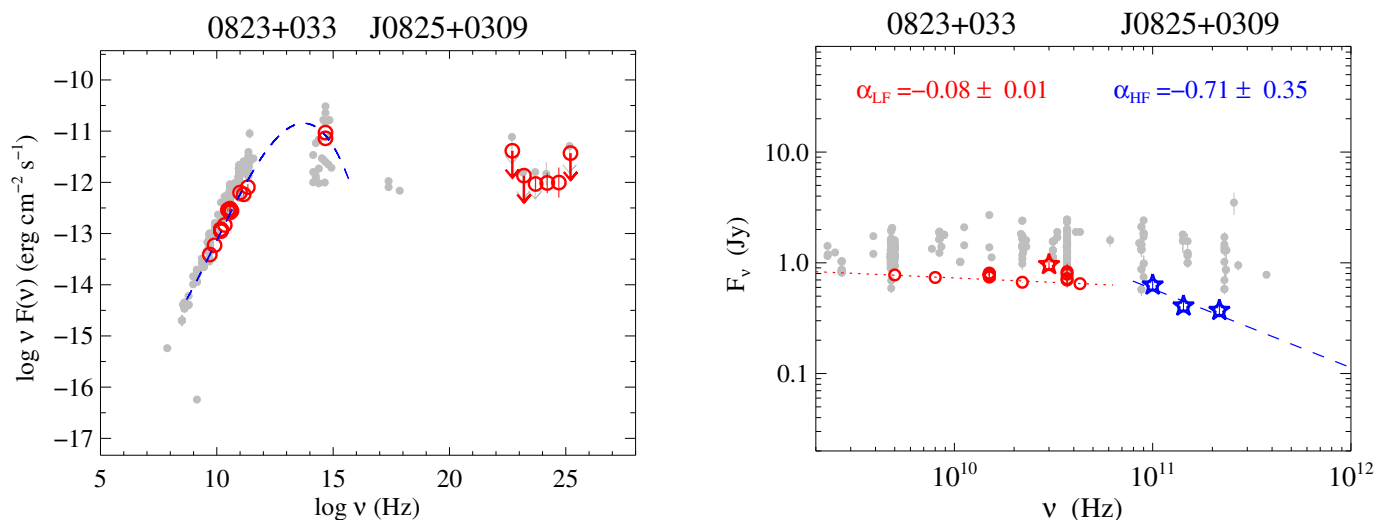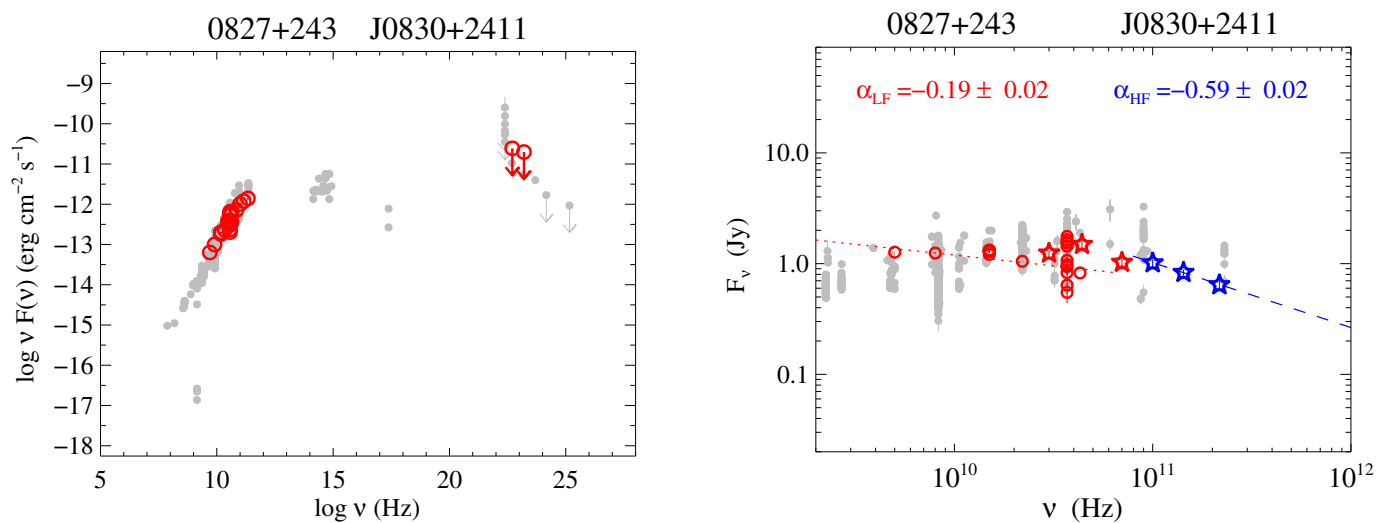
0836+710   J0841+7053
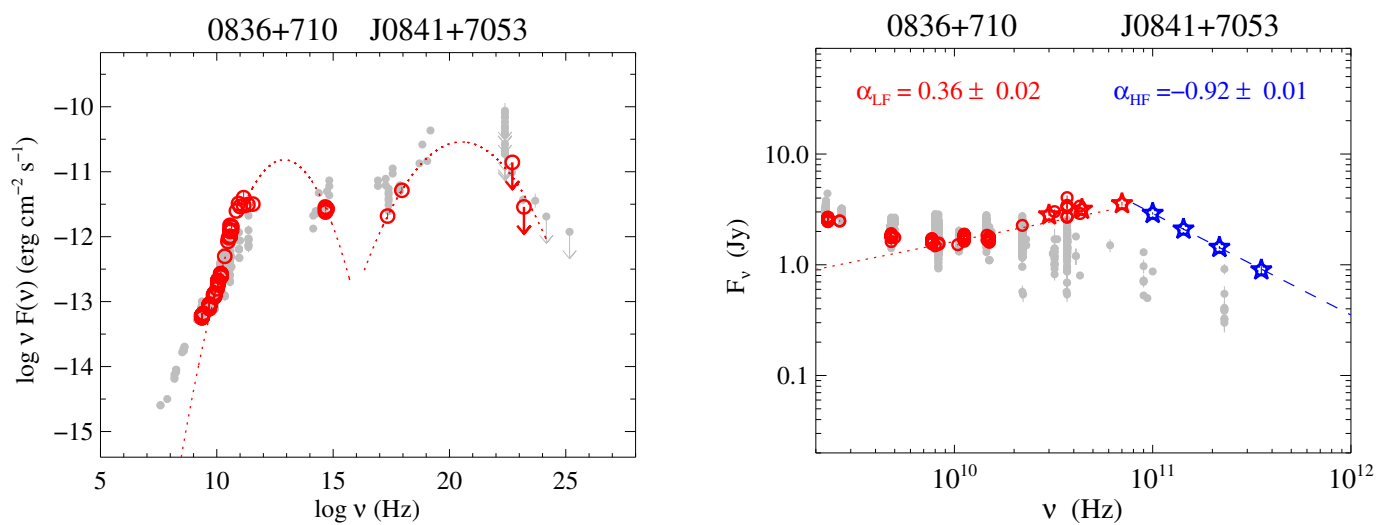
Fig. 57. 0836+710.
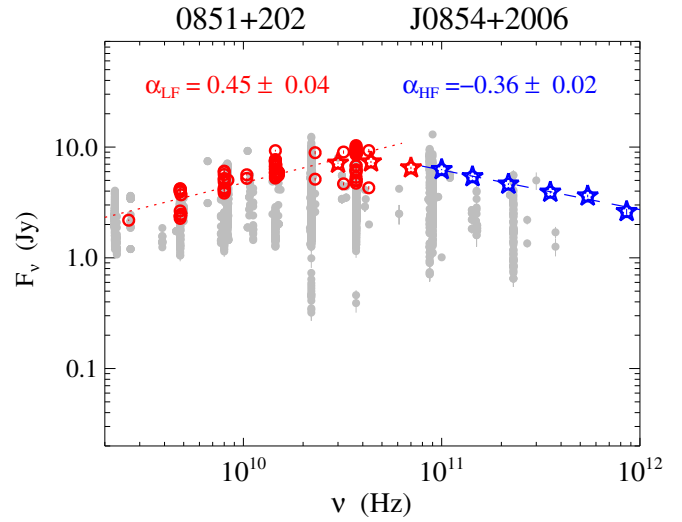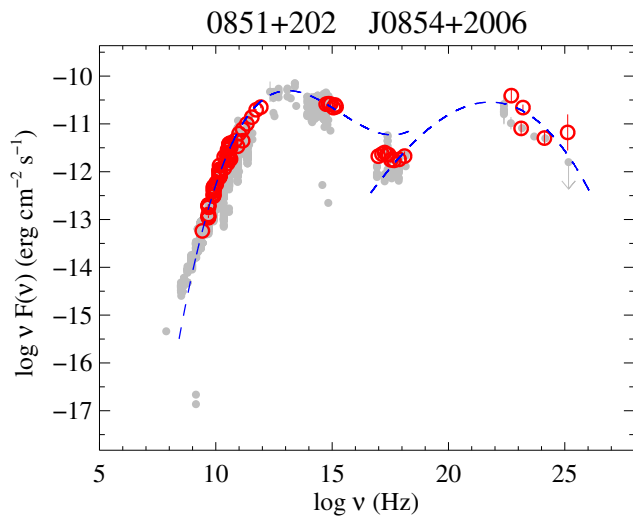
Fig. 58. 0851+202.
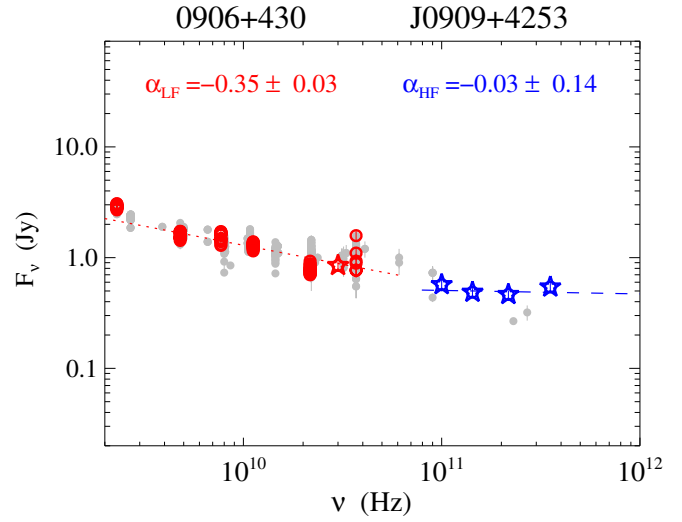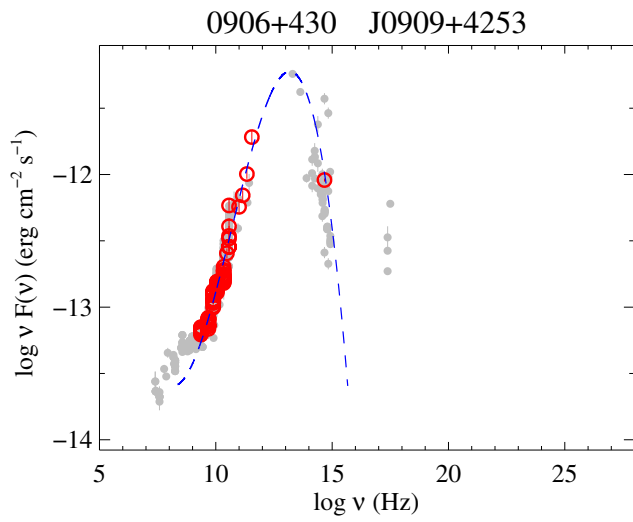
Fig. 59. 0906+430.
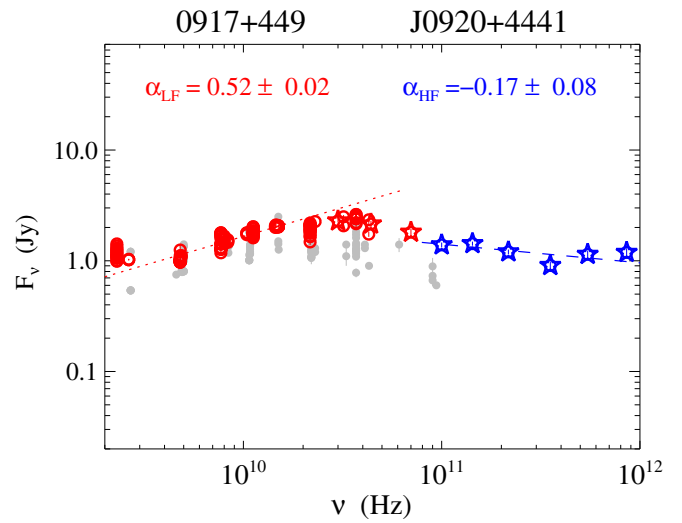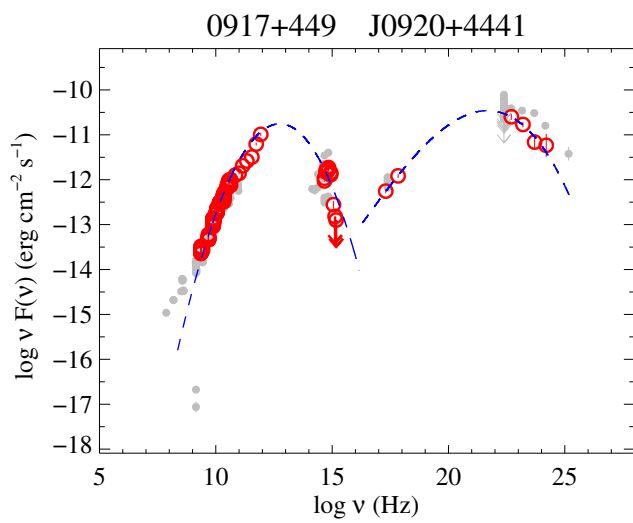
Fig. 60. 0917+449.
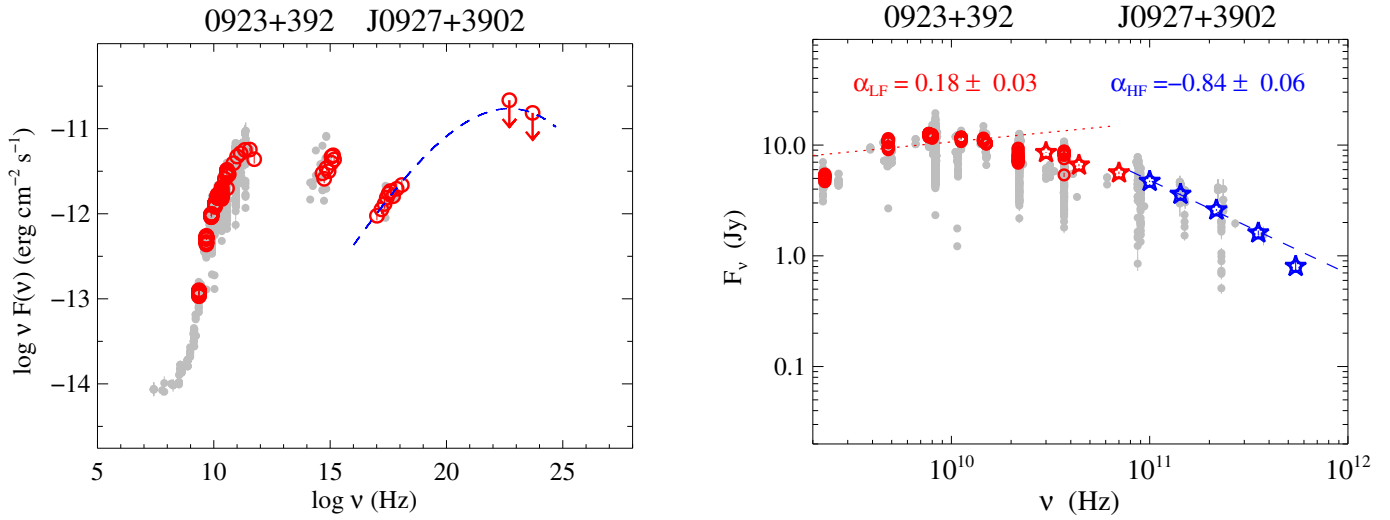
Fig. 61. 0923+392.
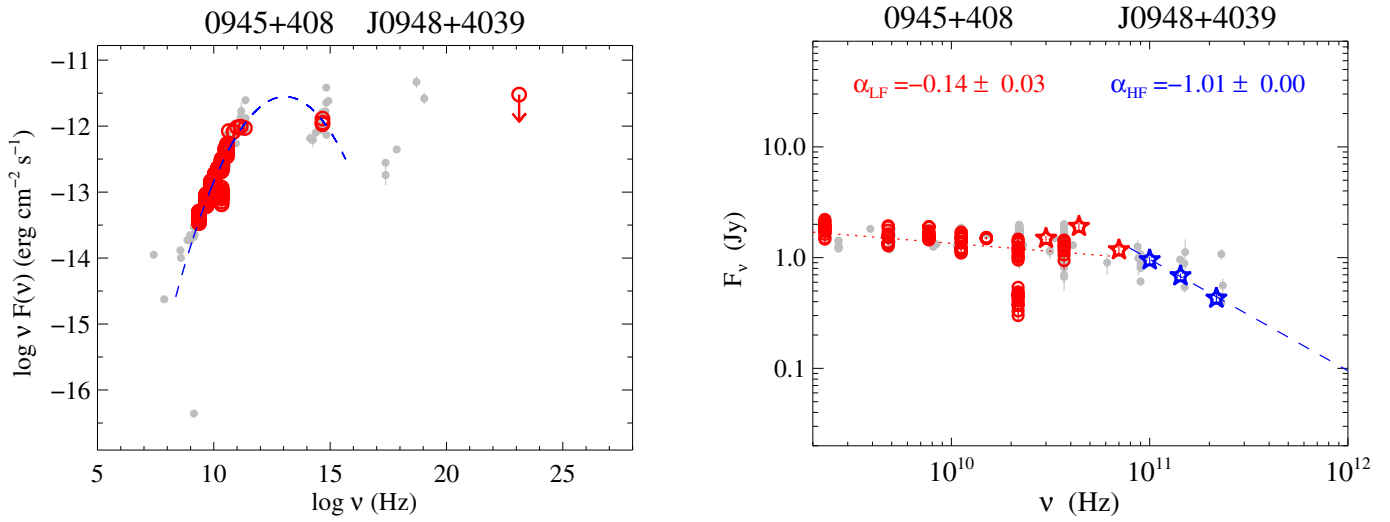
Fig. 62. 0945+408.
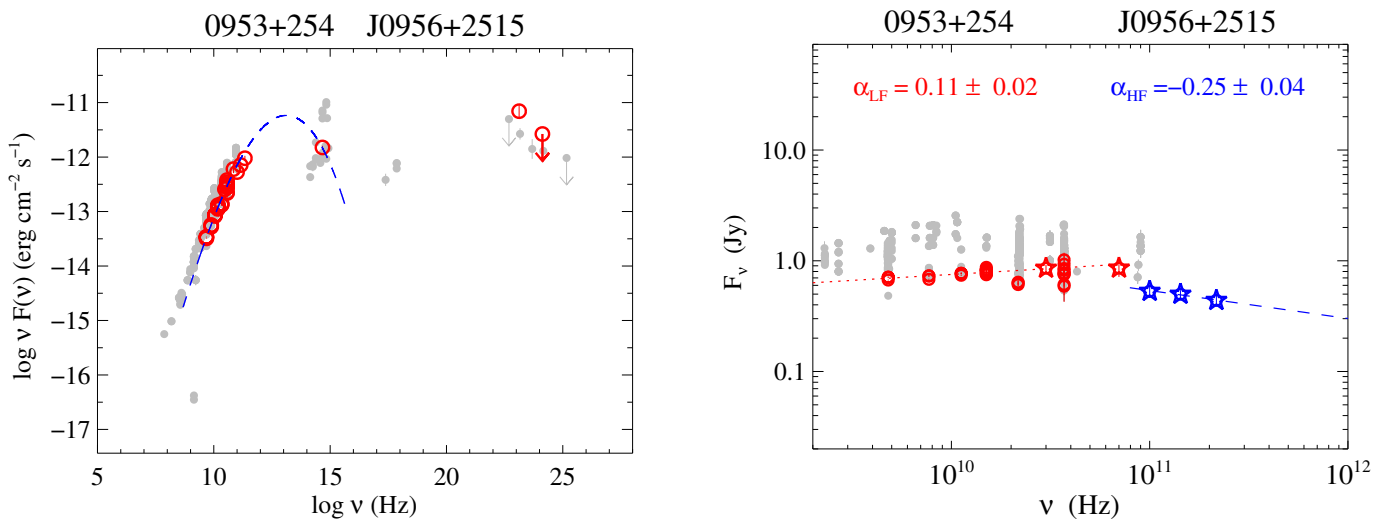
Fig. 63. 0953+254.
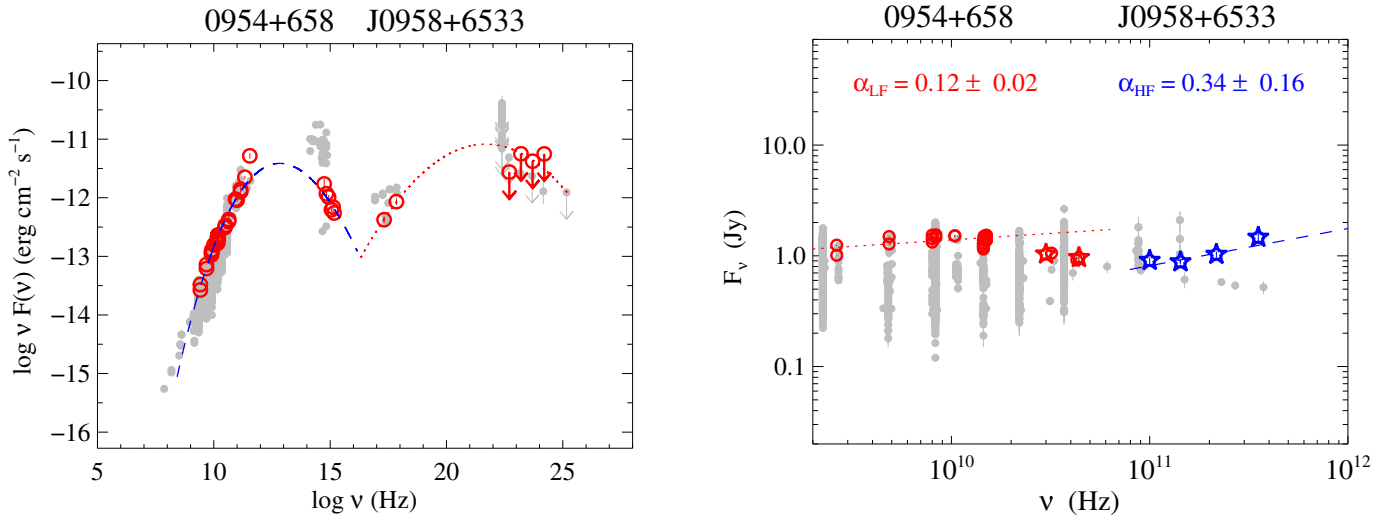
Fig. 64. 0954+658.
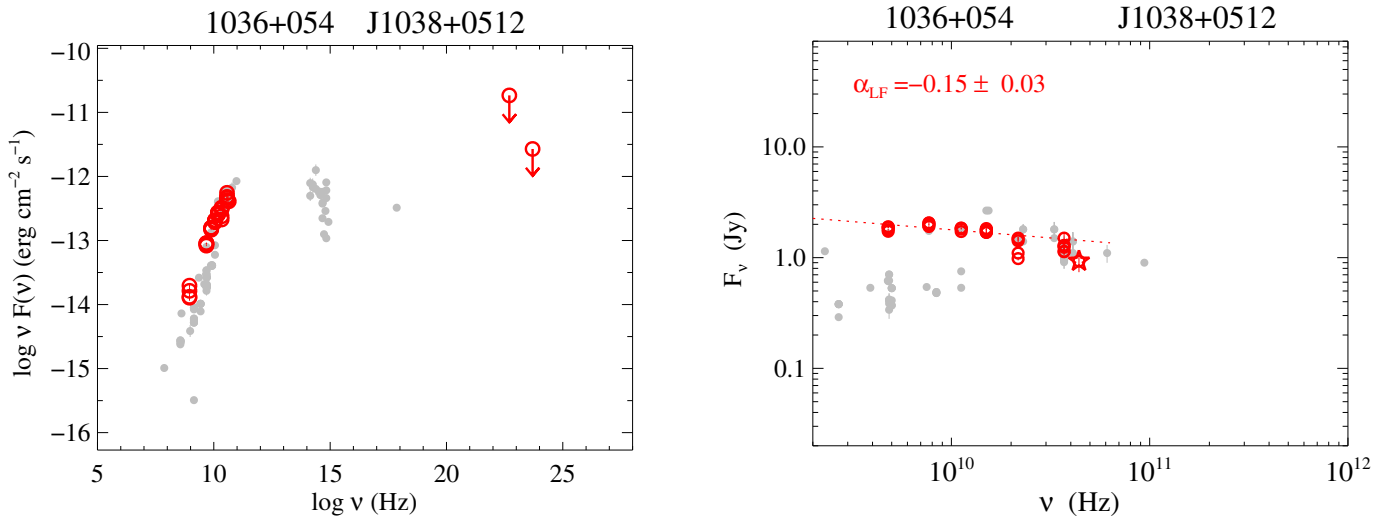
Fig. 65. 1036+054.

Fig. 66. TEX1040+244.

1055+018   J1058+0133

Fig. 67. 1055+018.

J1130+3815   J1130+3815

Fig. 68. J1130+3815.

1150+812   J1153+8058
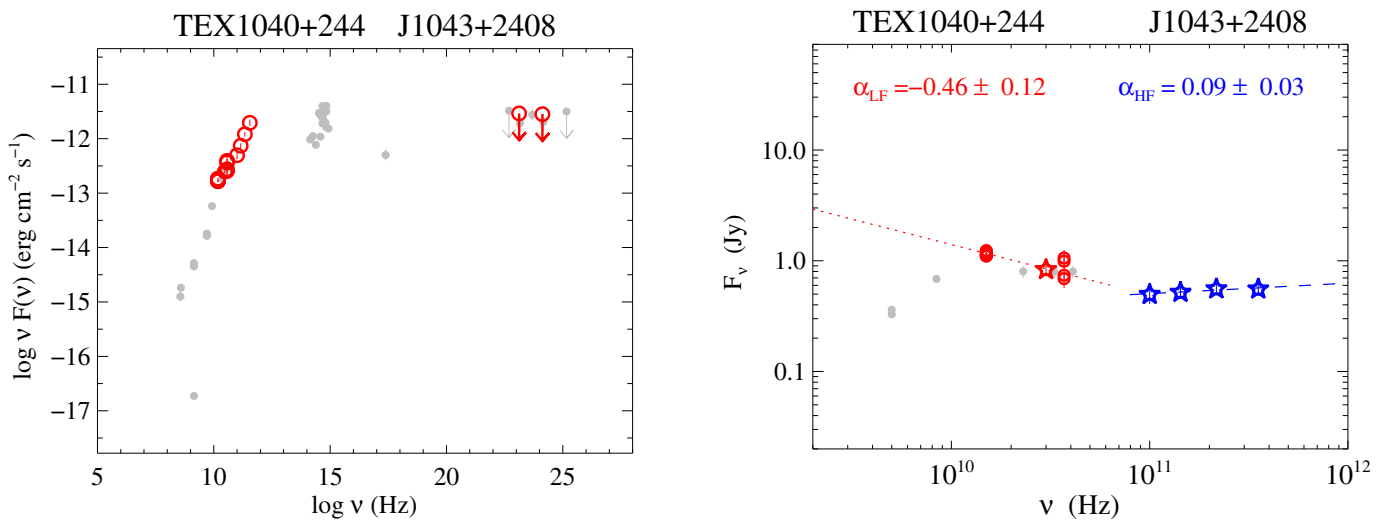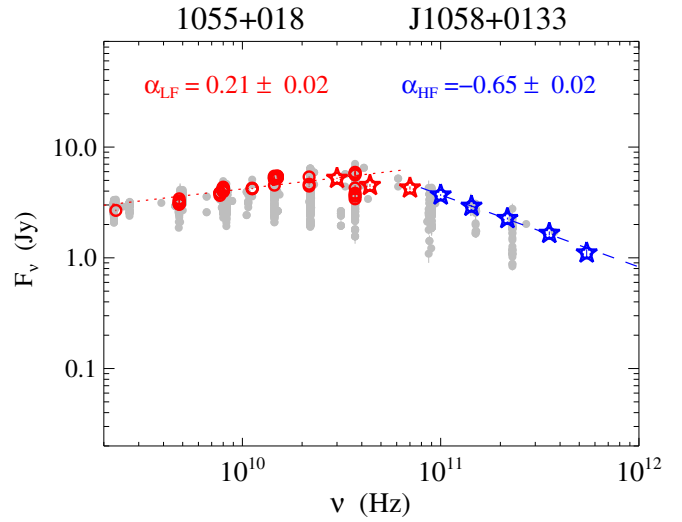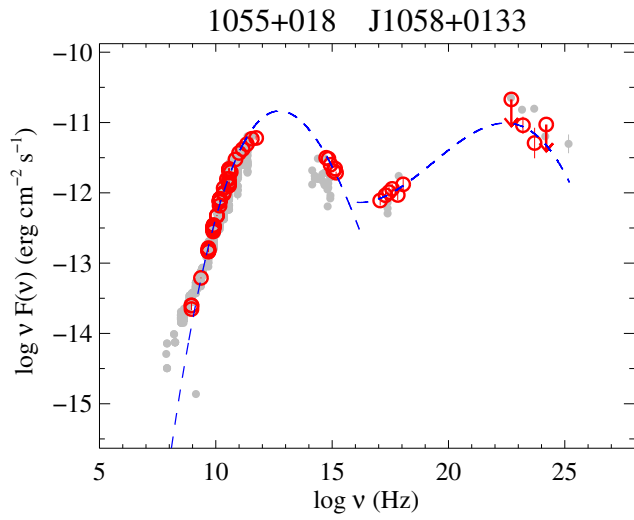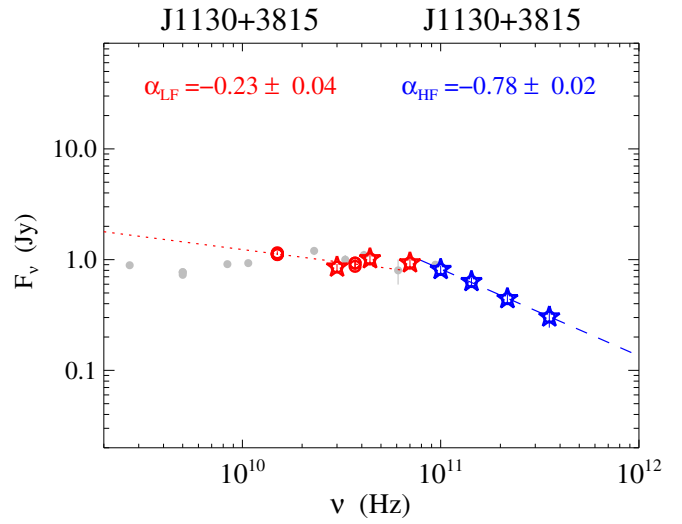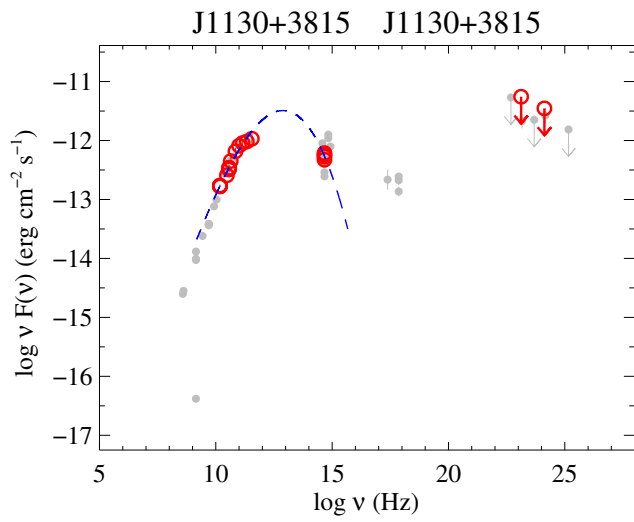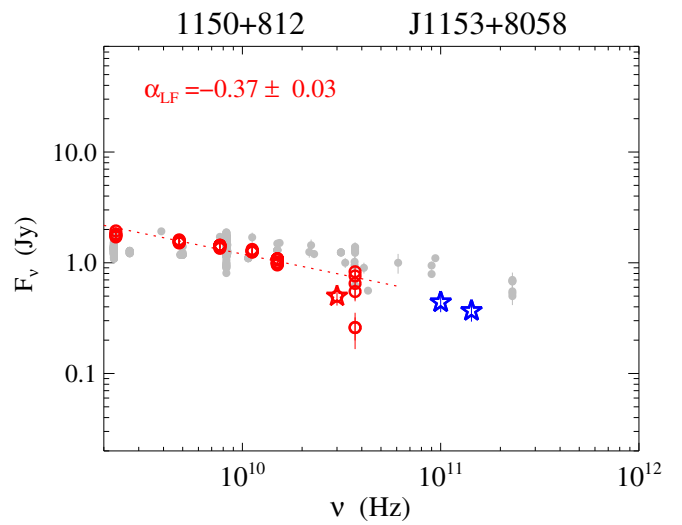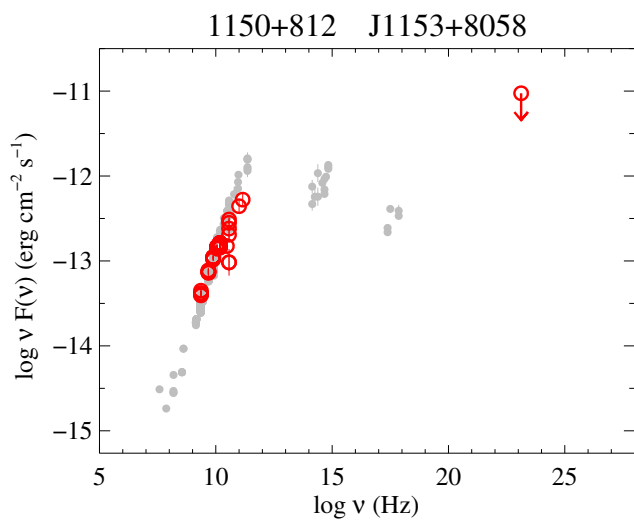
Fig. 69. 1150+812.
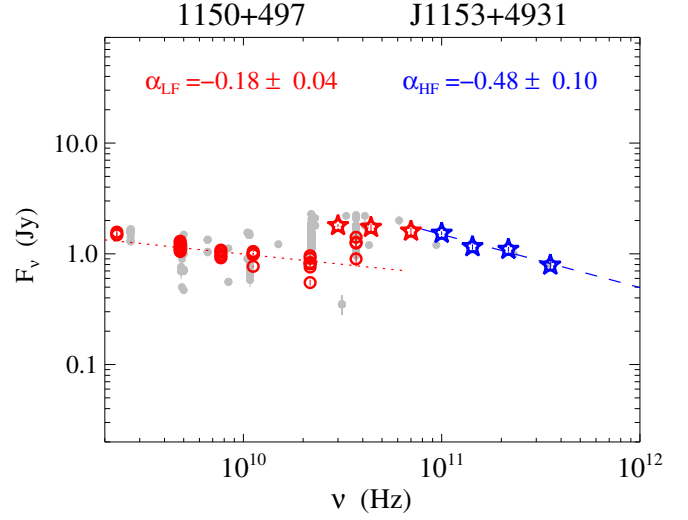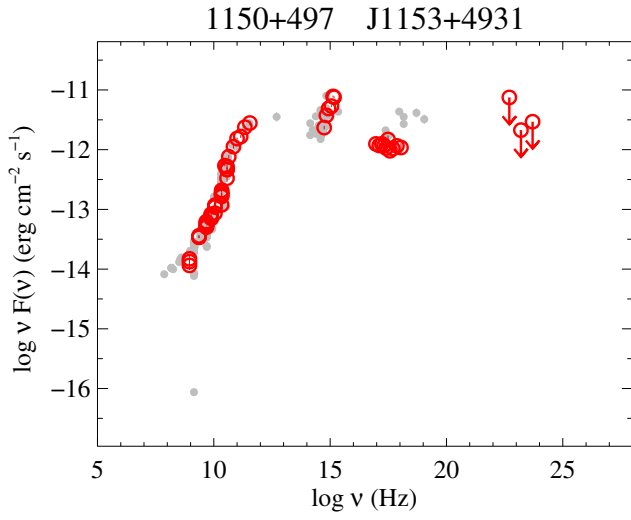
Fig. 70. 1150+497.
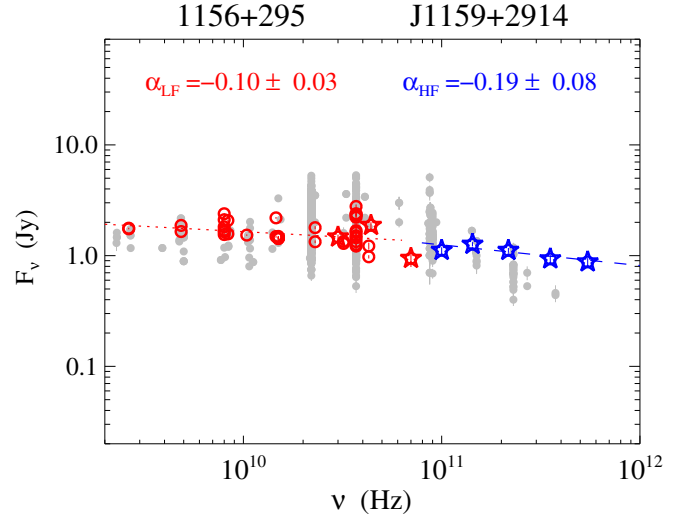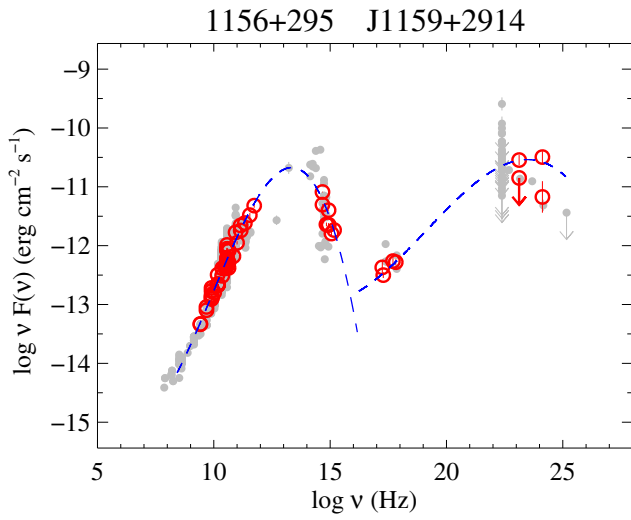
Fig. 71. 1156+295.
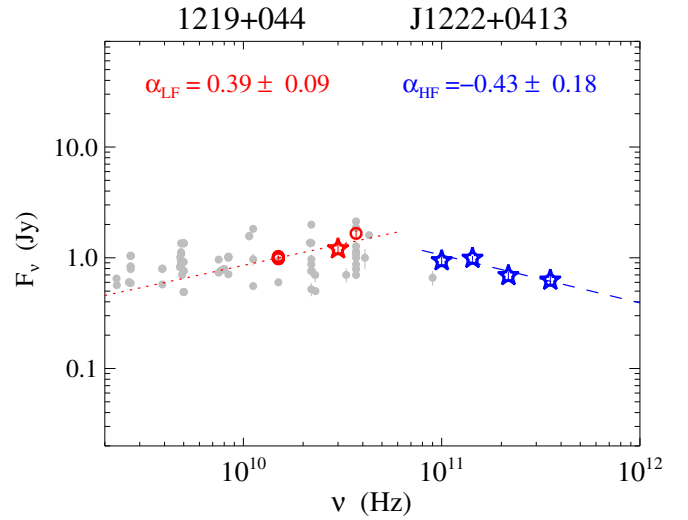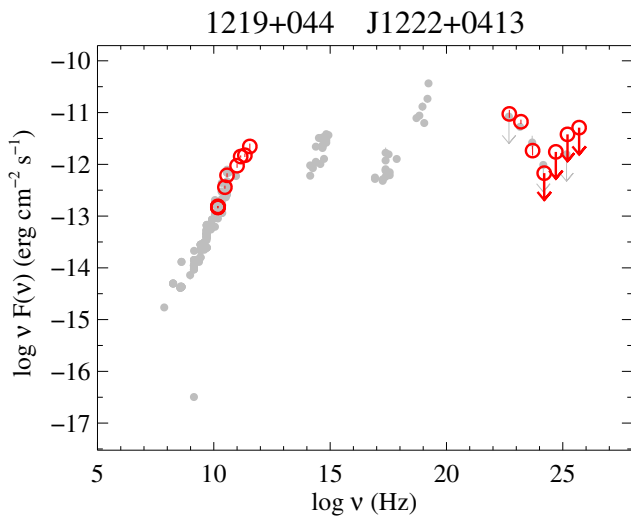
Fig. 72. 1219+044.

1222+216   J1224+2122

1222+216   J1224+2122

$\alpha_{LF} = 0.05 \pm 0.01$ $\alpha_{HF} = -0.76 \pm 0.07$

Fig. 73. 1222+216.

1226+023   J1229+0203

1226+023   J1229+0203

$\alpha_{LF} = -0.50 \pm -0.00$ $\alpha_{HF} = -0.78 \pm 0.02$

Fig. 74. 1226+023.

1228+126   J1230+1223

1228+126   J1230+1223

$\alpha_{LF} = -1.45 \pm 0.01$ $\alpha_{HF} = -0.80 \pm 0.06$

Fig. 75. 1228+126.

1253−055   J1256−0547

Fig. 76. 1253−055.

1308+326   J1310+3220

Fig. 77. 1308+326.

1324+224   J1327+2210
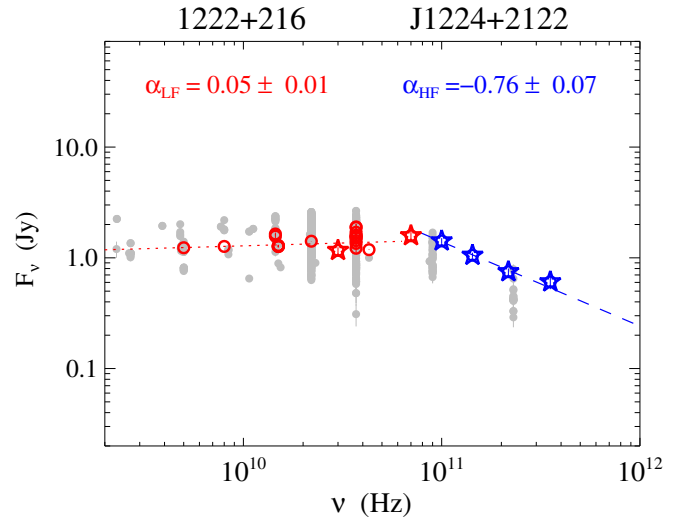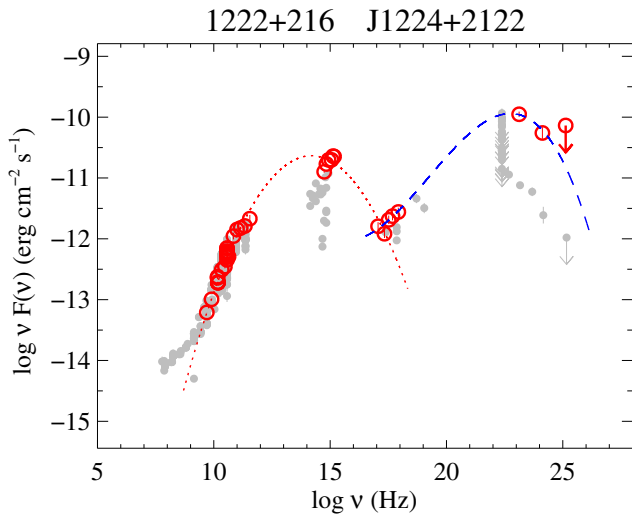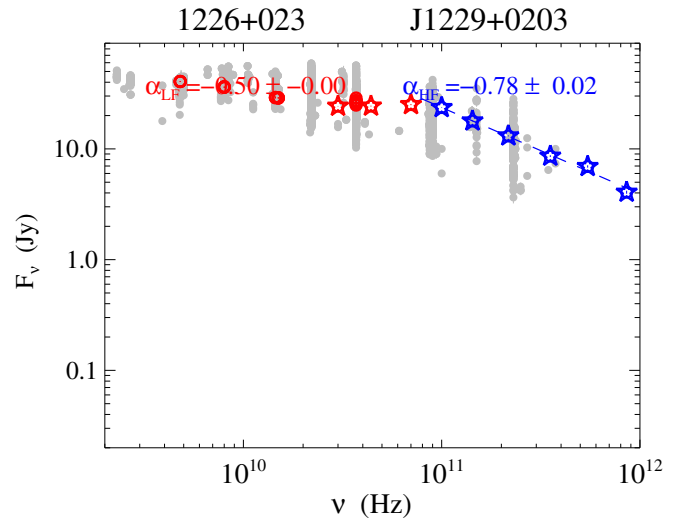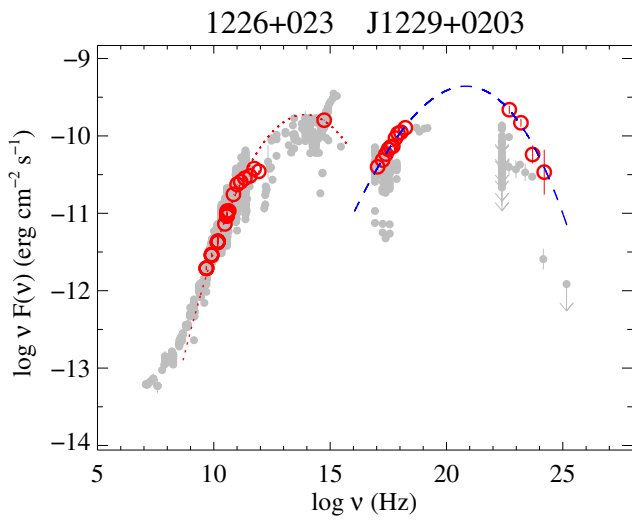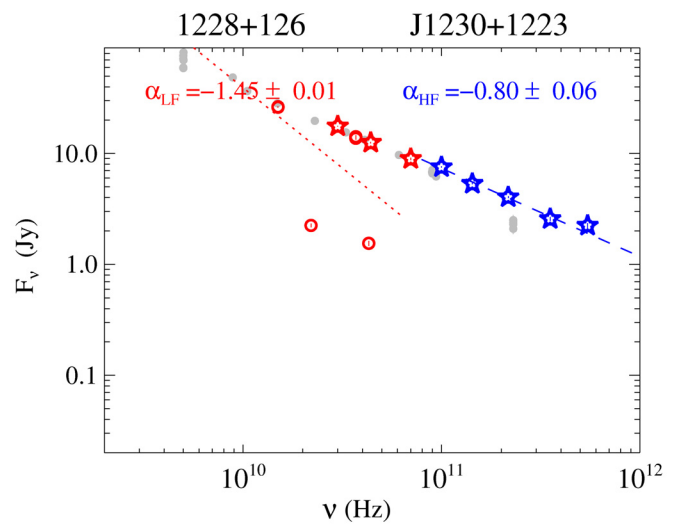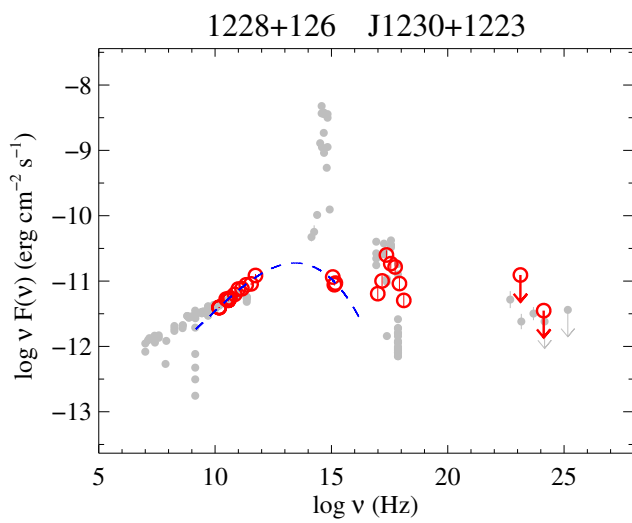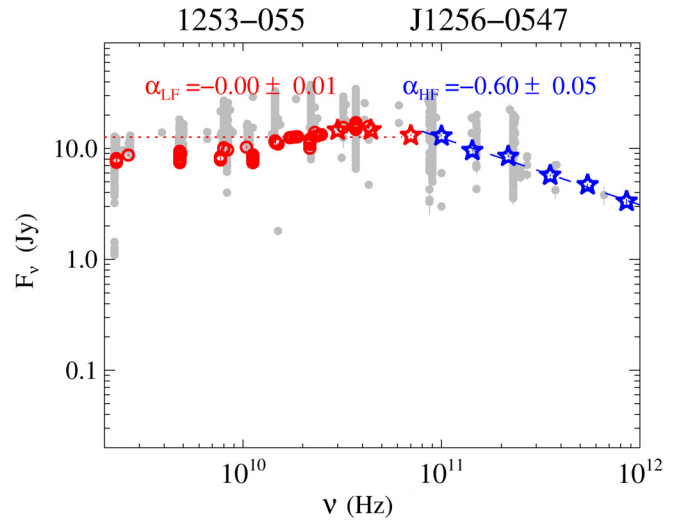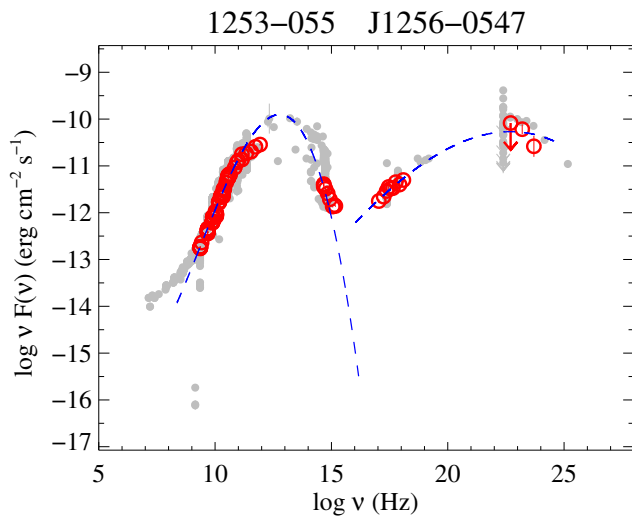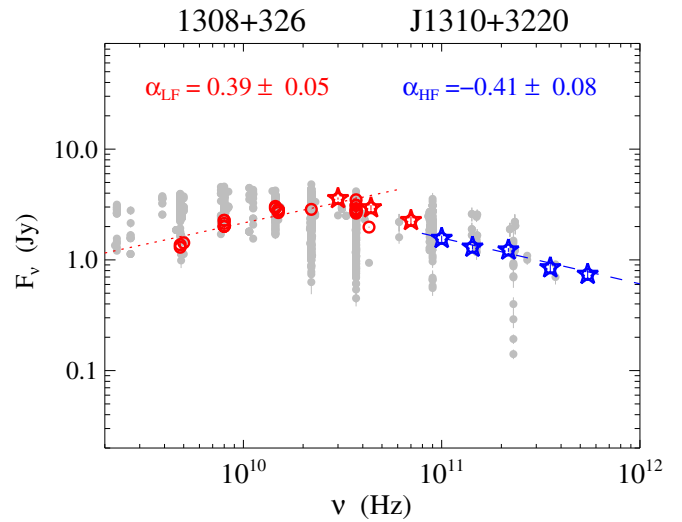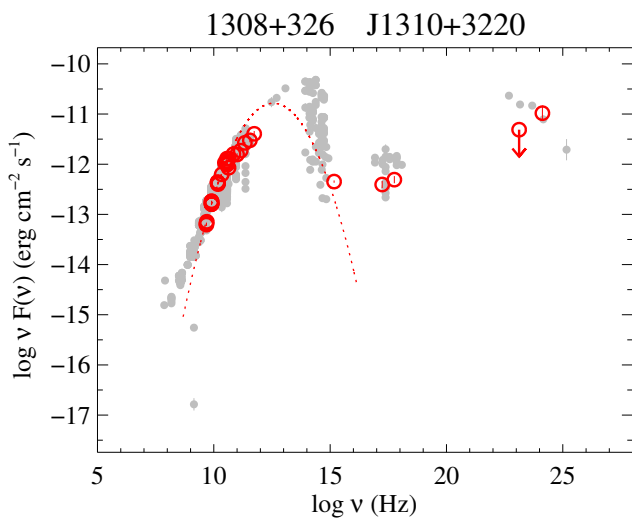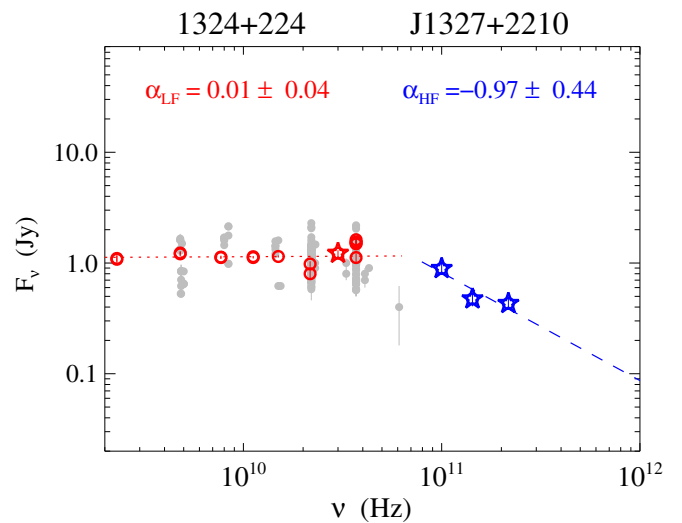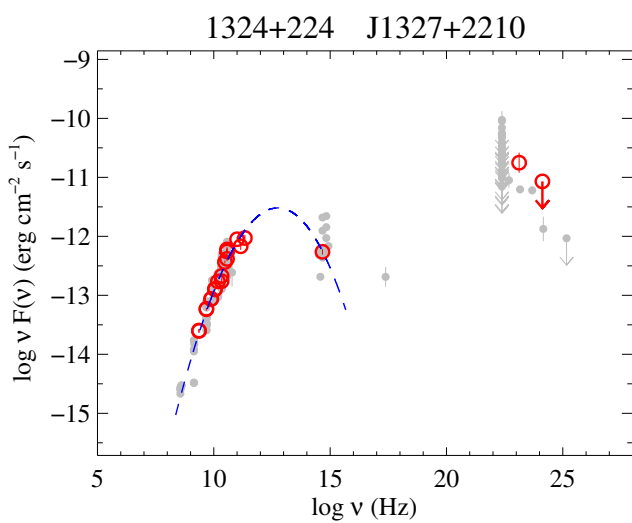
Fig. 78. 1324+224.
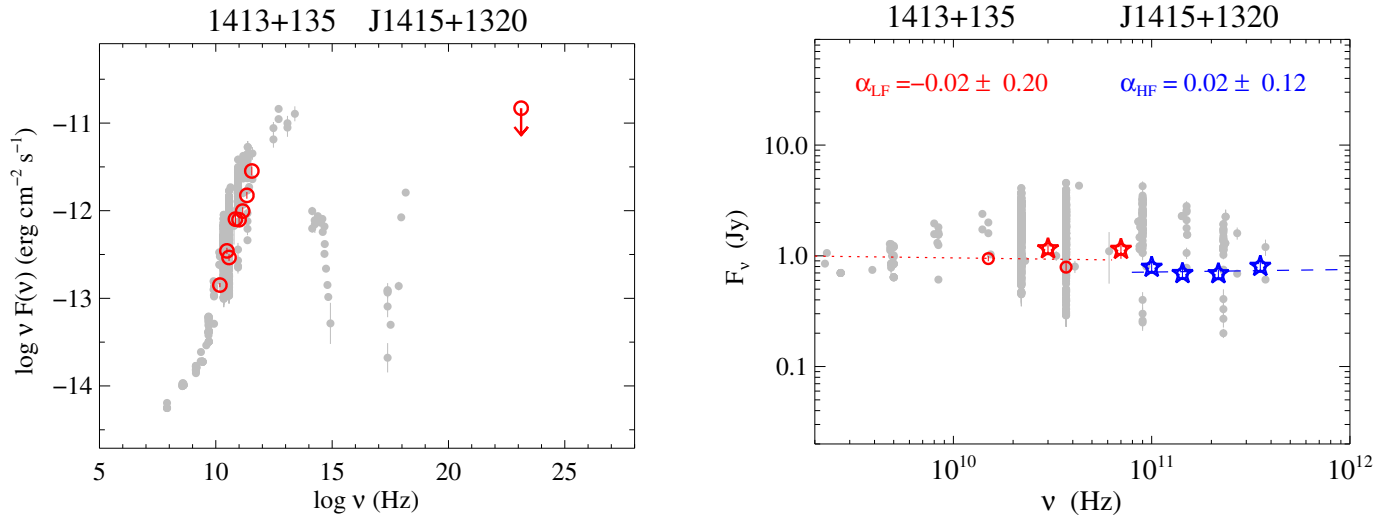
Fig. 79. 1413+135.
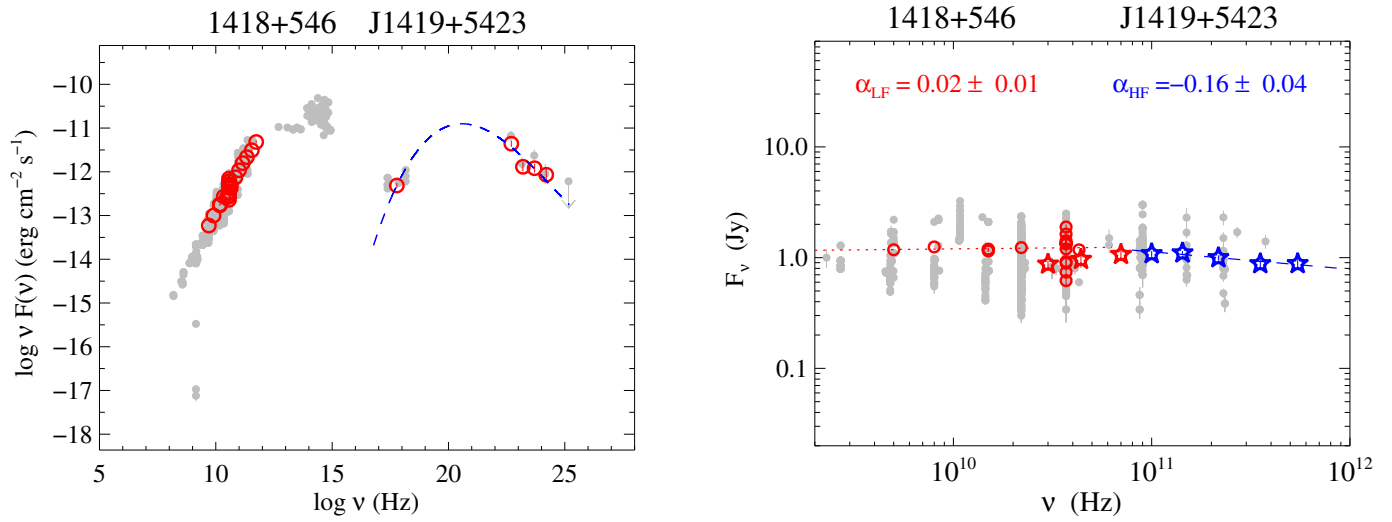
Fig. 80. 1418+546.

Fig. 81. 1502+106.

1510−089   J1512−0905

Fig. 82. 1510−089.

1546+027   J1549+0237
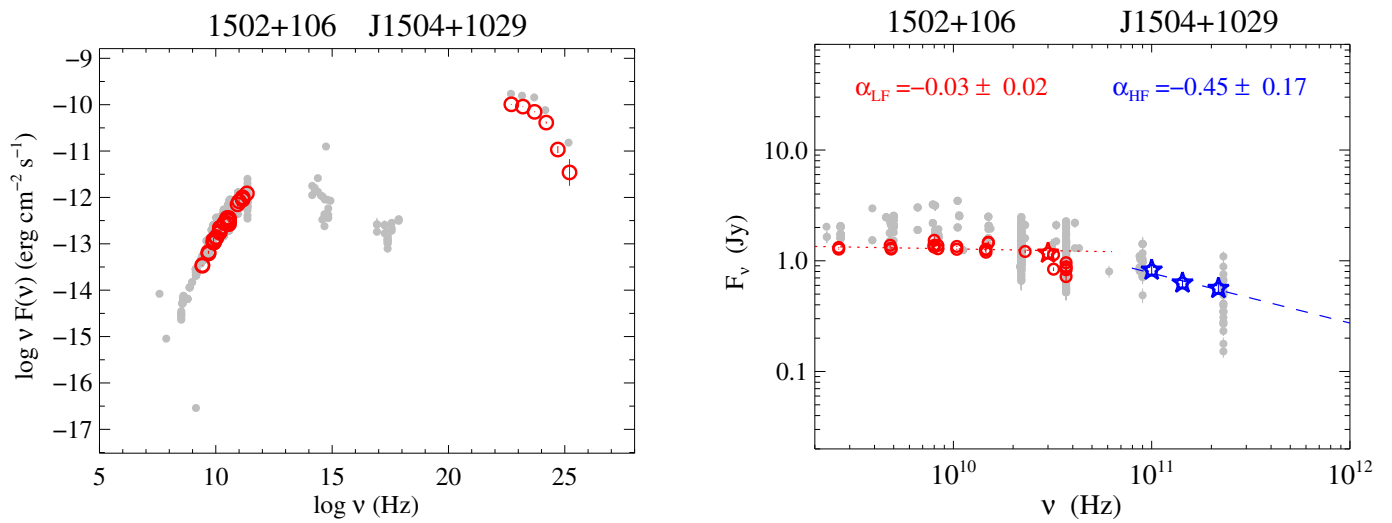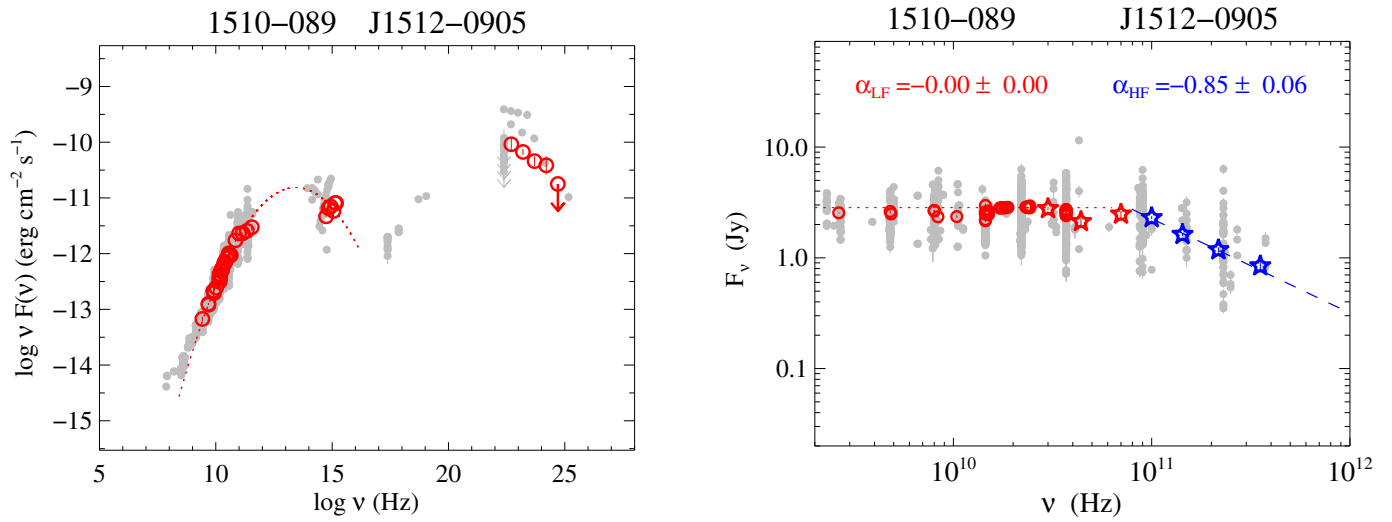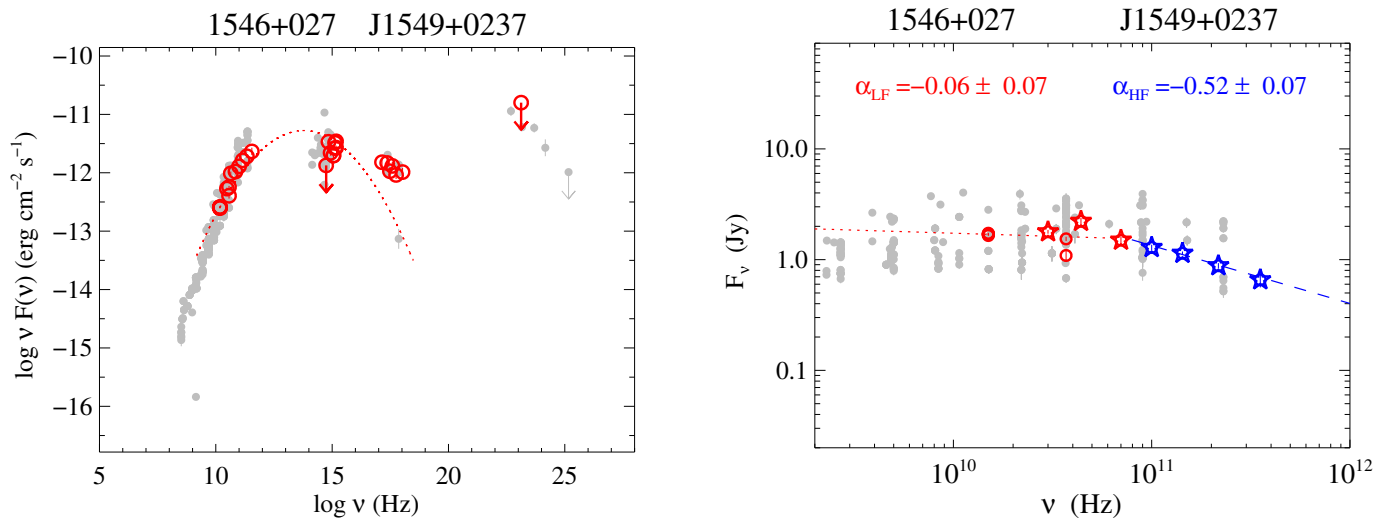
Fig. 83. 1546+027.

1548+056   J1550+0527
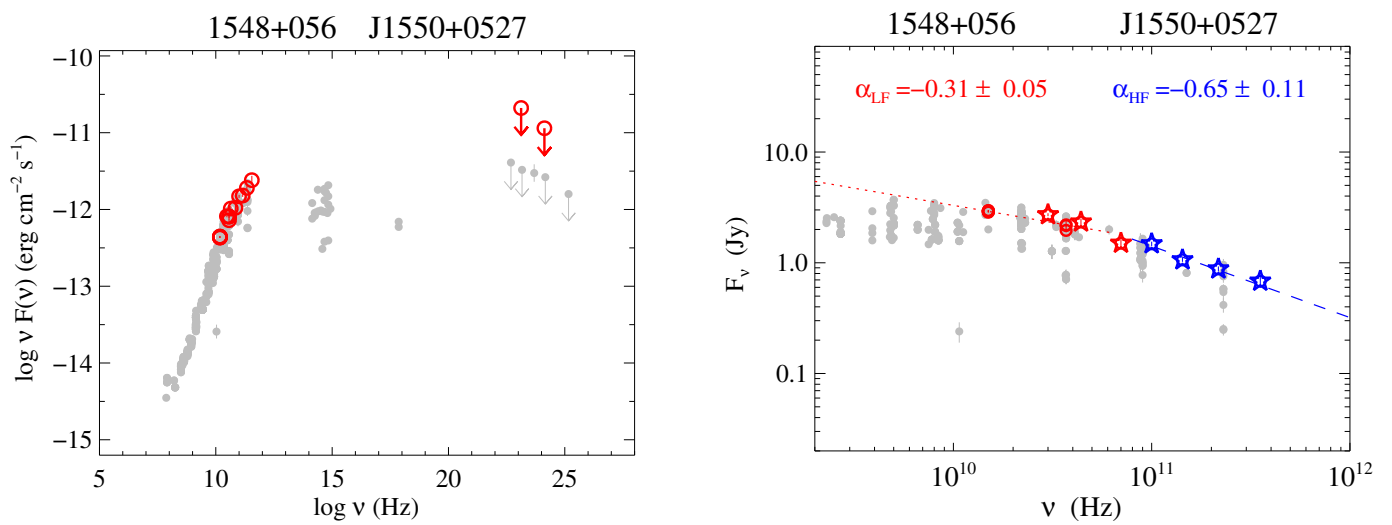
Fig. 84. 1548+056.
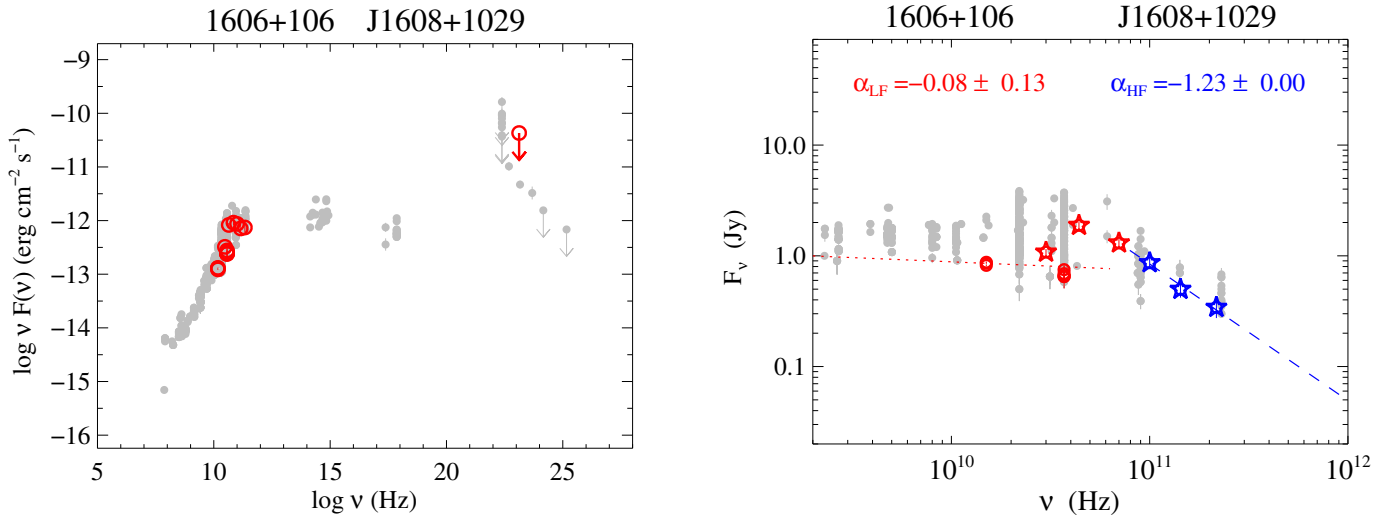
Fig. 85. 1606+106.
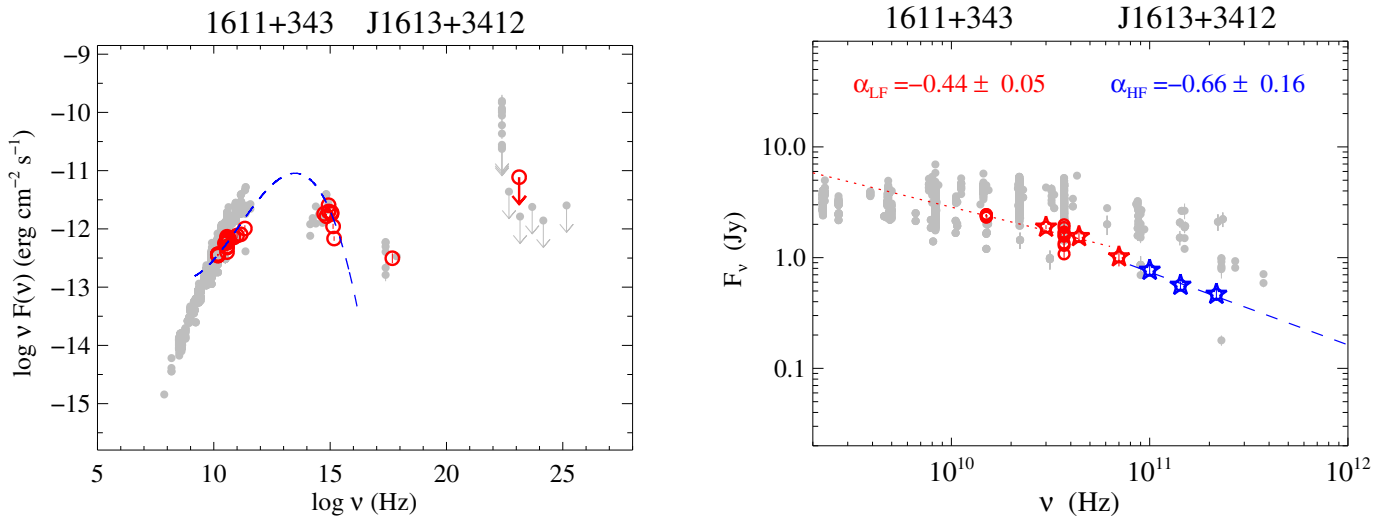
Fig. 86. 1611+343.
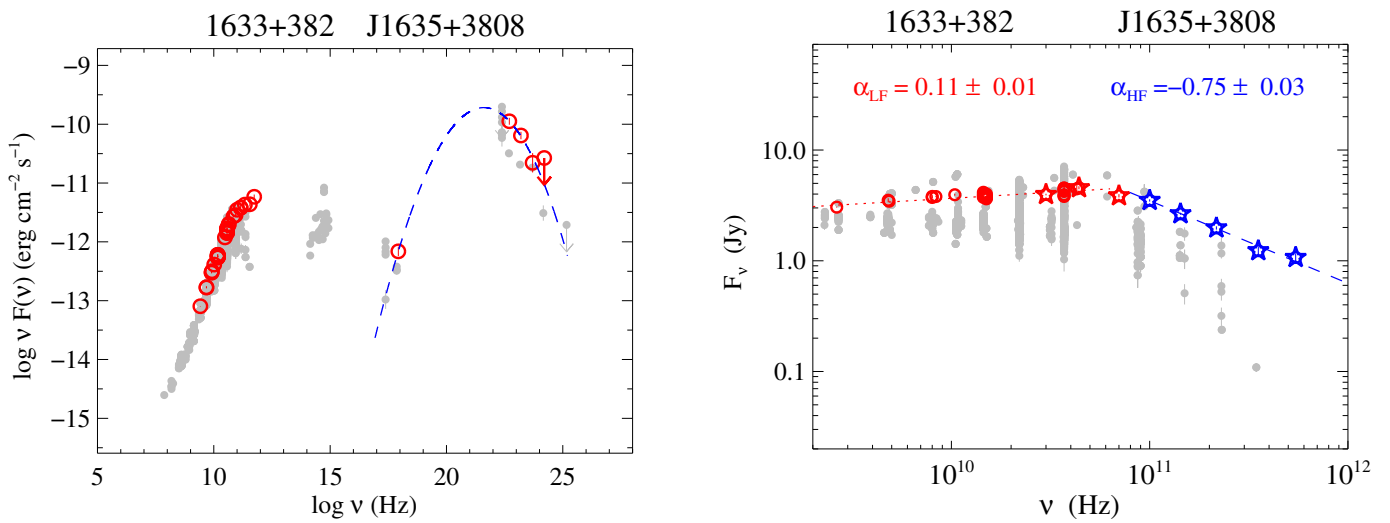
Fig. 87. 1633+382.
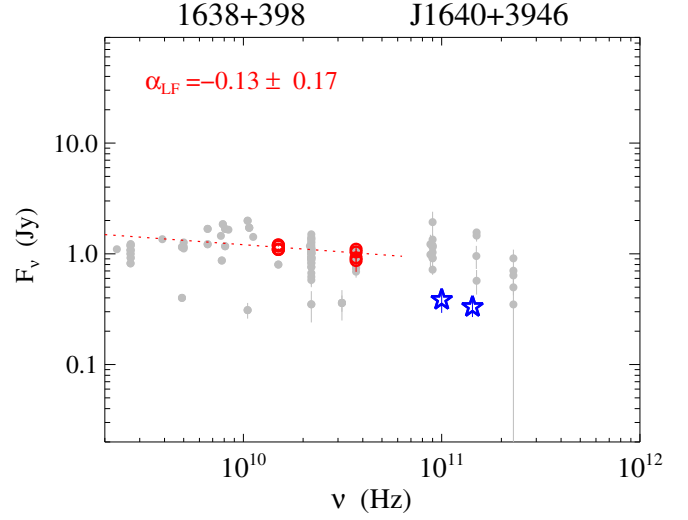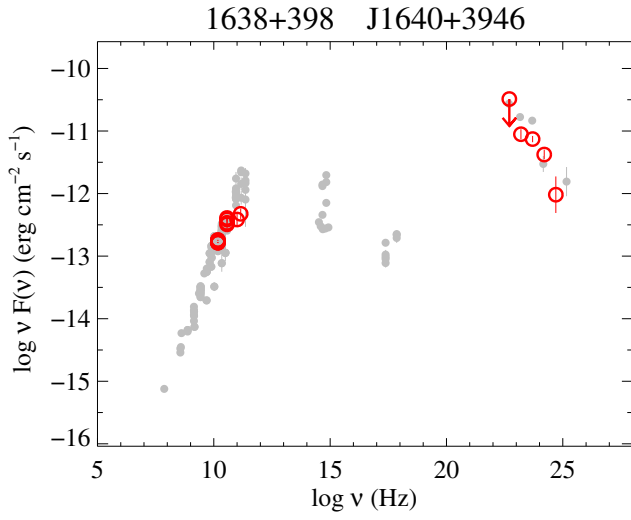
Fig. 88. 1638+398.
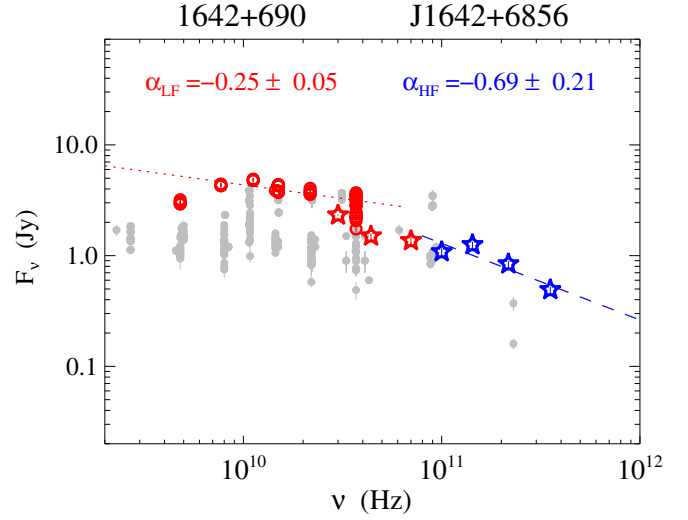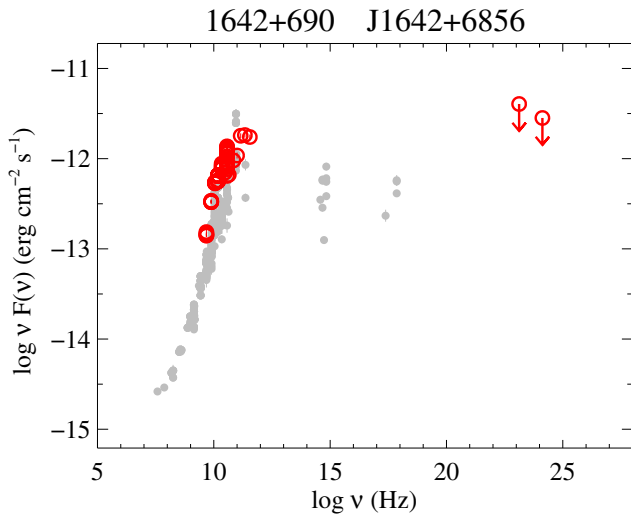
Fig. 89. 1642+690.

Fig. 90. 1641+399.

1652+398   J1653+3945

1652+398   J1653+3945

Fig. 91. 1652+398.

1739+522   J1740+5211

1739+522   J1740+5211

Fig. 92. 1739+522.

1741−038   J1743−0350

1741−038   J1743−0350
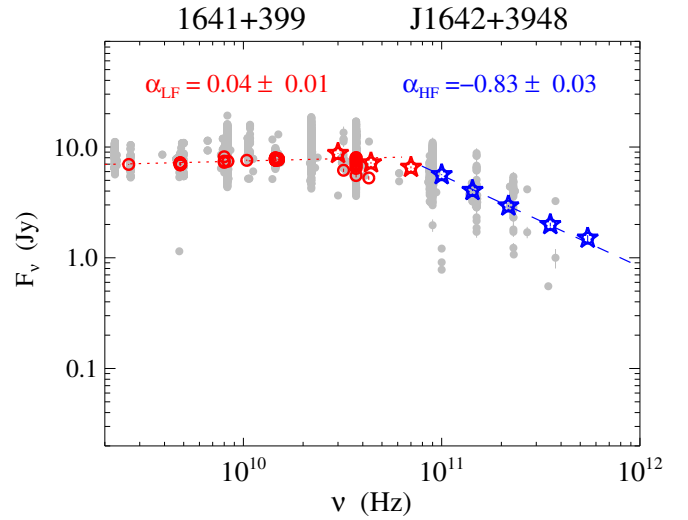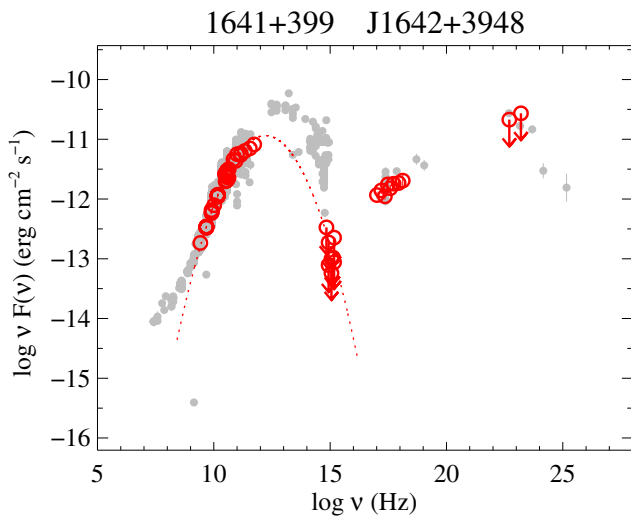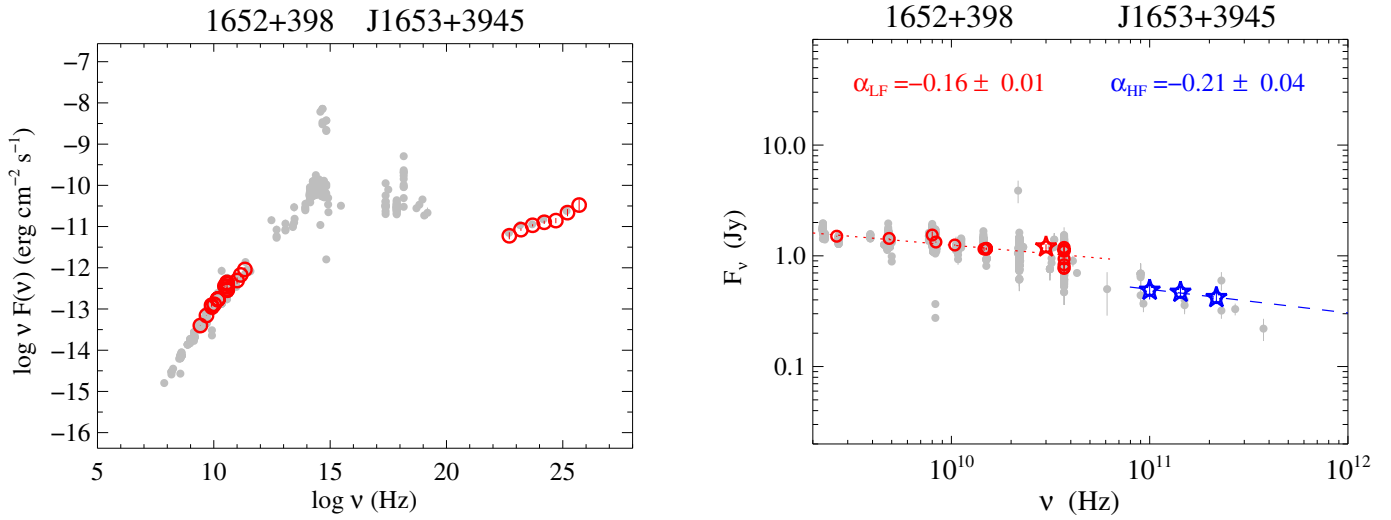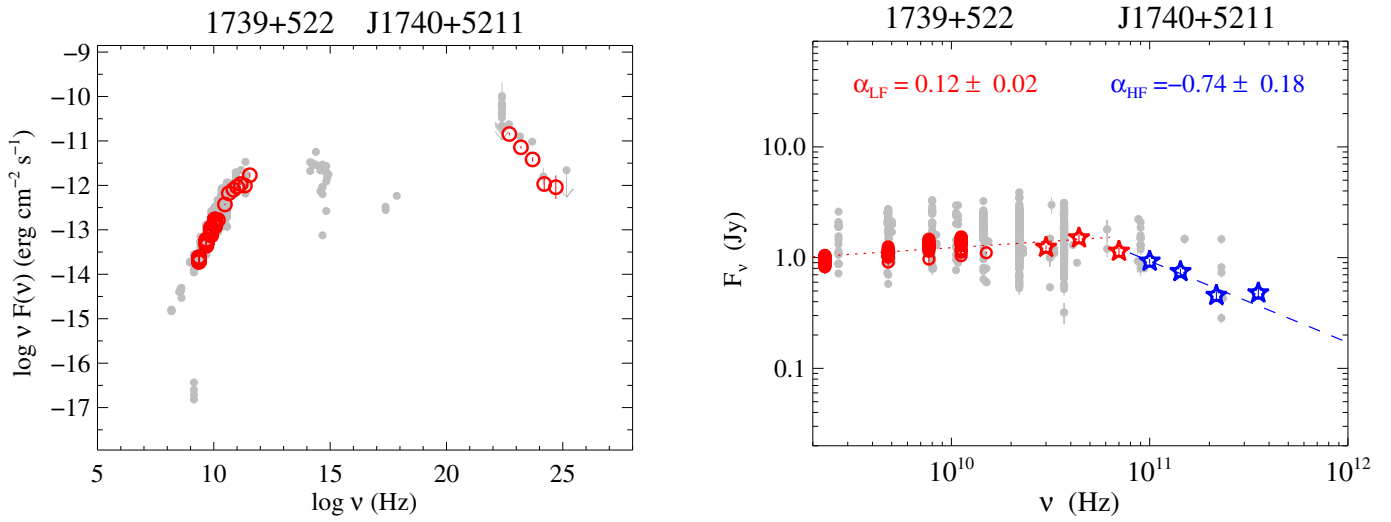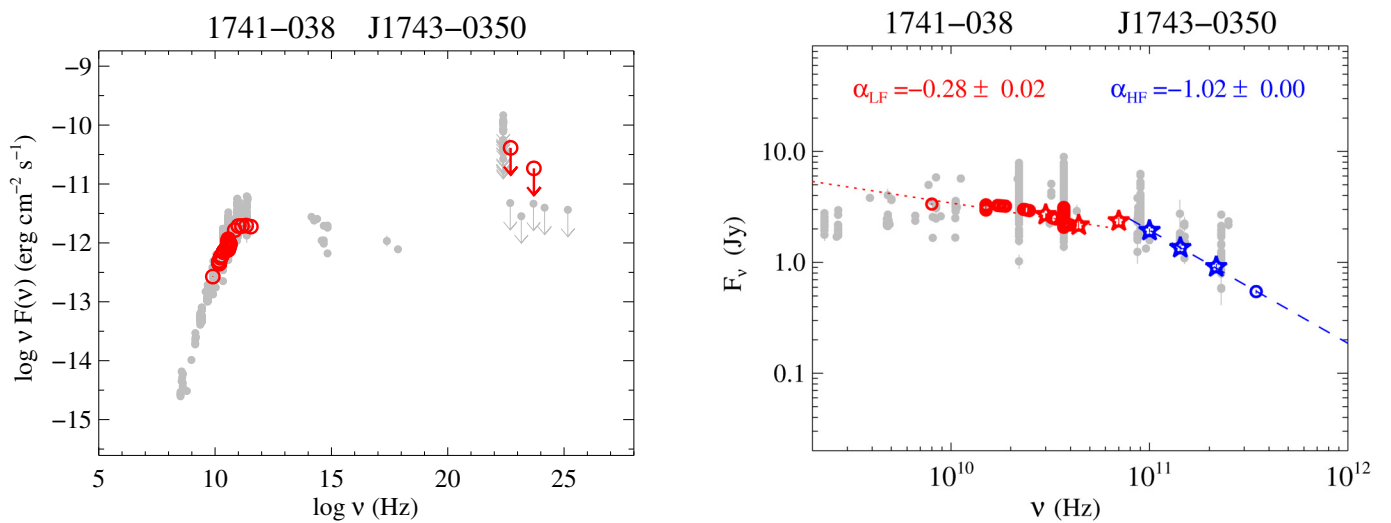
Fig. 93. 1741−038.
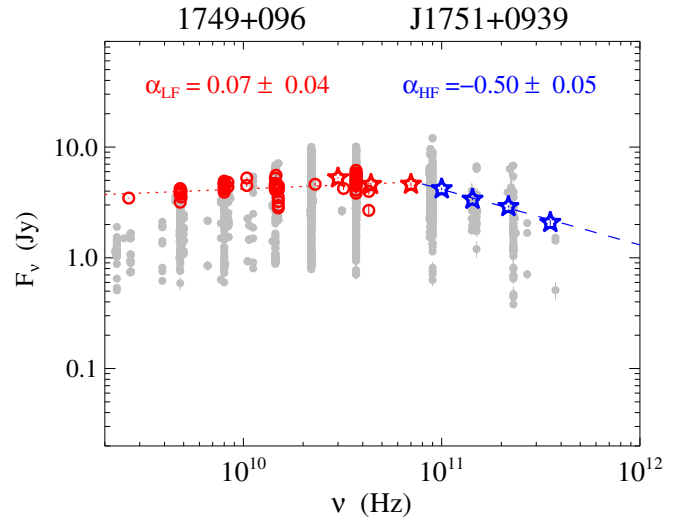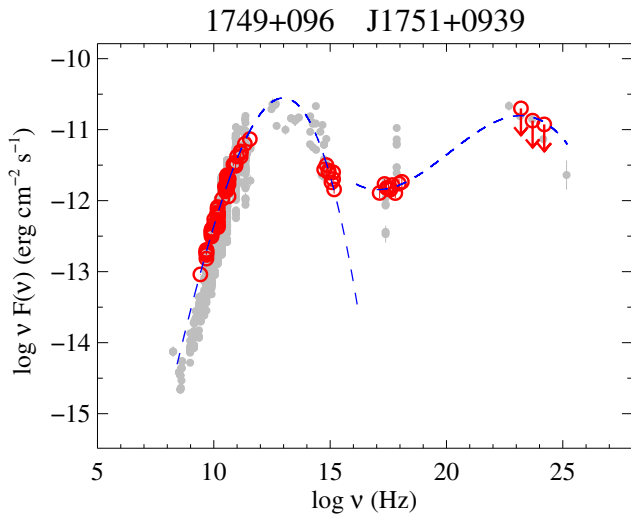
Fig. 94. 1749+096.
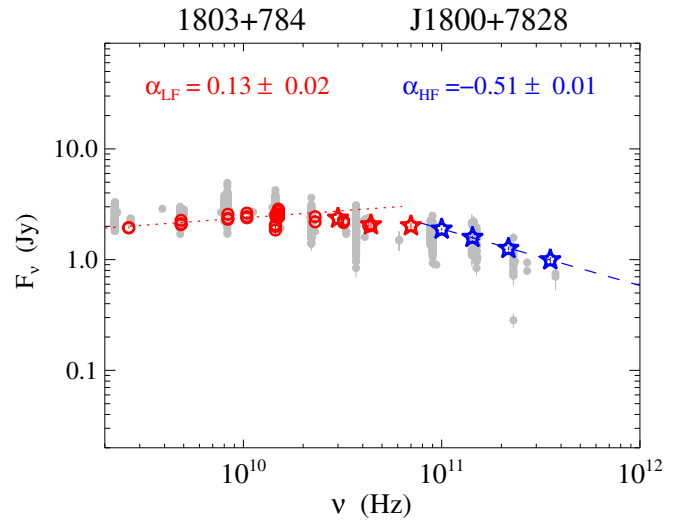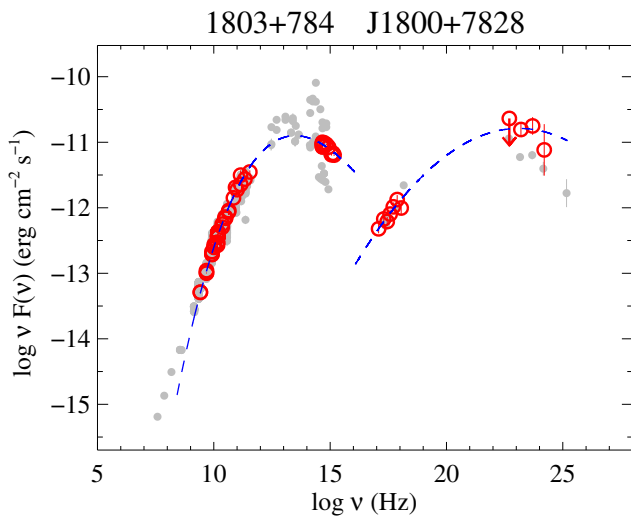
Fig. 95. 1803+784.
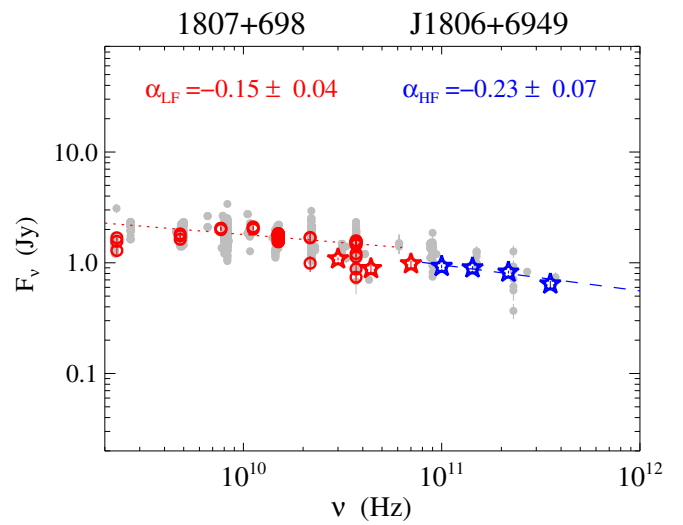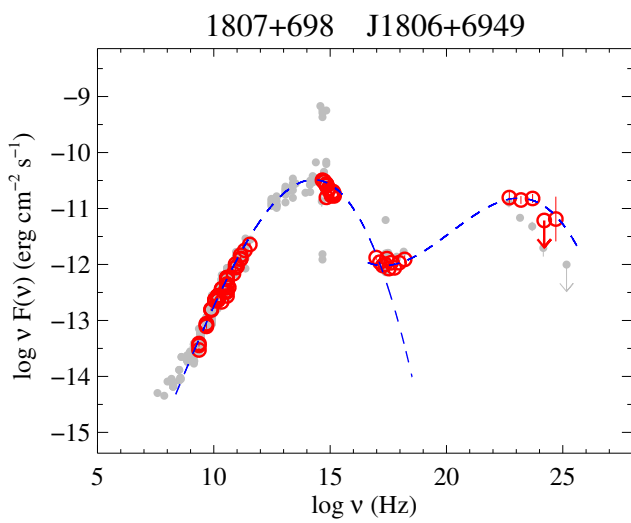
Fig. 96. 1807+698.
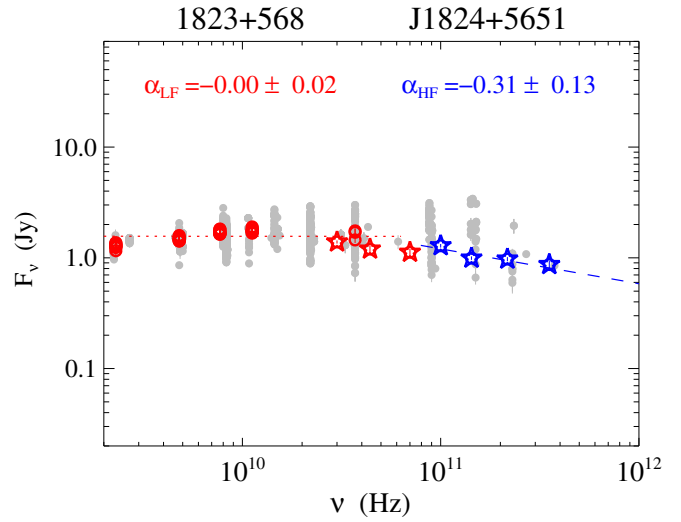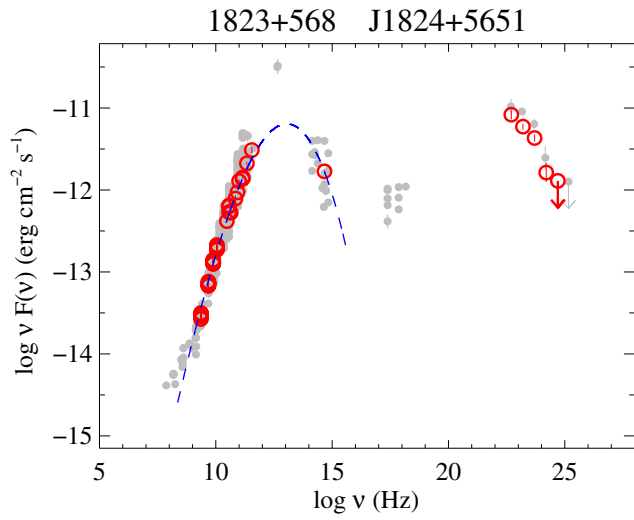
Fig. 97. 1823+568.
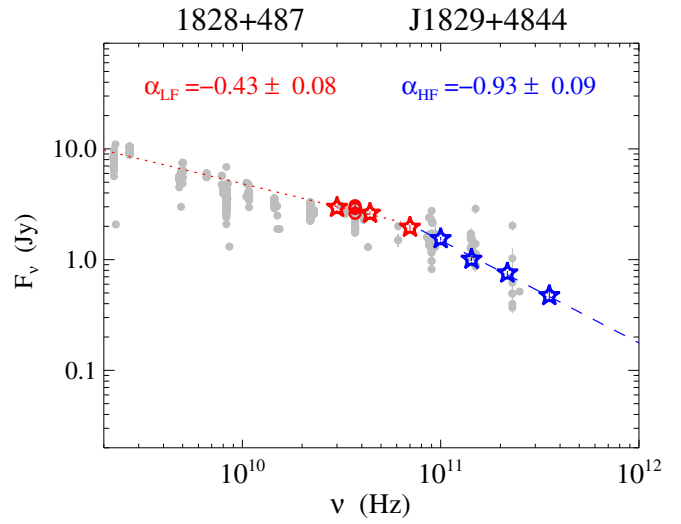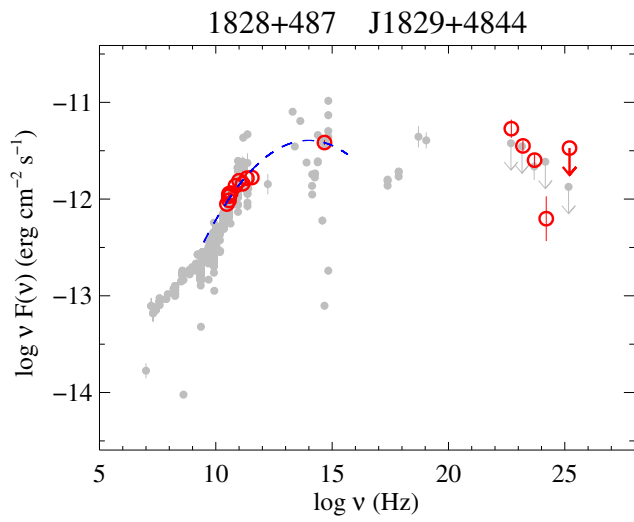
Fig. 98. 1828+487.
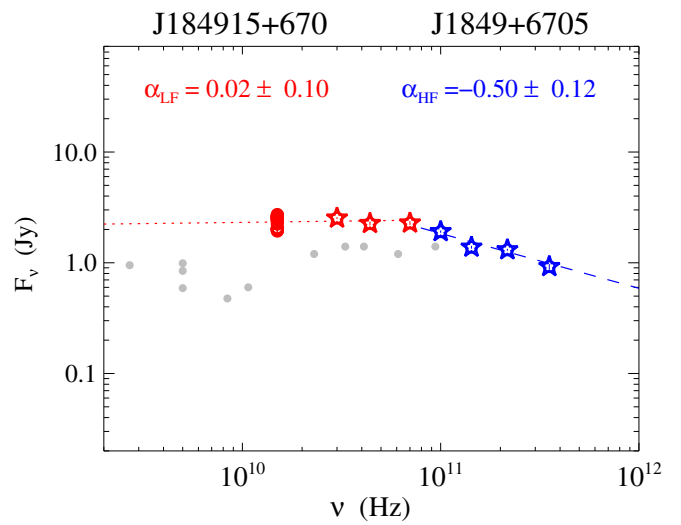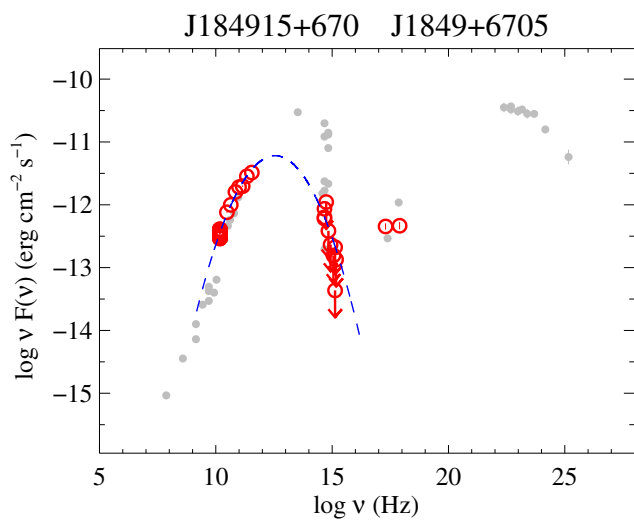
Fig. 99. J184915+670.
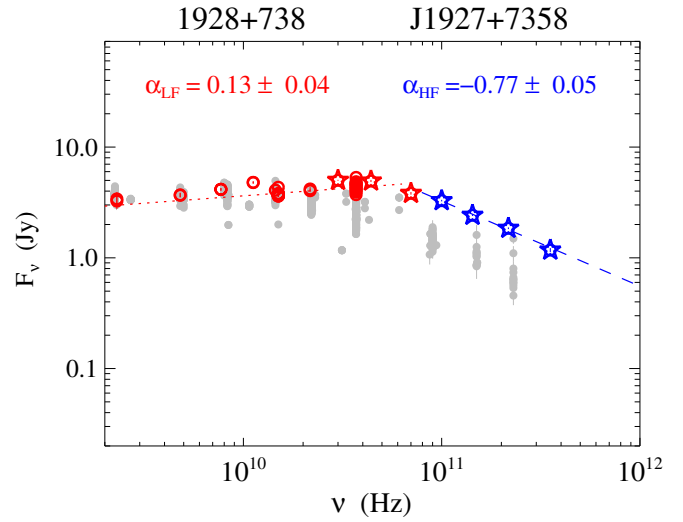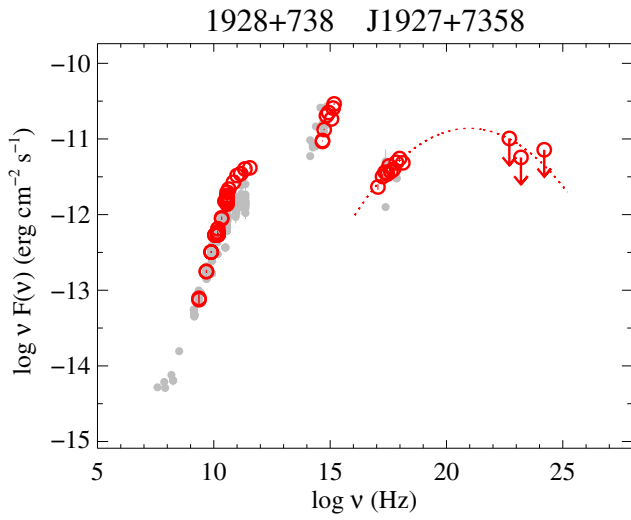
Fig. 100. 1928+738.
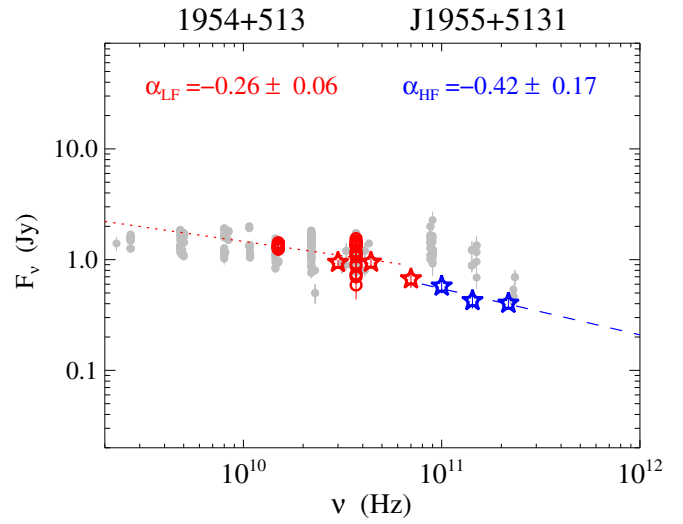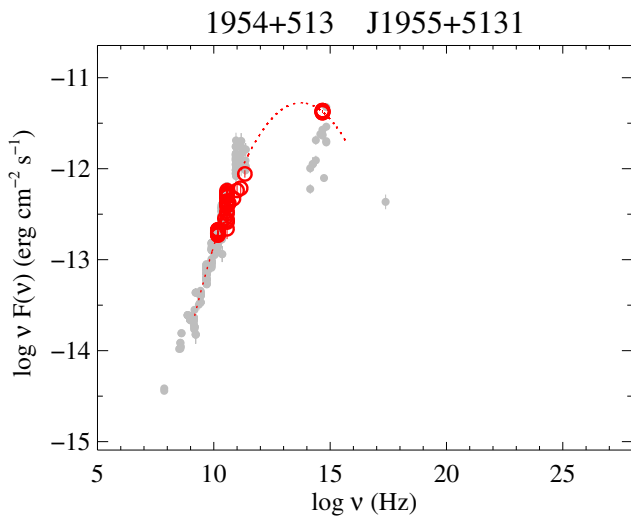
Fig. 101. 1954+513.

Fig. 102. 2007+776.

2005+403   J2007+4029

Fig. 103. 2005+403.

2021+614   J2022+6136

Fig. 104. 2021+614.

2037+511   J2038+5119
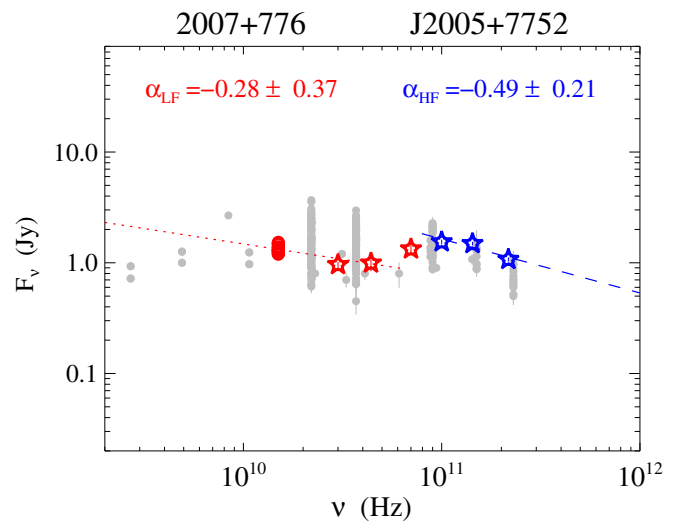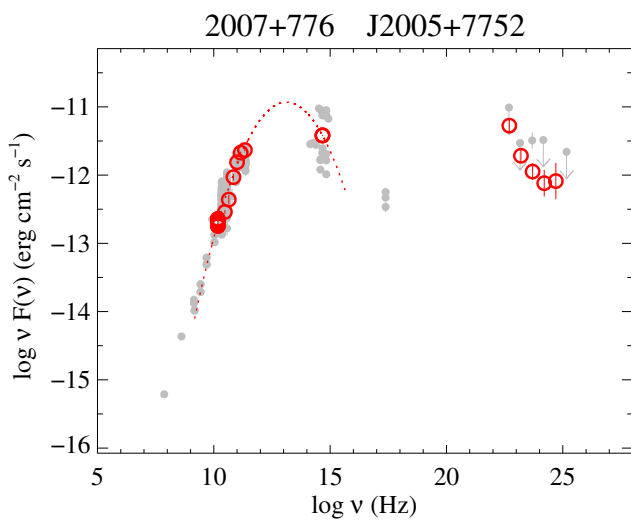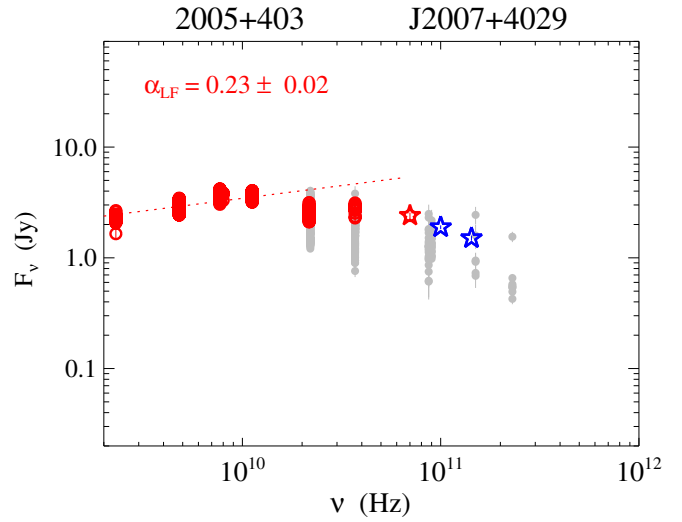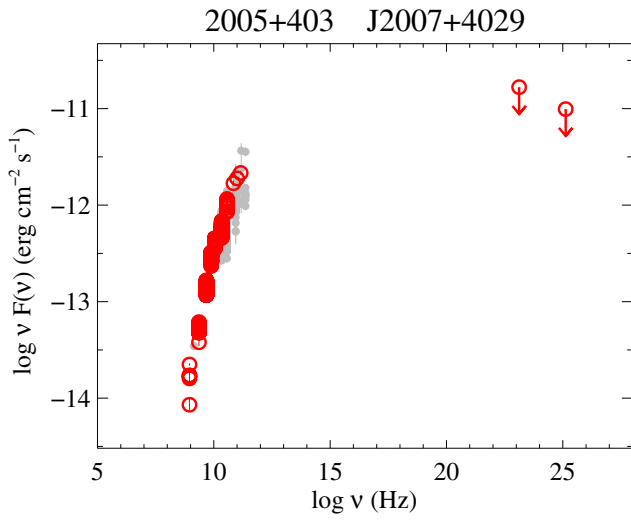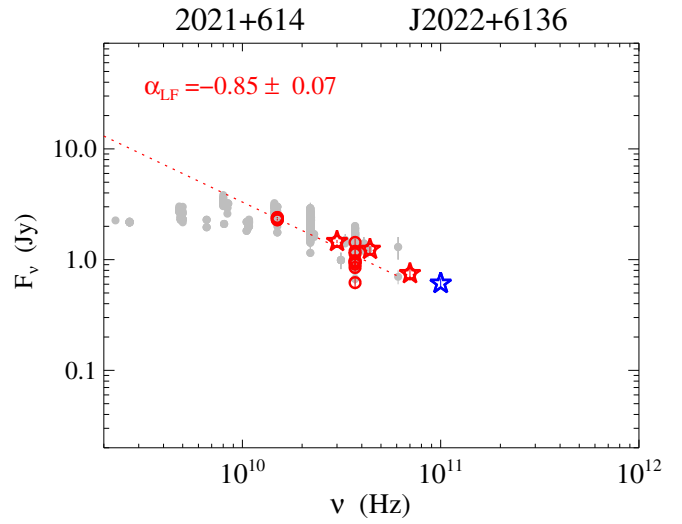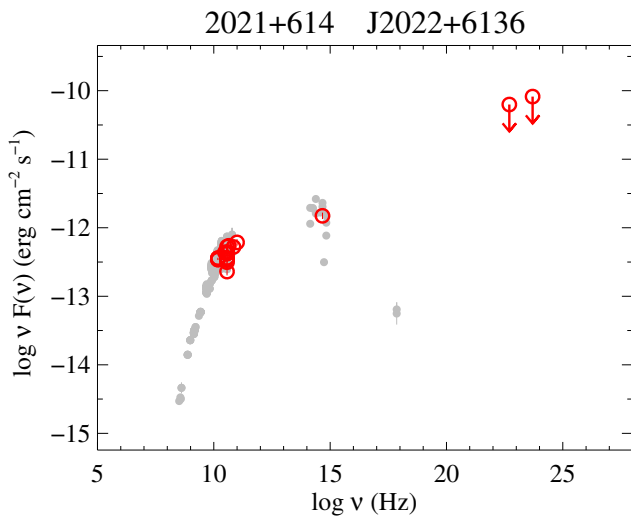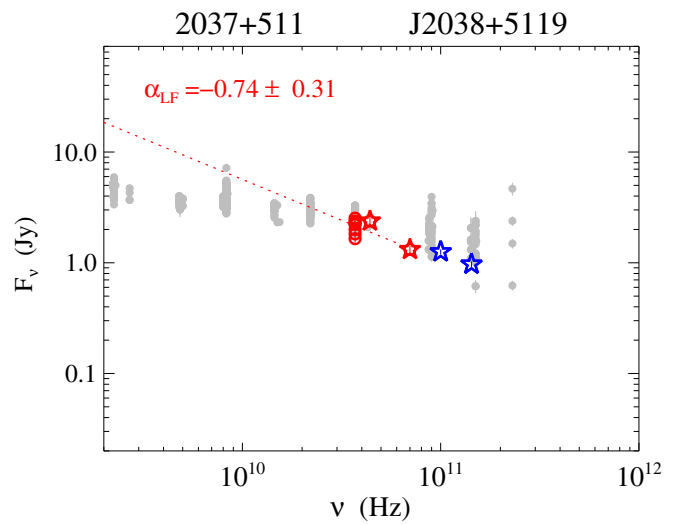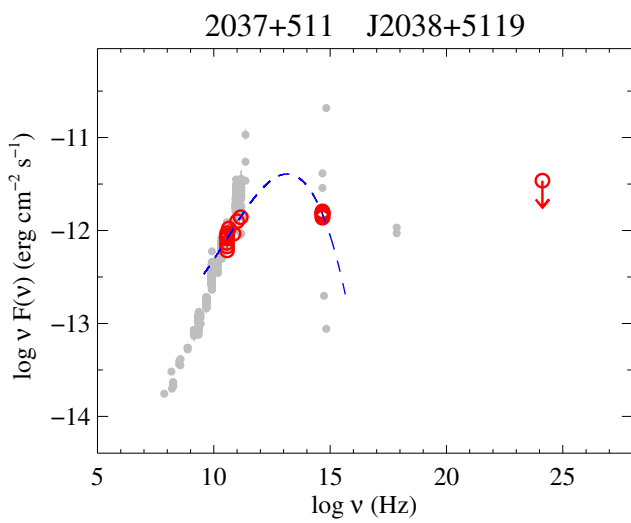
Fig. 105. 2037+511.
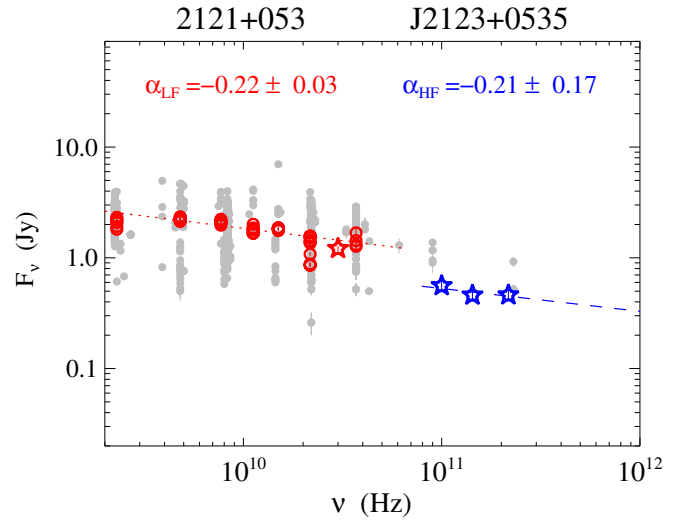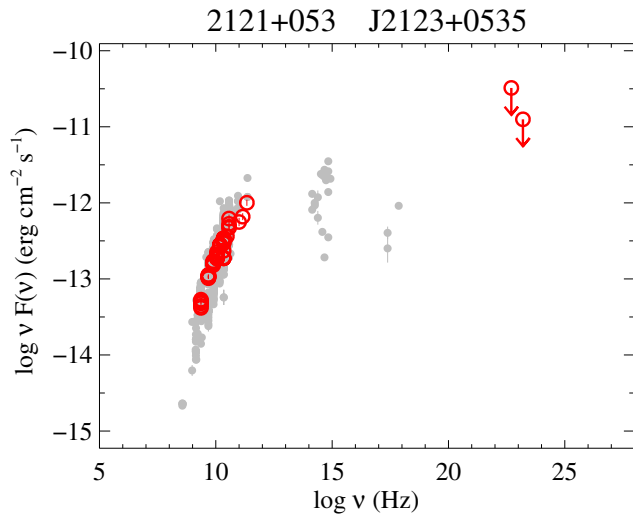
Fig. 106. 2121+053.
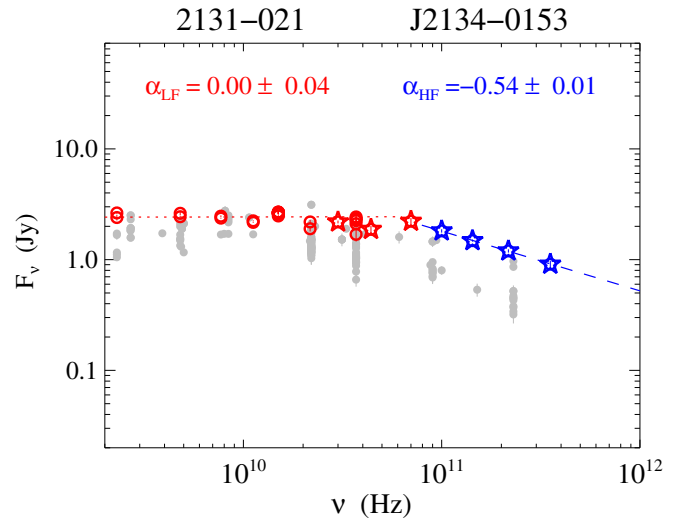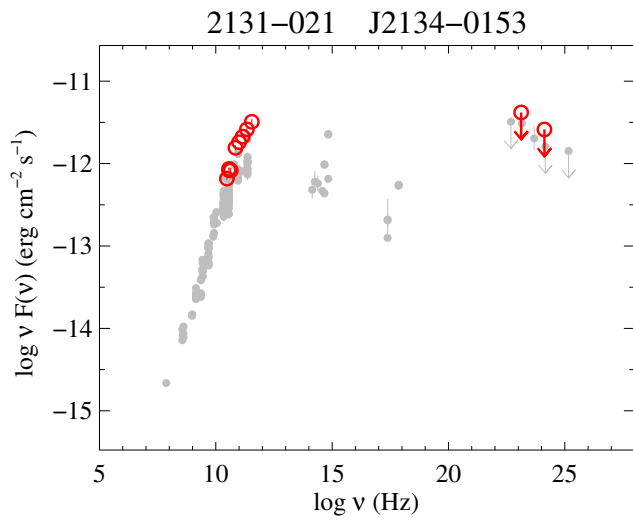
Fig. 107. 2131−021.
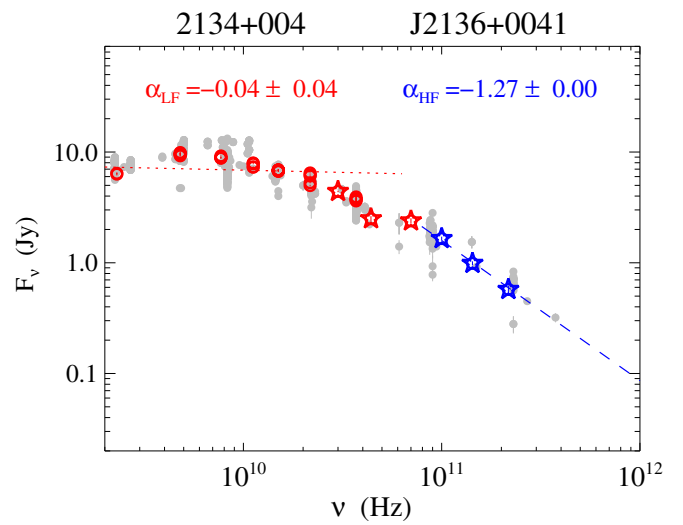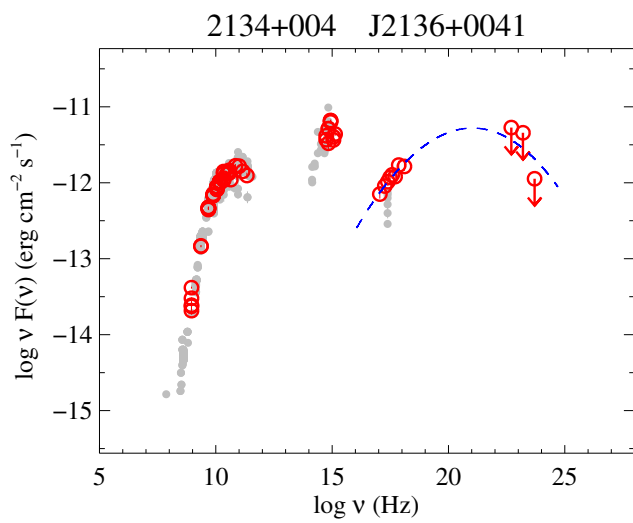
Fig. 108. 2134+004.
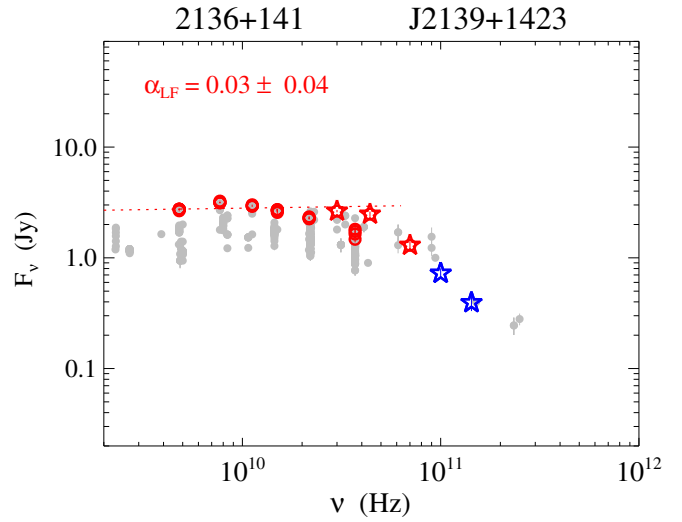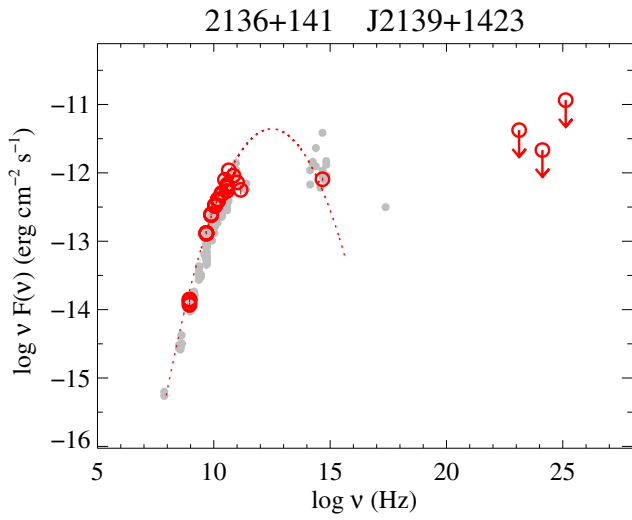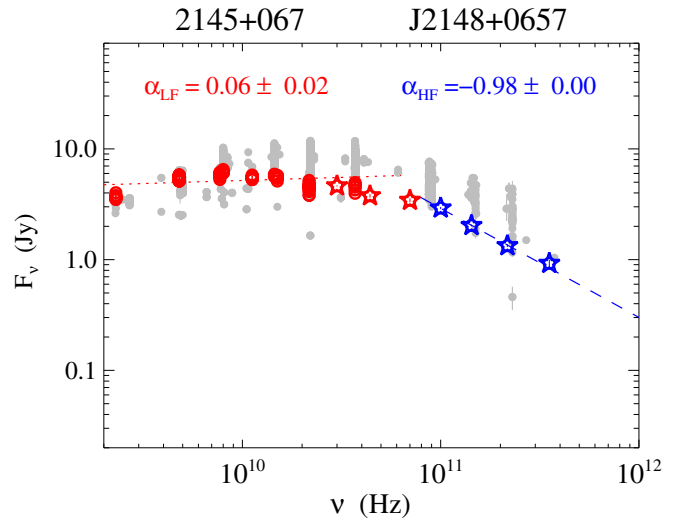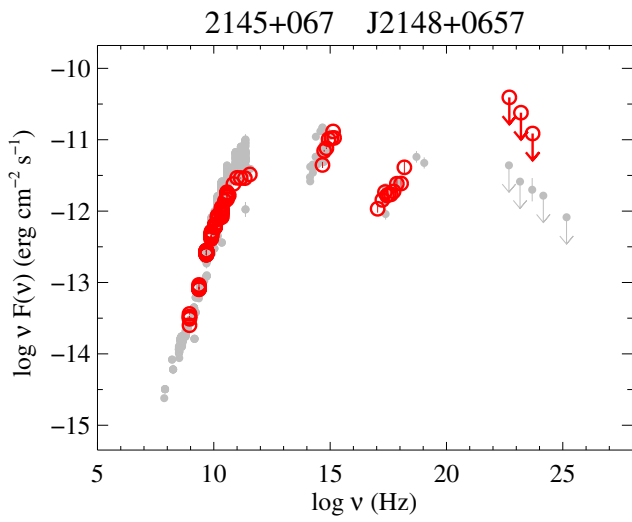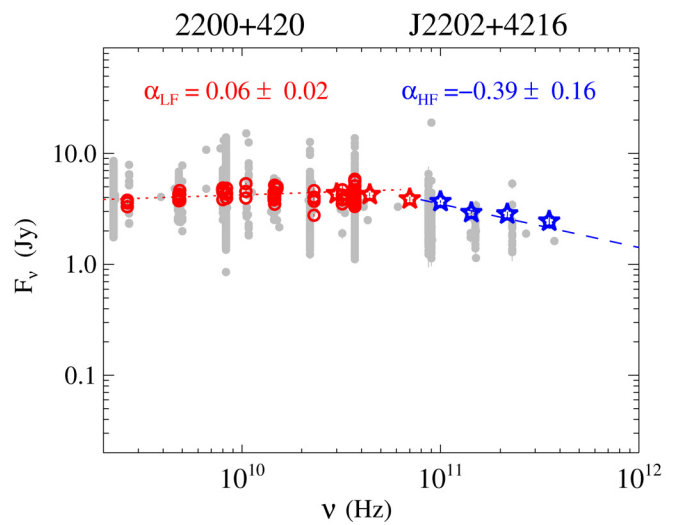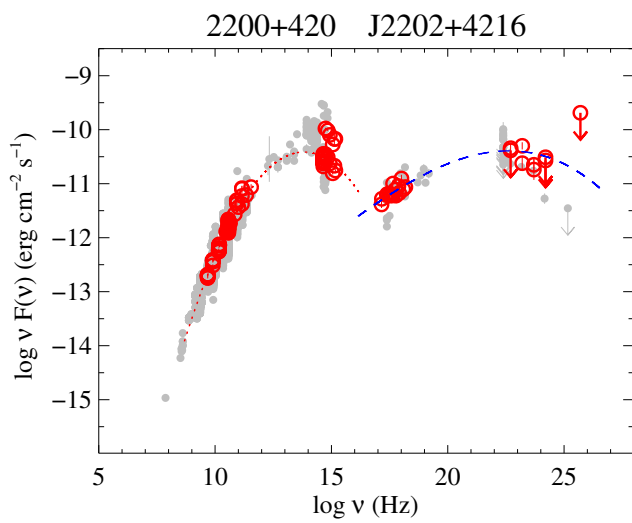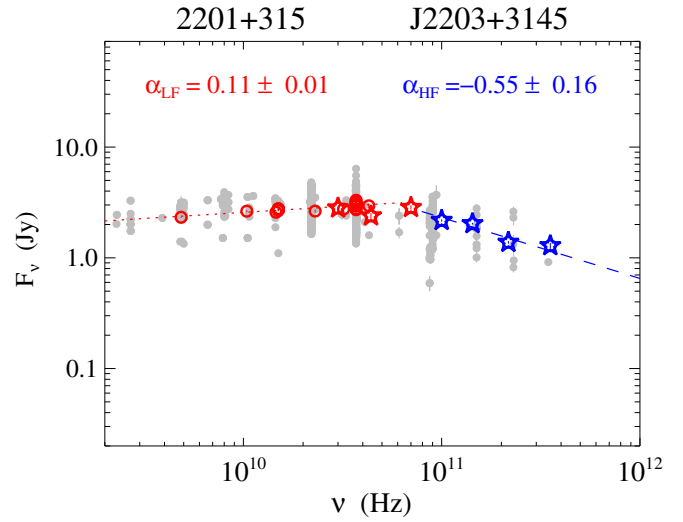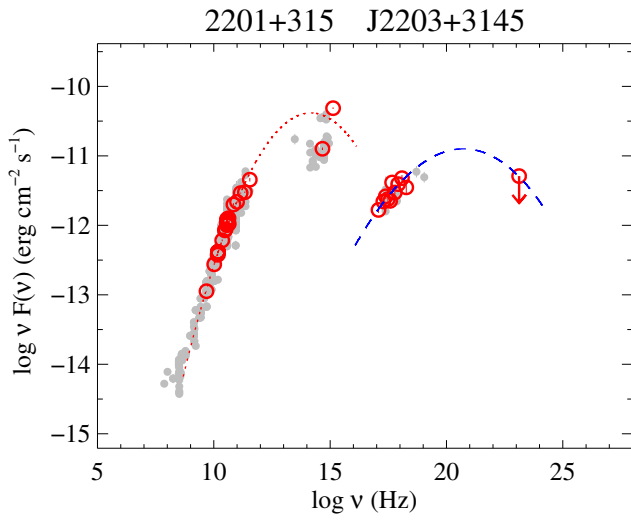
2136+141   J2139+1423

2136+141   J2139+1423

$\alpha_{LF} = 0.03 \pm 0.04$

Fig. 109. 2136+141.

2145+067   J2148+0657

2145+067   J2148+0657

$\alpha_{LF} = 0.06 \pm 0.02$ $\alpha_{HF} = -0.98 \pm 0.00$

Fig. 110. 2145+067.

2200+420   J2202+4216

2200+420   J2202+4216

$\alpha_{LF} = 0.06 \pm 0.02$ $\alpha_{HF} = -0.39 \pm 0.16$

Fig. 111. 2200+420.

2201+315   J2203+3145

2201+315   J2203+3145

$\alpha_{LF} = 0.11 \pm 0.01$ $\alpha_{HF} = -0.55 \pm 0.16$

Fig. 112. 2201+315.

2201+171   J2203+1725

2201+171   J2203+1725

$\alpha_{LF} = 0.10 \pm 0.02$ $\alpha_{HF} = -0.52 \pm 0.03$

Fig. 113. 2201+171.

2216−038   J2218−0335

2216−038   J2218−0335

$\alpha_{LF} = -0.19 \pm 0.02$ $\alpha_{HF} = -0.78 \pm 0.06$

Fig. 114. 2216−038.

2223−052   J2225−0457

Fig. 115. 2223−052.

2227−088   J2229−0832

Fig. 116. 2227−088.

2230+114   J2232+1143
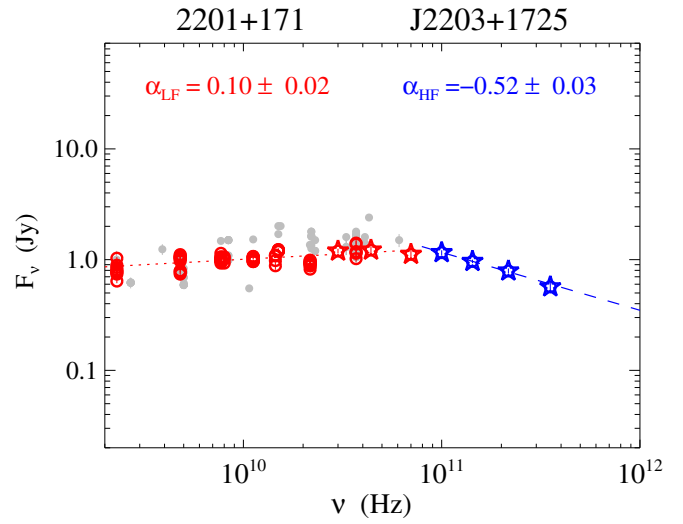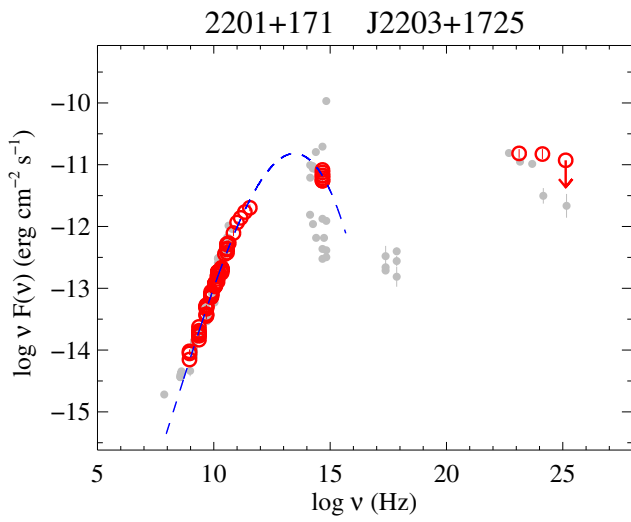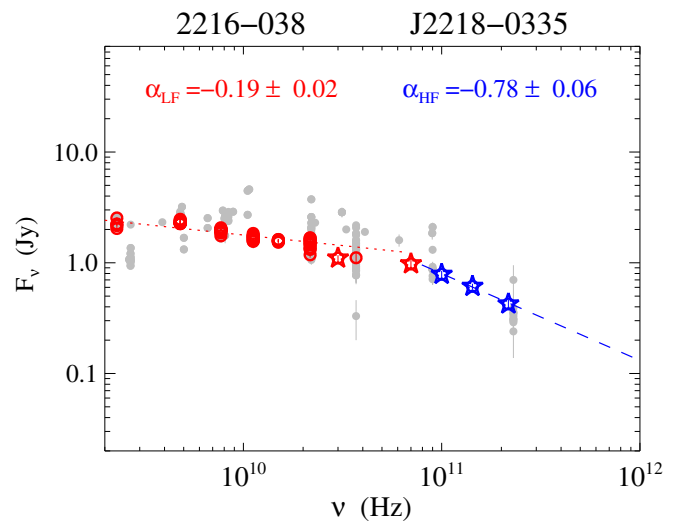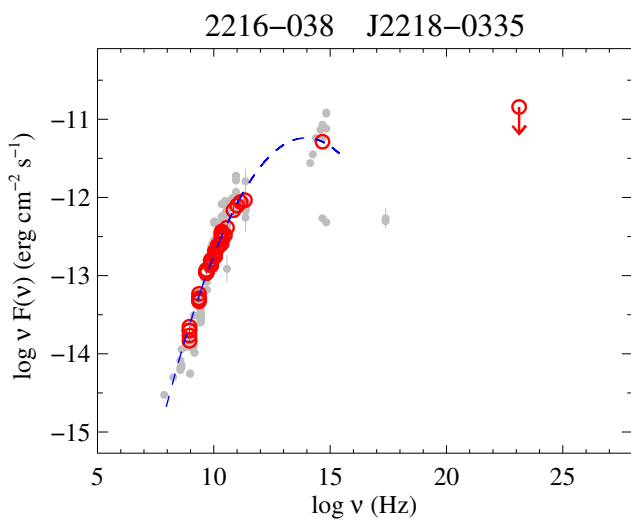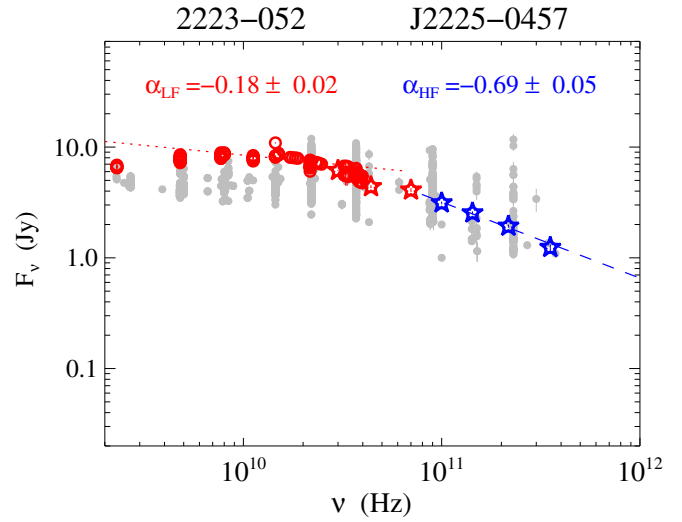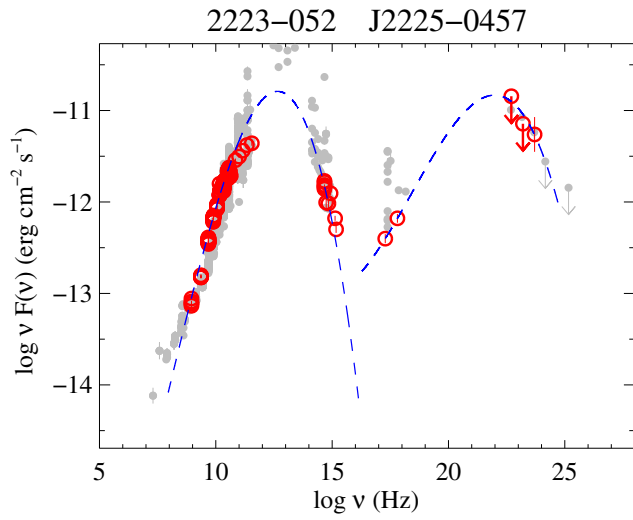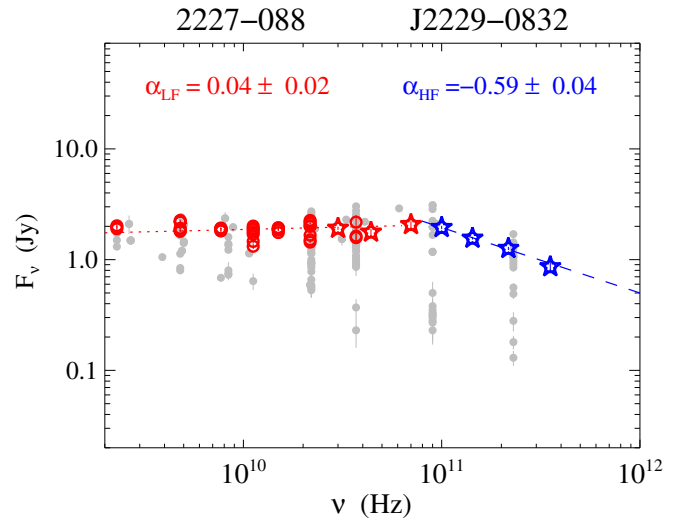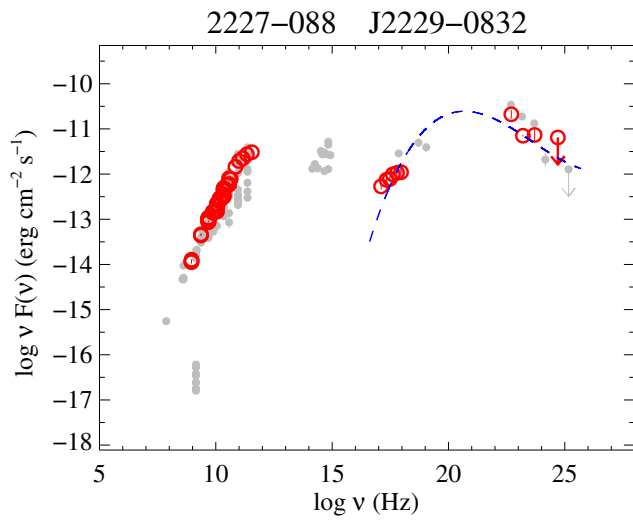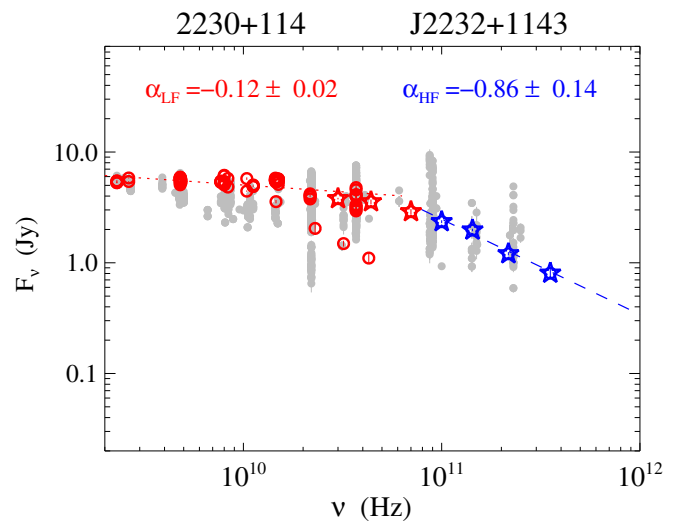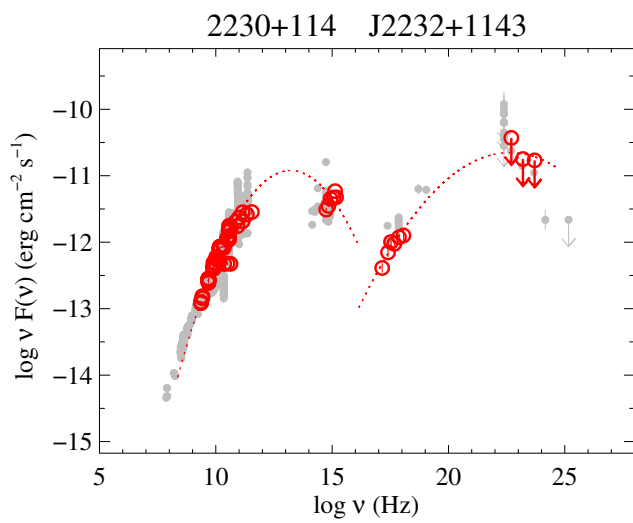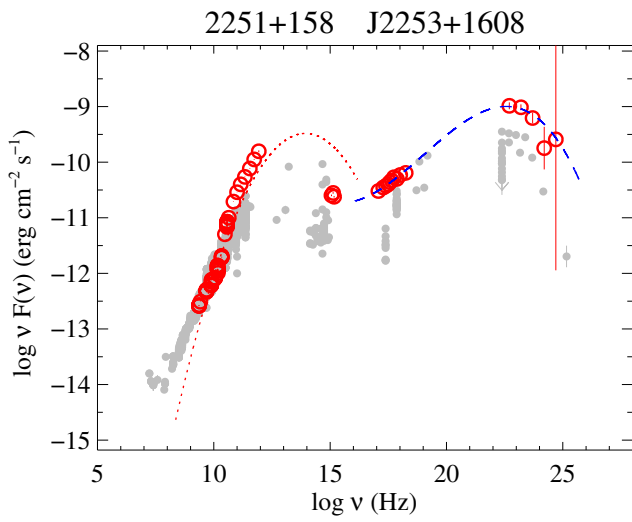

Fig. 117. 2230+114.
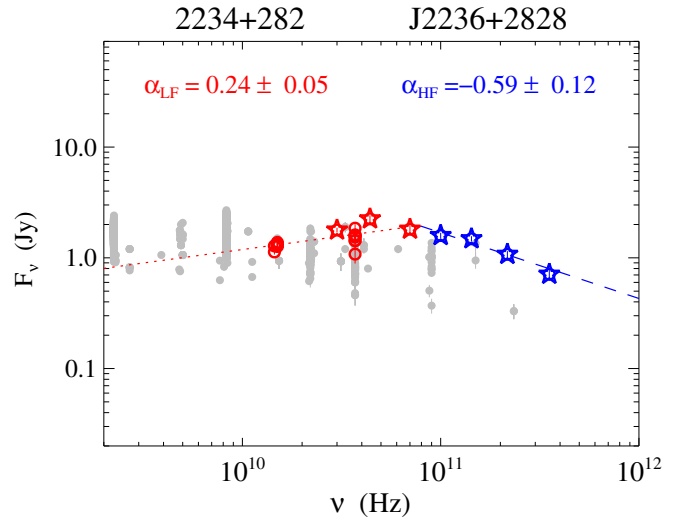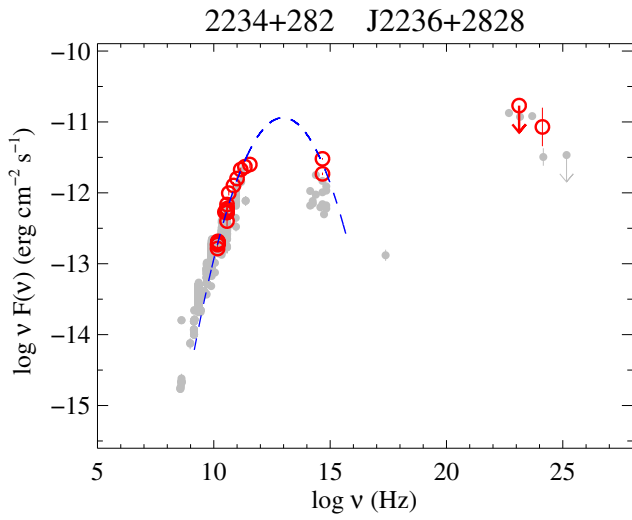
Fig. 118. 2234+282.
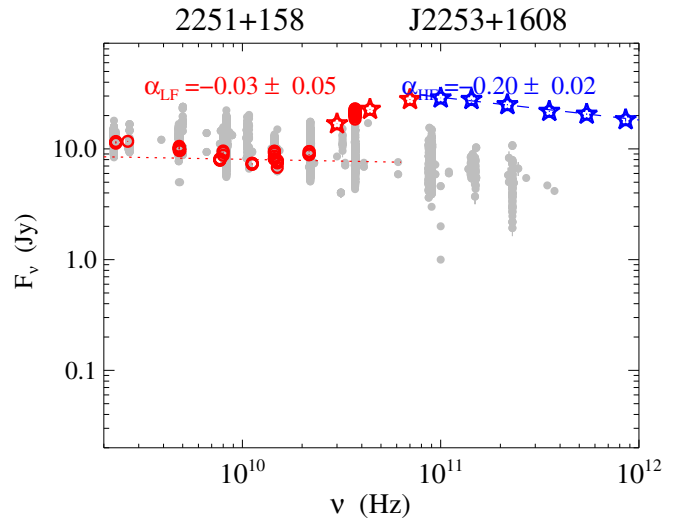
Fig. 119. 2251+158.
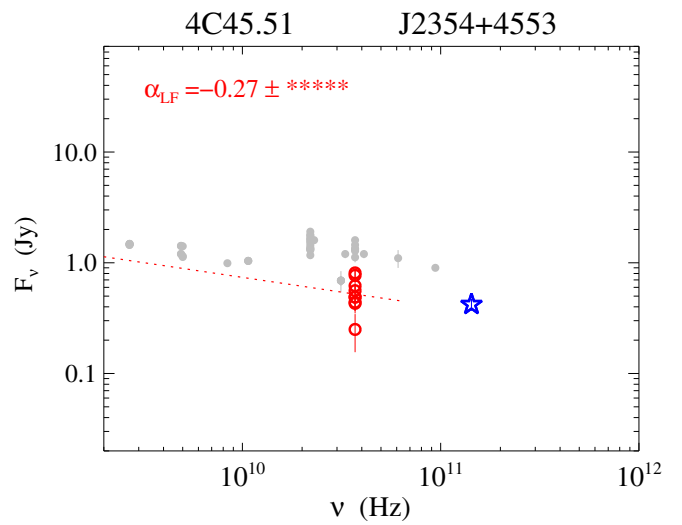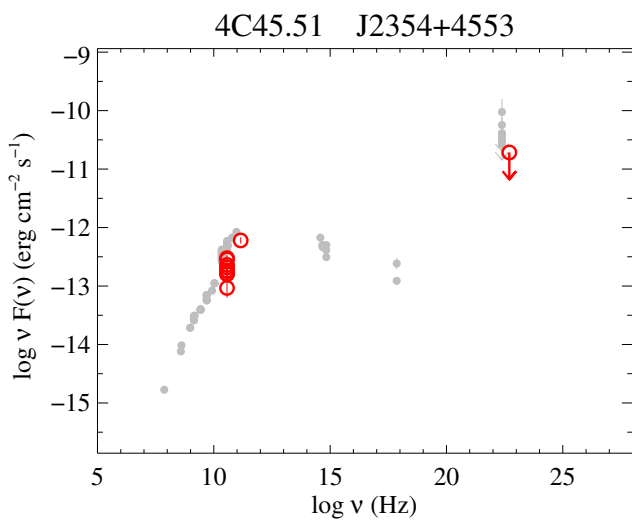
Fig. 120. 4C 45.51.

Fig. 121. 2353+816.